# MATERIALS FOR CARBON DIOXIDE UTILIZATION

Doctor of Philosophy


Fabrizio Silveri

December 2019

# Abstract

In recent years, the rise in popular awareness over climate change and the consequent attention governments have had over the matter has brought to ever-harder goals of environmental sustainability in all sectors of industry. Carbon capture and utilization schemes are one of the many routes that have been proposed to increase the environmental sustainability of the transport and chemical industries, which are two of the biggest carbon emitters on the planet. This strategy aims at closing the cycle of fossil fuel burning by using renewable energy to transform water and carbon dioxide back into fuels and chemicals. In this work, we present a computational study of the electronic structure and catalytic performances of two classes of materials, carbon nitrides and transition metal carbides. Carbon nitrides are semiconductors used for photocatalytic water splitting, a nature-mimicking process which aims at the direct conversion of $H_2O$ into $H_2$ and $O_2$ using solar irradiation and band gap tuned catalysts; in Chapter 3 we will explore their structural and electronic properties, providing a rationale for their experimental catalytic activity. Transition metal carbides are metallic materials which have been shown to catalyse, among other reactions, the electrochemical hydrogen evolution from water and the catalytic reduction of $CO_2$; in Chapter 4 and 5 we will explore the catalytic activity of the low-index surfaces of these materials, identifying descriptors and proposing routes to achieve the best rates and selectivity. The present work aims at improving our understanding of the fundamental behaviour of these materials, as part of the global effort in creating a more sustainable world.

# Table of contents

Abstract ..... I

Table of contents ..... II

Acknowledgments ..... III

Preface ..... V

Chapter 1: Introduction ..... 1

1.1 Global challenges ..... 1

1.2 Photocatalytic water splitting ..... 3

1.3 Electrochemical hydrogen evolution ..... 12

1.4 Carbon dioxide recycling ..... 17

Chapter 2: Computational Methodology ..... 23

2.1 Density functional Theory ..... 23

2.2 Plane wave basis sets ..... 25

2.3 Exploring the potential energy surface ..... 27

2.4 Computational details ..... 32

2.5 Data analysis ..... 35

2.6 Computational Resources ..... 37

Chapter 3: Photocatalysis on oxygen-doped carbon nitride ..... 38

3.1 Experimental evidence ..... 38

3.2 Modelling oxygen-doped graphitic carbon nitride ..... 41

3.3 Electronic properties of FAT models ..... 51

Chapter 4: Hydrogen adsorption on transition metal carbides ..... 57

4.1 Hydrogen Adsorption ..... 58

4.2 High hydrogen coverage ..... 66

Chapter 5: $CO_2$ reduction on transition metal carbides ..... 76

5.1 Adsorption of $CO_2$ on TiC and ZrC surfaces ..... 77

5.2 $CO_2$ reduction on TiC and ZrC ..... 81

5.3 Exploring the potential energy surface ..... 87

Chapter 6: Summary and conclusions ..... 93

Bibliography ..... 95

# Acknowledgments

This thesis is the result of three years of work and the conclusion of academic studies that started as far back as 2010. None of this would have happened without the support of several institutions and countless people along the way, both inside and outside the research environment. What follows is a short and slightly boring list of those institution, and a long but still far from complete list of those people. Both are absolutely necessary, so brace yourselves if you wish to continue reading.

Cardiff University has provided academic support and a fully funded PhD scholarship, allowing me to pursue this research. All the research presented here was funded through an EPSRC low carbon fuels grant (EP/N009533/1). Computing facilities for this work were provided by ARCCA at Cardiff University, Supercomputing Wales, Barcelona Supercomputing Centre through funding of HPC Europa-3, and finally through the UK's Materials Chemistry Consortium (EP/F067496).

My supervisor, Professor Richard Catlow, has been guiding me through my research since September 2016, and his guidance has proved invaluable. He also selected me for this PhD studentship, and I hope I have been a valuable student since then. Dr. Matthew Quesne has followed me almost daily, and I doubt I would have written a dissertation had it not been for his help in finding all the terrible mistakes I made before it was too late. They also helped me balancing workload and mental health when things got rough, and I will never be able to thank them enough for that.

More supervision came from Dr. Alberto Roldán and Professor Nora de Leeuw at Cardiff University, and Dr. Francesc Viñes and Professor Francesc Illas in Universitat de Barcelona. Alberto and Matthew also helped me with specific parts of the research, as well as Yiou Wang from University College London and Dr. Natalia Martsinovic from University of Sheffield, but more on that in the Preface. The help Francesc Viñes and my colleagues here in Cardiff – thank you Julien, Harry, Ali, Samantha, Stefan, Ilaria, Cameron, in rigorously random order – gave me is somehow more subtle, but this thesis might look very different without it. Last but not least, thanks to Silvia, Sofia, Cecilia, Beatrice and Elisa who took some of their precious time to help proofread my thesis, and to Marta, Martina, Cameron and Alessandra, who would have done the same if only I had not forgotten to send the draft.

Finally, there are all those people who might not have helped with the research I am presenting here but most definitely helped me make it this far, without whom I wouldn't be here. First of all, to my family. To my grandad, who didn't live long enough to see this but I hope he would have liked seeing it, and to my grandmas who I have lost too soon. To my mum and my dad, who don't even complain if I disappear for weeks in a row, even if they're worried. To my uncles and aunties, to my cousins and to my siblings, who are always there for a chat and some support, and with whom I might not talk too often when I'm in Cardiff but I know it won't matter once I am back. To Maria Flavia, cousin and friend since before I can remember. And then to my nephew and nieces – to Margherita, Viola, Luca, Bianca and Emma. Non so neanche spiegarvi quanto contiate per me, ma forse non importa perché lo sapete già.

Then there are all those amazing people who I have met throughout my life and who, for reasons I never fully understand, decided I was a keeper. To Stefano, Chiara, Nicola, Nicca and the others who stuck with me since we were 5. To Lorenzo, Thomas, Irene, who I met at school and never left since, and to those who joined us later but care for us all the same. To Silvia, Sara, Marta, Laura and the others who have accompanied me through university and are still with me. To Astrid, who decided to take a different path but will always matter in my life. To Nivi, Hannah and Elysia, whose terrible luck chose to be my housemates, but who chose to be my friends anyway. To Nikki and the crew of Cardiff University Hiking Club, so many of you have become my friends for a while, so many of you I will keep as friends for much longer. To Hannah and the People and Planet lot, with whom becoming friends was just as natural as breathing. To Ivett, Askandar and the STAR refugees, who've taught me more than I could ever teach them. To Winston, who is the most amazing person I have met in this city, and whose friendship helped me live to see this moment. To Chiara, Serena, Marta, Leah, Elena, Bea, Elisa, Ari, Gintare, Ilaria and to those I forgot – please forgive me, and rest assured you're not forgotten – who might not fit in any of those categories but care for me, and that's enough to be part of the reason why I can be here to write this words. To all those people in Roma, in Cardiff, and around the world who helped me get here.

Thank you.

# Preface

Part of the research presented here has previously been published in peer-reviewed academic journals. A large portion of the results reported in Chapter 3 were originally submitted as part of the main text and supplementary information of the paper "Bandgap engineering of organic semiconductors for highly efficient photocatalytic water splitting", published in *Advanced Energy Materials*, 8, 24, 1801084 and authored by Yiou Wang, Fabrizio Silveri, Mustafa K. Bayazit, Qiushi Ruan, Yaomin Li, Jijia Xie, C. Richard A. Catlow and Junwang Tang. The research presented here is an expansion of the work reported in the computational section of that paper, and was carried out with the aid of Yiou Wang from University College London, who provided the experimental data reported in section 3.1, and of Dr. Natalia Martsinovic from University of Sheffield, who provided the computational models used in a previous work, co-authored by herself, on a similar material. Their contribution is reported and cited in the main text of Chapter 3.

The research described in Chapter 4 was initially published in an entirely computational paper, "Hydrogen adsorption on transition metal carbides: a DFT study", published in *Physical Chemistry Chemical Physics* 19, 21, 5335-5343, and authored by Fabrizio Silveri, Matthew G. Quesne, Alberto Roldan, Nora H. de Leeuw, and C. Richard A. Catlow. The slab models of transition metal carbide surfaces used for such research and in Chapter 5 were originally prepared by Dr. Matthew Quesne for his work published in *Phys. Chem. Chem. Phys.*, 2018, 20, 6905-6916, as cited in section 2.4. Finally, the calculation of the temperature dependence of the chemical potential of hydrogen presented in Chapter 4 was performed by Dr. Alberto Roldan, who also wrote some of the code necessary for the Bader charge, DOS and work function analyses reported in Chapter 3 to 5.

# Chapter 1:
# Introduction

## 1.1 Global challenges

Recent years have seen a sharp increase in popular awareness on the topic of climate change, partly due to the increasingly tangible effects of global warming[1–3] and the efforts of public figures supporting radical policies to reduce greenhouse gas (GHG) emissions, such as U.S. Congresswoman Alexandria Ocasio-Cortez[4] and Swedish student Greta Thunberg.[5] The global student movement led by Thunberg, which has pushed millions of people to rally the past September,[6] and the historic result of the European Green Party in the 2019 European Parliament Elections,[7] which obtained a record number of seats, are just some of the many recent examples of popular initiative aimed at influencing the decisions of governmental and intergovernmental bodies towards a sharp decrease in GHG emissions within a few years. Past decisions such as the Paris Agreement,[8] through which 195 UN-registered nation agreed to reduce their carbon emissions within a short time span and implement a strategy of energetic sustainability in the longer term, have been seen as insufficient by climate activists[6] as well as by the UN-led International Panel on Climate Change (IPCC), which recently concluded that an increase in average global temperature of only +1.5° C with respect to the pre-industrial era could lead to catastrophic consequences for several life forms on Earth and have a deep impact on the economy and wellbeing of several countries.[9]

### *The role of chemistry*

The existence of such severe threats and ambitious political goals has sustained research aimed at reducing and possibly halting the use of fossil carbon. While many ambitious targets can be reached using the current technology for renewable energies, certain uses for fossil fuels will require the discovery and application of novel solutions to allow for entirely renewable supply chains.[10,11] An example of that is the synthesis of fuels and chemicals, which cannot yet be fully replaced by energy generation and storage technologies, especially in avenues such as the synthesis of jet

fuels, in which the weight to energy ratio is of paramount importance, and of base chemicals, which are produced in such a scale that the current technologies for chemical recycling cannot compete with the use of fossil carbon.[11–13] The combination of hydrogen generation through water splitting and carbon capture and utilization (CCU) schemes is a widely proposed solution[14,15] for some of these problems which uses water-derived molecular hydrogen either as an environmentally sustainable reducing agent for $CO_2$ to chemically recycle it into useful fuels and chemical. Significant research effort is being undertaken throughout the world to overcome the chemical and technological challenges related to these reactions, including the present work: the focus of this thesis is the computational modelling of catalytic materials for molecular hydrogen generation and carbon dioxide recycling.

### *The hydrogen economy*

The transition from an economy based on the use of fossil fuels for energy production to one based on the use of hydrogen as primary energy storing chemical – the so-called hydrogen economy – has been a major drive for scientific and engineering research in the last few decades. As far back as 2003, the topic was considered important enough to be featured in the annual State of the Union address by the U.S. President George W. Bush,[10] and has since been the long-term goal of countless research. As the effects of climate change have become more evident and dramatic over the years, the interest in abandoning the oil economy has further increased, but several challenges have yet to be overcome in order to make this transition possible. One major issue with the transition to a hydrogen-based economy is the energy required to produce the latter fuel;[14,16–18] molecular hydrogen can be produced from a variety of sources, but the technology most often implemented industrially – steam reforming of natural gas – is not in any way more environmentally sustainable than traditional fossil fuel combustion, as it is estimated to release 8.9 Kg of $CO_2$ into the atmosphere per Kg of $H_2$ produced.[19,20]

### *The hydrogen cycle and the carbon cycle*

The only carbon free source of hydrogen is water,[21] which can be split into its gaseous elemental components $H_2$ and $O_2$. This reaction is endothermic, but since the energy required to the break the O-H bond is stored in $H_2$, the latter can be used as a fuel in hydrogen fuel cells to provide energy by combining with atmospheric $O_2$, forming

$H_2O$ again. While this represents a perfect fuel-energy cycle, theoretically waste-free and therefore sustainable, the energetic requirements of $H_2$ production from water pose substantial research challenges.[22,23] The energy required for the $H_2$ evolution to take place can be provided in several ways, such as thermally, biochemically, electrochemically and photochemically.[24–28] In electrochemical and photochemical processes, which are of interest here, the energy required for $H_2$ evolution is provided through direct reduction of water by an electron, which is brought to a suitable energy level either by the potential applied to an electrocatalyst or by absorption of a photon of corresponding energy. The details of photochemical and electrochemical water splitting will be discussed later, as they are the focus of the research discussed in Chapter 3 and Chapter 4 of this work. Once generated, molecular hydrogen can either be used as a fuel in the aforementioned hydrogen fuel cells or as a chemical for its well-known reducing properties. Carbon capture and utilization (CCU) projects use these properties to recycle carbon dioxide.[11,12,29] The objective of such projects is of course the reduction of the overall $CO_2$ emissions of human technology, as recycled $CO_2$, generally in the form of CO or $CH_3OH$, can replace fossil fuels as feedstock for the production of fuels and chemicals. As with the hydrogen cycle, this $CO_2/H_2$ cycle can theoretically be sustainable and waste-free, but the science and technology required for carbon dioxide recycling on a global scale are not fully understood yet, as we will further investigate in Section 1.5.

## 1.2 Photocatalytic water splitting

*Introduction to photocatalysis*

Photocatalysis is the acceleration of the rate of a reaction obtained by shining light on a photosensitive material. This material – the photocatalyst – can absorb a photon as a result of exposure to electromagnetic radiation, resulting in the promotion of an electron into a higher energy state and in the creation of an electron – hole pair. This process can accelerate a redox reaction by enhancing electron transfer to or from the adsorbed species, as electron – hole pairs are only metastable and can lead to very efficient redox activity. [14,21,30] The principles of photocatalysis were first formalised as far back as 1938,[31] but a major scientific breakthrough in its application only came in 1972, when Fujishima and Honda first reported the photocatalytic electrolysis of

water using an electrochemical cell constituted of a $TiO_2$ cathode and a Pt anode, in which the source of potential was the light absorption on the former electrode rather than the presence of a battery or generator as in traditional electrochemical cells.[32] Since then, photocatalysis has been investigated and applied to various systems and practical problems, such as the oxidative degradation of organic compounds, sterilization and sanitation of materials, and synthesis of paint pigments and cosmetics.[33] Beyond $TiO_2$, which has been proved as a suitable photocatalyst for many applications, a wide variety of semiconductive materials has been reported as photocatalytically active in both heterogeneous and homogeneous systems.[21,33,34]

Since photon adsorption is a necessary step of photocatalysis, multiple stable redox states and a suitable band gap are necessary in the photocatalytic material, limiting the choice of potential catalysts for reactions of this kind. Usually the best photocatalytic activity is found for those materials whose photon adsorption is in the visible or ultraviolet spectra,[22,35] as a result of a series of factors concerning the energy

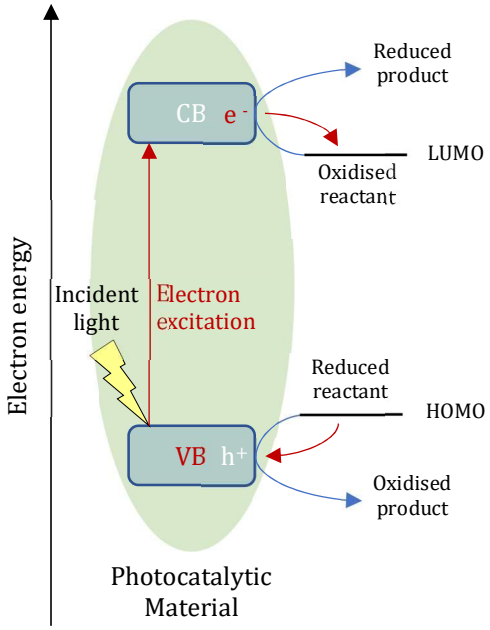


**Figure 1.1** *Simplified scheme of photocatalysis in heterogeneous systems. The incident photon (in yellow) is absorbed by the material (in green), causing an electron of the valence band (VB, in blue) to be excited into the conduction band (CB, in blue). The resulting excited electron in the CB ($e^-$, in red) can be transferred to the LUMO of a reactant on the material surface if the energy of the latter is lower than that of the former, reducing it; similarly, the hole in the VB ($h^+$, in red) can be reduced by an electron from the HOMO of a reactant on the material surface if the energy of the latter is higher than that of the former, leading to an oxidised product of photocatalysis. If neither of these electron transfer processes happen, the electron – hole pair will recombine, reducing the overall efficiency of photocatalysis.*

associated with those band gaps and the availability of solar light on the surface of Earth. The process of photocatalysis is initiated with the absorption of an incident photon on a material through the promotion of one of its electrons from its ground state to an excited state, creating an electron – hole pair. The energies of the excited electron and of the hole direct whether a catalytic reaction can take place on the surface of the material. These energies directly depend on the position of valence band (VB) and conduction band (CB) for heterogeneous systems and on the energies of the highest occupied and lowest unoccupied molecular orbitals for homogenous photocatalysts. If the energy gap is sufficient to drive the reaction and the band position is suitable to an efficient alignment with the energy levels of the reactants at the surface of the catalyst, an electron transfer might take place, leading to a redox reaction.[14,21] Figure 1.1 shows a simplified scheme of a photocatalytic reaction.

It follows from such a mechanism that the size of the band gap of a material is of paramount importance: a small band gap will correspond to a small energy gain for the excited electron, which might be insufficient to drive the reaction or lack the necessary band positioning. On the other hand, a wide band gap will drive the reaction efficiently, but at the same time will limit the amount of solar light available for photon excitation: since only ~5% of the solar radiation hitting the Earth's crust is in or beyond the UV spectrum,[36] materials and molecular catalysts with gaps wider than 3 eV will inevitably harvest the solar spectrum poorly, resulting in equally low catalytic conversion rates. For these reasons, the band gap of a material is often one of the primary focuses of research in photocatalysis, and its precise modification is part of the rationale behind the present work.

*Photocatalytic water splitting*

In photocatalytic water splitting the principles of photocatalysis are applied to the production of molecular hydrogen from a clean and renewable energy source such as solar light. In its original form, the reaction is achieved using a single photocatalyst.[30] If a suitable alignment is reached between the potential of VB and CB and that of the species in solution, water will be reduced by the electron on the CB and oxidised by the hole on the VB, evolving $H_2$ and $O_2$.[22] For this process to happen, the potential of the conduction band edge (CBE) has to be lower than that of the $H^+/H_2$ redox couple (0 V, as the standard hydrogen electrode is the reference for half-cell potentials) and

simultaneously the potential of the valence band edge (VBE) has to be greater than that of the $H_2O/O_2$ redox couple, i.e. higher than 1.23 V vs. NHE.[21] This requirement poses an immediate limitation to the choice of photocatalyst and to the fraction of solar light that can be used to drive the water splitting: any material with band gap lower than 1.23 eV and any light with wavelength above 1000 nm – over 50% than the total solar spectrum – cannot be used. However, a significant overpotential is required to drive the reaction, in excess of the thermodynamic requirement for $H_2O$ redox splitting: driving electrons and holes to the photocatalyst's surface, overcoming the interfacial charge transfer to the adsorbed chemical species and performing the redox reduction all of which are causes for significant energy losses. As a result, the few photocatalysts capable of single-adsorption $H_2$ evolution all show band gaps around 3 eV, corresponding to ultra-violet (UV) adsorption;[30] as mentioned in the previous section, this leads to a major inefficiency of the photocatalytic process, as only ~5% of the solar light irradiation that is not filtered by the atmosphere can be harvested by these photocatalysts.

*Double photon absorption water splitting*

The combination of inefficient solar light harvesting and difficult tuning of the catalytic properties of a material acting simultaneously as both cathode and anode has resulted in few examples of single-photon water splitting catalysts in literature – most notably $TiO_2$ and the GaN:ZnO solid solution[37] – all of which demonstrate wide band gaps and unsatisfactory catalytic efficiencies. However, a different strategy has been implemented in order to overcome the limitations of single photon adsorption photocatalytic water splitting. The so called "Z-scheme" water splitting is a photocatalytic process that involves two photon absorptions on two different photocatalysts, each driving one of the two redox half-reactions.[30,38] This design mimics what happens in the photosynthetic cells of plants and algae, where water is oxidised to $O_2$ as the photosystem II (PSII) absorbs a photon, and the energy from both this and the photon absorption occurring on photosystem I (PSI) is stored by reducing ADP to ATP and $NADP^+$ to NADPH.[14,17] This mechanism is replicated in artificial photocatalysis by coupling two narrow band gap semiconductors – which act as oxygen evolution photocatalyst (OEP) and hydrogen evolution photocatalyst (HEP)

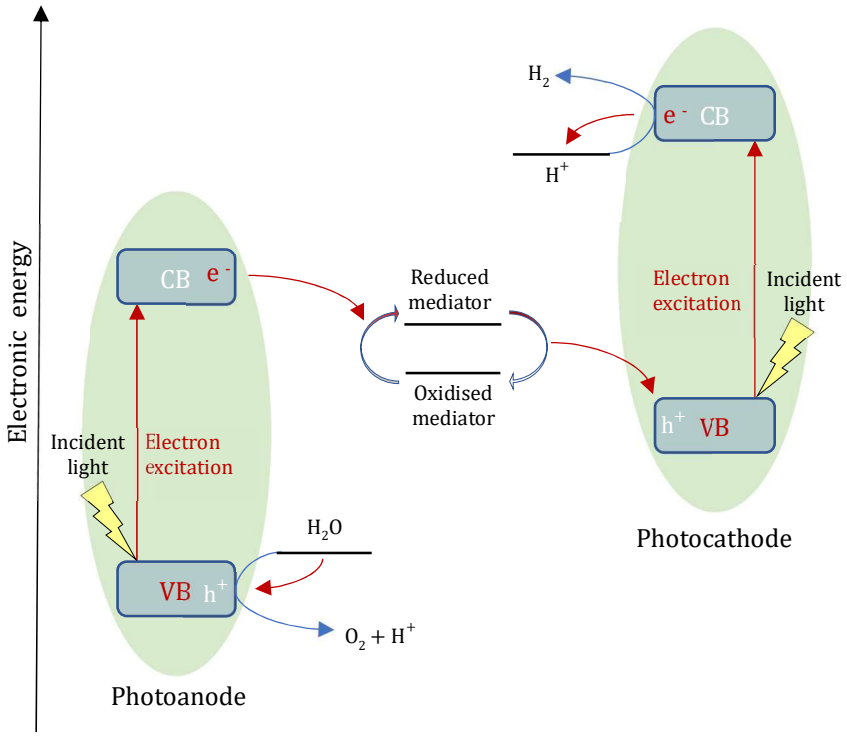


**Figure 1.2** *Design of a Z-scheme photocatalytic process using heterogeneous catalysts and ionic redox mediators. The photocatalytic materials are depicted in green, the blue arrows are the catalytic reactions, and the red arrows indicate the path followed by the electrons. The $e^-$ in the VB of the photoanode are excited to the conduction band of the material by an absorbed photon (in yellow), leaving a hole in the VB ($h^+$, in white). The presence of $h^+$ allows the oxidation of water at the surface of the photocathode, while the $e^-$ in the CB can reduce the redox mediator by transferring to its LUMO. The mediator is then oxidised at the photocathode by a $h^+$ left by the promotion to CB of an $e^-$ by a second photon, which then reduces the $H^+$ in solution to gaseous $H_2$. Since the spontaneous (i.e. non light-driven) movement of electrons is invariably towards lower energy states, it is clear from the scheme how the energy levels of the VB and CB of both photocatalytic materials as well as those of the redox mediator must be carefully chosen in order to obtain the photocatalysis.*

respectively – through a redox or solid mediator capable of transferring electrons between the two catalytic systems. This design, which is exemplified in Figure 1.2, has several advantages: firstly, separating the two half reactions significantly narrows the band gap required, widening the choice of potential catalysts; secondly, decoupling the reactions allows for simpler mechanistic and optimization studies, as the photocatalyst can be used to perform either $H_2$ or $O_2$ evolution using a sacrificial agent; lastly, a double light adsorption increases the maximum theoretical efficiency up to 40%, and can be used to harvest a wider fraction of the solar light spectrum.[17] However, a double absorption design also has drawbacks: while each component can initially be optimised on its own, a fine tuning of the coupling between components is also required; furthermore, the electronic connection between different phases induces

recombination and energy losses, which have to be minimised so that OEP, HEP and redox mediator can work together efficiently.

*Materials for Z-scheme photocatalysis*

Work on Z-scheme photocatalytic designs for water splitting has been drawing the attention of researchers for decades. One of the main research goals is to obtain devices capable of solar-to-hydrogen (STH) efficiencies over 10%, as these would allow for performances comparable to those of solar panels coupled with water electrolysis.[14,17] To increase the efficiency of the process, an additional component is often added to the photochemical reactor: the co-catalyst, which is generally a non-photoactive material deposited on the OEP or HEP to accelerate the chemical reaction of the photoexcited electron or photogenerated hole. The presence of the co-catalyst often leads to significantly higher STH efficiencies, as these materials are designed be good catalysts for the redox reactions needed for hydrogen and oxygen evolution by allowing fast electron transfer between the photocatalytic materials and the species in solution; additionally, co-catalysts can significantly increase the lifetime of the $e^-$-$h^+$ pair after this is created by physically separating them, as photoexcited electrons and holes can migrate from the HEP and OEP to their respective co-catalyst, further improving the chances of a chemical reaction before recombination. An often-used co-catalyst for hydrogen evolution is Pt, deposited directly on the HEP, although cheaper and more abundant Ni-based and Fe-based catalysts have also been developed.[17,39,40]

The different components of the Z-scheme photocatalytic design have often been considered separately, as one of the strengths of this hydrogen evolution process is the variety of materials that can be used in a reactor. The aim of the optimization of a single component is often the minimization of energy losses, which are particularly problematic in relation to the electron shuttle that connects OEP and HEP.[17,30] This connection is in most cases a redox couple in aqueous solution which is reduced by the OEP and oxidised by the HEP, transferring electrons between the two. This set up allows for a relatively simple coupling of separately optimized OEP and HEP materials: theoretically, any three of these components could be coupled together to form a working photocatalytic system as long as the electronic energy of the LUMO of the oxidised state of the mediator lies between the potential of the CB of the OEP

and that of the VB of the HEP, as highlighted in Figure 1.2. However, commonly used redox couples[41] such as $IO^-/I^-$ and $Fe^{3+}/Fe^{2+}$ do not allow for efficient electron transfer due to charge recombination effects and slow reaction rates,[17] limiting the overall efficiency of the Z-scheme. For this reason, solid bridge electron shuttles have also been developed; these are conductive materials with a suitable band alignment that connects the OEP CB and the HEP VB, eliminating the redox diffusion processes correlated with the reaction chain of redox mediators and strongly limiting the possibility of charge recombination.[41,42] For these applications, the use of high-performance materials such as graphene oxide, carbon dots and gold nanoparticles allows for much increased STH efficiencies with respect to comparable heterogenous photocatalytic systems. This, however, comes at the cost of considerably more complex systems, which can prove difficult to optimise: the components of the Z-scheme are no longer separable and the optimization of each of them cannot take place without a simultaneous fine tuning of the connection between them, limiting the applicability of these materials.

*Hydrogen and oxygen evolution photocatalysts*

Much of the research performed on Z-scheme systems has focused on the oxygen evolution and hydrogen evolution photocatalysts.[17,27,30,43] The wide variety of natural and synthetic semiconductors available calls for extensive research effort, while the complexity of the problem – which requires each catalyst to simultaneously possess good absorption properties, efficient charge separation, suitable band position and high catalytic performances – drives researchers to constantly push the boundaries of state-of-the-art photocatalysts. A wide range of materials has been tested for these applications, mostly metal oxides, but also nitrides, sulphides, halides, organic dyes and polymers, all with their respective variants and co-catalysts. Photocatalysts are often first tested in their respective half reaction, using sacrificial agents as either electron or hole acceptors, in order to ascertain their performances in a controlled environment.

Even in such simplified systems, several conditions have to be met in a material for it to be considered suitable as a OEP or HEP; the band position, the electron-hole pair lifetime, and the catalytic activity can all pose limitations to the performances of the photocatalyst, and are therefore the focus of investigation. Band position of the OEP

and HEP materials affect the performances of the photocatalytic system primarily due to the thermodynamic and kinetic limitations of the electron transfer, similarly to the case of single-photon photocatalytic water splitting. For this reason, efficient OEPs show very positive values for the valence band minimum, as it is the case for the metal oxides most commonly used for this application, such as $WO_3$ (~2.7 eV). With the aid of $RuO_2$ and Pt-based co-catalysts, used to help reduce the activation barrier of the water oxidation, tungsten oxide was the first material to be reported as achieving a stoichiometric $H_2$ and $O_2$ production under UV light, in 1997,[44] and under visible light, in 2002.[45] The ability of this material to oxidise water selectively, reducing recombination with CB electrons as well as the redox mediator, further increased the interest on $WO_3$, as this characteristic improves the performances of the $IO_3^-/I^-$ aqueous redox mediator.[17] Other metal oxides have been used as OEPs, such as $TiO_2$, $Ag_3PO_4$, and $BiVO_4$, the latter showing the highest activity in sacrificial cells but showing lower quantum yield in complete Z-scheme systems.[46–48] Another class of materials that has sparked interest is that of oxynitrides, such a TaON.[17] These materials show a smaller band gap and can therefore more efficiently harvest the solar spectrum. However, their intrinsic tendency to promote back reactions such as the oxidation of the material itself rather than $H_2O$ has led to their more efficient use as HEP. TaON is so efficient as a photocathode that it was reported to show the highest quantum yield for an overall Z-scheme water splitting cell, when coated with defective magnesium oxide and coupled to $PtO_x/WO_3$ via an iodide-based redox mediator.[49]

A relatively new avenue of research for hydrogen evolution photocatalysts, as mentioned above, is that of organic materials, primarily in the form of dyes and polymers. The former take inspiration from the relatively well-established work on dye-sensitized solar cells (DSSC) – which make use of the wide and tunable absorption spectrum of certain organic molecules to try and increase the efficiency of solar to electricity conversion[14,17,50] – in order to achieve a similar flexibility in terms of band gap in photocatalytic devices; however, these molecules are often unstable in their oxidised states, which leads to relatively quick degradation during $H_2$ evolution. Similar absorption properties with improved stability have been achieved using polymers such as carbon nitride, a well-known hydrogen evolution photocatalyst on its own terms, the band gap of which can be further tuned by doping with different elements, such as P, B, F, I, S, N or O.[51]

*Graphitic carbon nitride*

Graphitic carbon nitride (g-$C_3N_4$) is a one of the earliest synthetic polymers, being first reported as far back as 1834.[52] Its structure is generally accepted as being composed of heptazine units connected via their three amino groups to form either chains or layers, varying with the synthetic route and the degree of polymerization.[53,54] The polymer is considered stable and nontoxic in all its forms, which further increases its potential as "green" catalyst for sustainable energy conversion. It can be synthetized from a variety of cheap and common precursors, like melamine, dicyanamide, thiourea and urea, obtaining different degrees of polymerization and electronic properties.[17] Despite its very early discovery, graphitic carbon nitride was only reported as an effective hydrogen evolution photocatalyst in 2008.[55] Since then, g-$C_3N_4$ has been tested both as HEP in sacrificial cells and in overall Z-scheme systems, showing promising $H_2$ evolution rates and demonstrating high activity when coupled with $Fe^{3+}/Fe^{2+}$ and $IO_3^-/I^-$ redox mediators and Pt co-catalysts.[40,53,56,57]

Despite its many advantages, the relatively wide band gap of g-$C_3N_4$ (about 2.7 eV) limits adsorption to wavelengths shorter than 460 nm, considerably restricting the portion of solar light that it can harvest. Furthermore, the material displays a small surface area, of the order of 10 $m^2g^{-1}$, which in combination with low charge mobility limits the charge transfer with the redox species in solution, favouring charge recombination.[17,53] Elemental doping has been frequently implemented to try and overcome these limitations, allowing for fine tuning of the material's properties. Elemental doping is a well-established practice in crystalline semiconductors; however, in polymeric systems such as g-$C_3N_4$ the range of synthetic routes and the often amorphous structures introduces several unconventional challenges. Metal doping has generally been introduced in the material as absorbed or deposited metal ions, and has been shown to influence the electronic properties of the material, especially in relation with its absorption spectrum and band alignment.[56] However, the metal-free nature of the polymer has induced researchers to more often focus on non-metal doping. Sulphur, phosphorus, boron and halogens have all been successfully introduced in the material to reduce its band gap and improve its photocatalytic activity. The present work is part of a multidisciplinary research aimed at the investigation of oxygen doping of carbon nitride polymers.

*Structure and electronic properties of carbon nitride-based materials*

Computational techniques such as Density Functional Theory (DFT) are often used to investigate photocatalytic materials as an aid to experimental characterization. Computational aid is especially valuable for heterogenous photocatalysts, as these are often difficult to characterise both in their optical properties and in their structure. The latter is particularly true for polymeric materials, and specifically the structure of g-$C_3N_4$ has long been cause for debate.[54,58] The computational studies reported in this field display a wide range of techniques and theoretical frameworks used. In DFT studies, GGA and hybrid-GGA functionals have been used, making functionals such as PBE and HSE06 the *de facto* standard modelling frameworks for photocatalytic heterogeneous materials, often coupled with plane-wave basis sets.[59–61]

In the present work, a computational study has been performed to investigate the polymeric structure and electronic properties of graphitic carbon nitride after its doping with tunable amounts of oxygen, following input from experimental collaborators in University College London. The structure of the oxygen-doped polymeric carbon nitride derivative was synthetized and characterised by our collaborators, while this study has focused on correlating quantum mechanical calculations with experimental data. Our approach is similar to several other computational studies on analogous materials, in which *in silico* models are often used to clarify the structure of the photocatalyst and its relationship with electronic properties and photocatalytic performances, as highlighted by characteristics such as band gap and charge localization. This investigation will be presented in Chapter 3.

## 1.3 Electrochemical hydrogen evolution

*Water electrolysis*

The advent of ever-cheaper and more efficient solar and wind power has driven scientific interest towards the study of the hydrogen evolution reaction (HER) and the oxygen evolution reaction (OER). These two processes are the cathodic and anodic half-reactions of water electrolysis, which produces molecular hydrogen without the need for oxidation of organic compounds through the electrochemical disproportion of $H_2O$. Water electrolysis has been known for more than a century and has been extensively studied and used in lab-scale applications, but it has found little industrial

success: due to the high running costs compared to fossil-fuel based alternatives, water electrolysis only accounts for roughly 4% of the global $H_2$ production.[22] However, the widespread fear for climate change has been reigniting interest in this reaction in the last two decades, leading to extensive experimental and theoretical literature on the topic. Compared to photochemical water splitting, which was analysed in the previous section, water electrolysis presents the clear drawback of being powered by electricity rather than directly harvesting a renewable energy source, therefore introducing an additional energy conversion step that may lead to energy losses.[11] However, decoupling solar harvesting and hydrogen evolution results in increased flexibility and more efficient electrochemical reactions, as the electrolytic cell does not have the spatial and temporal limitations typical of solar light harvesting and the electrodes can be more efficiently optimized for electrocatalysis. In acidic medium, the HER is the electrochemical combination of two protons with two electrons from a cell cathode to obtain molecular hydrogen, as in the reaction:

$$2H^+ + 2e^- \rightarrow H_2 \qquad E_c = 0.0\ \text{V}\ vs.\ \text{NHE}$$

When combined with the OER:

$$2H_2O \rightarrow O_2 + 4H^+ + 4e^- \qquad E_a = 1.23\ V\ vs.\ \text{NHE}$$

the two half-reactions give rise to the electrochemical water splitting:

$$2H_2O \rightarrow 2H_2 + O_2 \qquad \Delta E = 1.23\ V$$

The thermodynamic potential is constant with pH, electrode material and solution composition, but in practice no gas is evolved when a potential of 1.23 V is applied, and industrial cells use voltages of about 1.8 to 2.3 V in order to obtain significant $H_2$ evolution.[62] The overpotential (η) required to drive the reaction is therefore cause of a significant reduction of the efficiency and a corresponding increase in the amount of energy required to produce a given quantity of hydrogen, which is of about 4.8 kWh/m$^3$ if a potential of 2 V is applied, corresponding to an efficiency just above 60%.[62] In order to make $H_2$ evolution from water a viable energy storage solution for a carbon-neutral world, the efficiency of both anodic and cathodic processes has to be improved. Hydrogen evolution will be the focus of this work, and therefore the cathodic half-reaction of water splitting is more thoroughly analysed in the following section.

*Modelling the hydrogen evolution reaction*

The cathodic reduction of water to molecular hydrogen is a two-step process. Initially, a proton has to adsorb and discharge on the surface of the electrode, resulting in an intermediate state in which a hydrogen atom is chemisorbed:

$$H^+_{(aq)} + e^-_{(cat)} \rightarrow H_{adsorbed}$$

This is called the Volmer reaction, after which the adsorbed hydrogen can desorb either combining with a similarly adsorbed hydrogen on the surface of the electrode, through the Tafel reaction, or with a proton in solution simultaneously with its discharge, through the Heyrowský reaction:

$$H_{ads} + H_{ads} \rightarrow H_{2\,(g)}$$

$$H_{ads} + H^+_{(aq)} + e^-_{(cat)} \rightarrow H_{2\,(g)}$$

in which the subscripts $ads$, $aq$, $cat$ and $g$ stand respectively for *adsorbed* on the surface of the cathode, in *aqueous* solution, from the *cathode* and *gaseous*.

Which of the two desorption steps is the dominant mechanism and whether the rate limiting step is the desorption or discharge heavily depend on the reaction conditions and the material chosen for the cathode.[63,64] Since desorption and discharge are competitive, it has been theorized that a good catalyst for HER will need to balance adsorption and desorption. This principle has found practical application in the so-called volcano plot: if the current density is plotted for several cathodes as a function of their M-H binding energy, a peak in catalytic activity will occur around $\Delta G_{ads} = 0$.[65] For this reason, computational modelling of materials for HER electrodes has often focused on calculating the hydrogen adsorption energy: this quantity, expressed either in terms of $\Delta G_{ads}$ or electronic energy, is relatively simple to calculate and is more accurate than experimental values for M-H binding energy, allowing fine control of the model surface and obtaining easily replicable results.[66] Because of this, a wide variety of materials can be easily benchmarked for the HER, obtaining an adequate qualitative measure of their catalytic activity without the need for often complicated and hardly replicable syntheses.

However, some inherent contradictions of volcano plots have been highlighted. Sabatier's principle and both its early and modern[67] applications in volcano plots are

simple schemes that are based on a solid chemical basis and allow for an early screening of materials, but cannot encompass the full complexity of the reaction and the chemical nature of the M-H bond on different materials. For this reason other descriptors have been proposed, although often unsuccessfully,[66] and computational work often focuses on finer detail of the chemical interaction between material and hydrogen, such as surface coverage or reaction mechanism, in order to obtain more meaningful insight in the catalytic activity of each material. One key success of the volcano plot, however, lies in the accurate prediction of unparalleled activity for d-metals: at the peak of the volcano plot is Pt, which is the most efficient hydrogen evolution catalyst material, requiring only $\eta = 20$ mV in order to evolve $H_2$ with a comparatively high current density of $i = 1$ mA/cm$^2$ in acidic medium.[64,68]

*Catalysts for the hydrogen evolution reaction*

Due to their high performances, platinum-based catalysts are the most commonly used cathodes for lab-scale applications. However, the scarcity and cost of Pt are amongst the reasons for the limited industrial application of water electrolysis,[22,63] as they make the use of such catalysts impractical and expensive for a large-scale use. Cheaper materials are often used as HER electrocatalyst in industrial applications, such as mild steel, which is employed in the Chloro-alkali reaction.[12] However, the overvoltage needed to drive the reaction (up to 1V) is too high for an economically and environmentally sustainable large-scale production of $H_2$. For these reasons, research has been driven towards the development of new catalysts, with the aim of achieving similar performances to Pt – especially in terms of overpotential required – with cheaper, more abundant and more resistant materials.

Several metals have been reported as catalyst for HER, such as Cu, Au, Mo, Pd, Rh, Fe, Ni and Ti. Some of the best results are found for Ni, Fe and Co catalysts, but they suffer from corrosion and passivation[23]. Nanostructured materials[22,69] have been reported in the forms of nanoparticle alloys, doped and supported materials, and heterostructures. Some of these make use of Pt in very small loadings on carbon nanotubes and similar supports in order to maintain the low overvoltage while reducing the costs of the electrode;[70,71] alloys of Ni, Co, Mo and Fe have been reported to improve activity and stability over the pure metals; 2D multi-layered transition metal sulfides can have similar activity to that of Pt; most of these materials still

present major drawbacks that prevent them from replacing Pt in conventional electrolytic cells, but all show promising results and require a significant research effort to optimize their performance, cost and stability.[23,69] One interesting class of materials for this application is that of transition metal carbides, which couple low cost and extreme durability with well-known Pt-like catalytic activity, and have been the focus of extensive research in the past decade.[64,72]

*Transition metal carbides*

Transition metal carbides (TMCs) are a class of materials traditionally known for their hardness and their mechanical as well as chemical resistance. For that reason, they are often the material of choice as coating for high-end stress-resistant materials, such as cutting tools, ultra-high-vacuum turbines and jet engines. In 1973, however, the ground-breaking work of Levy and Boutart highlighted a "platinum-like" catalytic activity in tungsten carbide over several reactions involving hydrogen.[73] From that moment TMCs have been tested and reported as catalysts for a wide range of reactions, either involving hydrogen, such as hydrogenation, water-gas shift, hydro-treatment isomerization and methane reforming,[27–33] or involving oxygen transfer, such as the OER, $CO_2$ reduction and several organic reactions involving the activation or scission of a C-O bond.[75,79–81]

The structure of these materials is well known and understood. All transition metals of groups 4-6 and Fe form at least one stable carbide phase at standard conditions. Groups 4-5 form stable carbides with 1:1 stoichiometry and rock salt structure, although often with defective structures that highlight the higher metal/carbon ratio. Cr, Mo and W form carbides with a variety of structures and stoichiometries, but in all cases and no matter how defective the carbon content is the structure is different from that of the parent metal.[63,82–84] The electronic structure of these material has been investigated experimentally and theoretically, highlighting their promising d-band position and rationalising their catalytic activity towards reactions such as hydrogen evolution from water and $CO_2$ reduction to CO and $CH_3OH$. Several transition metal carbides have been reported for the hydrogen evolution reaction. WC and $Mo_2C$ have been have been the most extensively studied and are reported to show good catalytic activity, although still not comparable to Pt: carbon nanotubes-supported molybdenum carbide has been shown to allow a current density of $i = 1$ mA/cm$^2$ at $\eta = 63$ mV, while

WC showed a relatively high exchange current density of $i_0$ = 0.35 mA/cm$^2$ and an onset potential of $\eta \approx 100$ mV. Even though the latter displays lower activity, it has been extensively used as HER catalyst due to its very high corrosion resistance under acidic condition, which also inspired its use as catalyst support for low Pt loadings, with HER activities more than an order of magnitude higher than the commercial Pt/C catalysts.[71,81,85–87]

*Hydrogen adsorption on early transition metal carbides*

Lately, TiC has also been studied as HER catalyst, both experimentally and computationally.[86,88] Despite its small exchange current density, TiC nanopowder has an onset potential close to 0 V vs. RHE and a good corrosion resistance that make it a potentially interesting material for HER cathodes,[86] and computational studies of the bulk electronic structure of early transition metal carbides have highlighted how some of these show promise for a high catalytic activity of the HER and $CO_2$ conversion.[89] Chapter 4 of this work expands on this knowledge by studying the adsorption of molecular hydrogen over the low-index surfaces of TiC, VC, ZrC and NbC and investigates the correlation between the energetics of adsorption and the activity of the material as a HER electrocatalyst by analysing the thermodynamics of hydrogen coverage on the system.

## 1.4 Carbon dioxide recycling

*Solving the 'carbon problem'*

The increasing popular and governmental pressure to tackle climate change has resulted in political objectives that might not be feasible with current technology, at least within a *business-as-usual* model.[10,12,21] The carbon dioxide targets set in the Paris Agreement and the political objective the European Commission has set to decrease emission by 80% before 2050 are among those, as the "simple" transition from fossil fuels to renewable energy would not be able to yield such results. One often proposed solution to this problem is the capture of $CO_2$ from either exhaust gases or, as a long-term goal, directly from the atmosphere.[12] The practical challenges of $CO_2$ separation are well-known, but the best solution for the disposal of quantities of $CO_2$ in the order of magnitude of the gigatons is still cause for debate. Two of the

strategies that have been designed are the carbon capture and storage (CCS) and the carbon capture and utilization (CCU) schemes. The former has been known for decades and has already been applied by a few countries:[13] after $CO_2$ is captured, natural cavities such as coal beds and depleted oil and gas fields are used to store large quantities of $CO_2$. These technologies had great early success, and several megatons of $CO_2$ are stored every year around the world, but some limitations are preventing them from spreading further.[12] The main issue with CCS scheme is of course that the process is very energy intensive, leading to only marginal improvements in carbon emissions as the captured $CO_2$ is balanced by a further use of fossil fuels necessary to store it. On top of this, concerns over the long-term safety of natural fields in terms of environmental impact and permanence of captured $CO_2$ within the confinement have limited the applicability of this strategy.[12]

The opposite strategy involves the recycling of $CO_2$ into the products that are currently synthesised using fossil carbon. Using carbon dioxide as a building block for chemicals is after all the source of many of the fossil fuels we use now, as photosynthetic organisms have fixated it and used it as energy storage for millions of years, by converting $CO_2$ and $H_2O$ in glucose and then into the unlimited variety of organic matter that powers most of life on our planet.[14,21,30] The most obvious way of recycling atmospheric $CO_2$ would therefore be through biomass, which is harvested and then converted into fuels and chemicals that can be used in the same processes currently used for fossil fuels while reducing their carbon footprint. This, however, has been criticised as an unrealistic scenario, as biomass production might be in competition with food production for the use of farmland, preventing its application on a global scale;[11] furthermore, while the photosystems responsible for the light harvesting and water splitting in plants and algae are extremely efficient, their further use to make glucose and then convert it into the chemicals needed by the organism is not, driving the total efficiency of biomass down to 0.1-1% in most agricultural crops[14,29] and resulting in a high environmental footprint for its use, as highlighted by life cycle assessments.[11] Carbon capture and utilization designs therefore aim to similarly fixate $CO_2$ into reduced carbon-based chemicals while significantly improving the efficiency, applicability and scale of such processes.

*Synthetic carbon utilization*

The synthetic fixation of $CO_2$ into useful fuels and chemicals can be performed through two main strategies: introducing $CO_2$ into existing molecular frameworks without changing its oxidation state, or reducing the $CO_2$ into base chemicals that can be further processed.[11,12] The former strategy is already used in several industrial applications as it generally involves strongly exothermic (inorganic carbonates) to mildly endothermic (urea and organic carbonates) reactions; this is a well-established way of reducing the environmental impact of certain chemical processes. However, the utilization of $CO_2$ in such processes in 2014 was of 200 Mt/y, only 0.62% of the global carbon emissions,[12] and the global demand of chemicals is not sufficient to drive a significant expansion. Contrary to that, the reduction of $CO_2$ leads to highly-valued chemicals and fuels, mostly CO, $CH_3OH$ and $CH_4$;[12,80] these are all strongly endothermic reactions that require considerable amounts of energy to be performed, and that ultimately store renewably-generated energy into the fuels and chemicals produced.

Renewable reduction of $CO_2$ can be done through systems that harvest and input the energy in a single step – as in solar thermal concentrators and photocatalytic systems – in two steps – as in inverse methanol fuel cells powered by fossil-free energy and through chemical reduction by photosynthetically produced hydrogen – or through a three-step process in which renewable energy is harvested, converted into $H_2$ through water electrolysis and finally into fuels and chemicals through the reduction of $CO_2$ with hydrogen.[11] While it would be obvious to look at single-step and two-step processes to reduce the efficiency losses correlated with energy conversion, it is the latter strategy that is currently the most primising.[11] One- and two-step processes are in fact limited by either their scale or the photochemical complexity of the systems involved: size, efficiency and resistance to very high temperatures of all components are an issue for solar concentrators; microorganism using light to convert $CO_2$ to short chain organic molecules have shown promising results but are a new field that will require further research development before it can be scaled-up; similar observations can be pointed out for the Z-scheme photocatalytic systems, which still require a consistent research effort to obtain the efficiencies required for large-scale industrial application; and finally, reverse methanol fuel cells and other means of electrochemical reduction of $CO_2$ share with 3-step chemical reduction the advantage

of being potentially powered by any fossil-free energy source, but suffer from the even higher overpotentials required and more complex catalytic reactions on the electrodes.[11,25,90-92] On the other hand, the three steps of renewable energy harvesting, water electrolysis and catalytic $CO_2$ reduction with $H_2$ all make use of well-established science, resulting in a solar-to-fuel conversion that can be higher than 10% when state-of-the-art technology is used.[14] However, as mentioned in the previous sections and as it will be highlighted in the rest of this work, several challenges remain, and among those the design of a catalyst which combines efficiency, cost and selectivity is paramount.

*Activity and selectivity in catalytic $CO_2$ conversion*

Several processes have been proposed for the recycling of $CO_2$ once it has been captured using renewably generated $H_2$, most of which make use of technology that is already employed by the chemical industry. The closest target chemical for $CO_2$ reduction is of course CO. This reaction can be performed using either the reverse water gas shift process (RWGS), which produces CO and $H_2O$ from $CO_2$ and $H_2$, or the dry reforming of methane, which produces CO and $H_2$ from $CO_2$ and $CH_4$. Both reactions can be readily implemented into existing plants, but further studies are needed to increase their efficiency, especially with respect to the Fischer-Tropsch (FT) catalysts currently used for RWGS reactions.[11] Furthermore, CO is a highly valued base chemical,[74,93] but has to be further processed in order to be used in fine chemistry or as fuel. Further down in the reduction series of $CO_2$ are methanol and methane. Methanol is often produced from syngas over Cu/ZnO-based or iron oxide catalysts,[11,94] but the chemistry of these systems is very complex and often determined by defective and multi-phasic morphologies which limit our understanding of the process.[94] Direct $CO_2$ to methanol routes have also been proposed, using molybdenum sulphide clusters ($Mo_6S_8$) and Pd-based catalysts supported on carbon nanotubes.[11,95] Both FT-based and direct routes to methanol have also been reported, with either B-based or Ru-based catalysts, at lower temperatures.[11,94] Finally, $CO_2$ can be converted to methane, short-chain olefins and other short-chain organic fuels such as dimethyl ether and formic acids through various routes, either involving FT processes, through direct hydrogenation on a suitable catalyst, or electrochemically.[96–99]

For many of the routes explored, selectivity is an issue that must be tackled. Such complex reaction processes can often lead to multiple products, but separation can be complex and expensive, leading to a less valuable product. For this reason, several studies have investigated the product selectivity of $CO_2$ reduction over various catalysts. For example, $Mo_2C$ and $Fe_3C$ were demonstrated as viable catalysts for the RWGS reaction, with better performances than their respective metal sulphides.[95] Homogeneous catalysts for the direct, low temperature synthesis of methanol have been proposed, both complex-based and metal-free;[11,90] the former makes use of a three-step cascade process based on Ru- and Sc-complexes to produce methanol through a formic acid intermediate, while the latter exploits the concept of frustrated Lewis pairs to obtain $CH_3OH$ with 100% selectivity.

*Computational studies of carbon dioxide reduction*

Theoretical studies have often focused on either the activation of $CO_2$ or the mechanism for reduction, trying to connect such data with the experimental results on activity and selectivity. $Mo_2S$ was shown experimentally to have a strong selectivity towards CO, with a ratio of 154:1 over $CH_3OH$, and its performances could be correlated with its computed oxygen binding energy.[80] Other theoretical studies were performed on a copper catalyst with metal oxide support, showing that hydrogen binds preferentially on the metal while $CO_2$ favours adsorption on the oxide, predicting higher activity at the interface.[95] Adsorption studies have also been performed on $Cu_2O$, $In_2O_3$ and $TiO_2$,[100] highlighting the effect of oxygen vacancies and surface morphology on carbon dioxide activation. Several reaction pathways have been investigated, making it possible to identify two main paths, which are selected by the site of first hydrogenation of $CO_2$: if this is on the carbon atom, producing an HCOO species on the catalyst's surface, the first step is rate determining and the catalyst cannot catalyse the RWGS reaction as the product will necessarily be hydrogenated; if the first hydrogenation happens on the oxygen, both CO and $CH_3OH$ formation are possible, depending on the relative rate of CO desorption and CO hydrogenation, as the latter will be the rate determining step on methanol formation.[94] Even on the same material, different mechanisms have been proposed in some cases: $CO_2$ methanation on Cu was proposed to go preferentially through CHO if the metallic surface is exposed to vacuum but through COH if a continuum solvent model is used,[100] highlighting the difficulties related to the modelling of such complex systems. Finally,

computational catalyst screening studies have also been performed, but the lack single reliable and widely-accepted descriptor – even if the oxygen binding energy has been proposed for RWGS reaction in the aforementioned paper – has limited their applicability.[80,100]

TiC has been proposed for $CO_2$ reduction, both as a catalyst and as catalyst support.[79,101–103]. However, not as much computational effort has been spent on group IV TMCs as on other carbides such as $Mo_2C$.[81,104] For this reason, and building on our previous work on the hydrogen adsorption on group IV TMCs[101] as well as on the several studies of the bulk properties and catalytic reduction of $CO_2$ on TMCs,[89,102] Chapter 5 of this work will be focused on the $CO_2$ reduction on TiC and ZrC.

# Chapter 2:
# Computational Methodology

## 2.1 Density functional Theory

*Solving the Schrödinger equation*

The computational investigation of metal carbides and carbon nitride derivatives has been performed using accurate *ab initio* methods. These techniques use quantum mechanics to obtain a mathematical representation of the behaviour of electrons in molecules or extended materials. This strategy enables computational chemists to investigate the geometry, electronic properties and chemical reactivity of the systems examined. The main objective of the use of computational power in *ab initio* methods is to obtain an approximate, iterative solution of the time independent Schrödinger equation:

$$H\psi = \varepsilon\psi \tag{1}$$

where H is the Hamiltonian operator, ψ is the wave function or eigenstate of the system and ε is the respective (ground-state) eigenvalue for the energy. The Born-Oppenheimer approximation is used to decouple the movement of electrons and nuclei, allowing for the classical treatment of the latter over a potential energy surface (PES) given by the quantum mechanical interactions of the electrons between each other and with the nuclei, at each given position of these. This results in the equation:

$$[T_e + V_{eN} + V_{ee}]\psi = \varepsilon\psi \tag{2}$$

in which $T_e$ is the kinetic operator of the electrons, $V_{eN}$ is the potential operator relative to the interaction of each electron with all the nuclei, and $V_{ee}$ is the potential operator relative to the interaction of each electron with all other electrons. Since no analytical solution to $V_{ee}$ is known, *ab initio* software uses iterative numerical solutions to the Schrödinger equation which are approximations of the exact solution obtained either through systematic improvement of averaged interaction (post-Hartree Fock methods) or through approximation of the exchange and correlation energy within Density Functional Theory (DFT).

In DFT, the main objective of the calculation is the solution of the Kohn-Sham equations:

$$\left[-\frac{1}{2}\nabla^2 + v_{ext}(\boldsymbol{r}) + v_H(\boldsymbol{r}) + v_{xc}(\boldsymbol{r})\right]\varphi_i(\boldsymbol{r}) = \varepsilon_i\varphi_i(\boldsymbol{r}) \quad (3)$$

In this equation the potential operating on each electron is divided into three components: $v_{ext}(\boldsymbol{r})$ is the operator related to the interaction between electron $i$ and the nuclei; $v_H(\boldsymbol{r})$ is the coulombic interaction between electron $i$ and the average electron density due to all other electrons; finally, $v_{xc}(\boldsymbol{r})$ is the exchange and correlation potential due to the dynamic interaction of electron $i$ to all other electrons. Note that these operators are no longer operating on the wave function as is, but on the electron density of the system, $\rho[\boldsymbol{r}] = |\varphi_i|^2$; this is possible thanks to the Hohenberg-Kohn theorem which demonstrated the biunivocal relationship between the two quantities and therefore between $\rho[\boldsymbol{r}]$ and the properties of the system. The Kohn-Sham (KS) equations are thus processed through a self-consistent field (SCF) cycle in which the mutual dependency of energy eigenvalues and electron density is solved iteratively making use of the variational principle.

As a result of the terms included in the electronic Hamiltonian of the KS equations, the energies of all terms except for $v_{xc}(\boldsymbol{r})$ can be calculated exactly. In other words, all unknown interactions are included in the $v_{xc}(\boldsymbol{r})$ term. For this reason, DFT could theoretically lead to an exact solution to the Schrödinger equation if the exact $v_{xc}(\boldsymbol{r})$ was known; even though this is not the case, DFT achieves the best accuracy of all techniques for its computational cost,[105] although its precision and accuracy are strongly influenced by the choice of exchange and correlation functional $E_{xc}[\rho]$.

*The exchange and correlation functional*

The simplest form of $E_{xc}[\rho]$ is called Local Density Approximation, or LDA. It was first introduced with the Kohn-Sham equations and it is based only on the total electron density and on the exact solution for the exchange and correlation potential in a uniform electron gas. While this is a crude approximation, the results are often useful for solid systems and have been employed for such systems with some success.[106,107] A more nuanced approach is obtained by including the gradient of the electron density in the calculation of $E_{xc}[\rho]$. This is the approach at the basis of Generalized Gradient Approximation (GGA) functionals, which are currently commonly employed in

solid-state calculations as a consequence of their computational cost similar to LDA functionals but showing significantly more accurate performances. A wide variety of GGA potentials is now available, with PBE and its variations such as RPBE and PBEsol being among the most commonly used for solid state periodic systems. In this work we will make use of the PBE functional.[108] This is a non-empirical functional, meaning that its functional form and the parameters used for its construction rely on physical constraints rather than on fitting over a given set of known systems. This allows for wider and more reliable applicability on a wide range of systems, rather than being limited to systems similar to those it was fitted to. The exchange and correlation functional is calculated based on the equation:

$$E_{XC}^{PBE}[\rho_{\uparrow}, \rho_{\downarrow}] = \int d^3r \rho(\boldsymbol{r}) \epsilon_X^{unif}[\rho(\boldsymbol{r})] F_{XC}(r_s(\boldsymbol{r}), s(\boldsymbol{r}), \zeta(\boldsymbol{r})) \quad (4)$$

where $\zeta(\boldsymbol{r})$ is the spin polarization, $r_s(\boldsymbol{r})$ is the Wigner-Seitz radius, $s(\boldsymbol{r})$ is the reduced density gradient, and $F_{XC}$ is the enhancement factor of the unified exchange hole $\epsilon_X^{unif}$.

Further along the "Jacob's ladder" of DFT potentials[105] are the hybrid potentials. These expressions for $E_{xc}[\rho]$ improve on GGA using explicitly calculated Hartree-Fock exchange from wave-function based *ab initio* techniques and mixes it with analytical functionals for exchange and correlation. This approach allows for the creation of functionals which are more accurate than GGA, especially when targeted over a specific class of materials, such as the well-known case of B3LYP for organic materials. The improved accuracy, however, comes at a cost: the resolution of a further series of Fock equations leads to a much increased computational cost. For this reason, hybrid functionals have not been used in this work, as they are usually considered too computationally demanding for reactivity studies in a periodic-DFT framework.

## 2.2 plane wave basis set

### *Bloch theorem*

The electronic structure of a crystalline material, especially in metals, is strongly influenced by the delocalization of electrons and the periodic nature of the potential applied on each electron by the lattice of nuclei. In order to model these effects, the

system is placed in a unit cell of suitable symmetry and then replicated in all directions in space. This forms a periodic Bravais lattice in which the atoms are replicated indefinitely; atomic planes in real space can be identified as points in reciprocal space, generating a corresponding reciprocal lattice matrix. Since the arrangement of atoms is periodic, the solution to the Schrödinger equation will also be periodic, hence the potential $U(\boldsymbol{r})$ applied on each electron at each point can be written as:

$$U(\boldsymbol{r}+\boldsymbol{R}) = U(\boldsymbol{r}) \tag{5}$$

in which $\boldsymbol{R}$ is the lattice vector of the Bravais lattice describing the symmetry of the material. In order to adhere to this requirement, the functional form chosen for the basis set used to describe the behaviour of electrons in a periodic system can be chosen as a plane wave, a periodic function with period equal to that of the underlying Bravais lattice:

$$\psi_{n\boldsymbol{k}}(\boldsymbol{r}) = e^{i\boldsymbol{k}\boldsymbol{r}} u_{n\boldsymbol{k}}(\boldsymbol{r}) \tag{6}$$

where $u_{n\boldsymbol{k}}(\boldsymbol{r}) = u_{n\boldsymbol{k}}(\boldsymbol{r}+\boldsymbol{R})$ is the periodic potential and $n$ and $\boldsymbol{k}$ are two quantum numbers identifying the solution to the Schrödinger equation, specifically the band index and the wave vector. The two quantum numbers give rise to the traditional picture of the band structure of a crystalline material as a family of continuous function of energy $\varepsilon_n(\boldsymbol{k})$, as $n$ identifies each function while $\boldsymbol{k}$ varies continuously over all the reciprocal space within the first Brillouin zone, i.e. within the reciprocal unit cell.

*Pseudopotentials and plane wave DFT*

As implied in the Bloch theorem, each $n$ and $\boldsymbol{k}$ define a single plane wave the value of which varies throughout the whole unit cell. Nonetheless, the variations of potential surrounding the atomic sphere region around each nucleus of the unit cell are generally more complex than those in the interstitial region, and account for a more significant portion of the energy. Owing to the behaviour of the core electrons, high computational cost and difficult convergence are faced when the Kohn-Sham equations are solved using a pure plane-wave basis set. In order to solve this problem, the so-called pseudopotential approach is used. This method is based on separating core and valence electrons, and substituting the nuclear potential and the potential due to core electrons with a suitable pseudopotential which has the same effect on valence electrons – i.e. which presents the same solutions to the Schrödinger equation:

$$H\psi_{\boldsymbol{k}}^{v} = \varepsilon_{\boldsymbol{k}}^{v}\psi_{\boldsymbol{k}}^{v} \tag{7}$$

in which $\psi_{\boldsymbol{k}}^{v}$ is the pseudowavefunction of the system in which only valence electrons are explicitly considered. While this approach limits the accuracy of the model by not calculating the energy and the wavefunction of core electrons, the success of this approach stems from the fact that the resulting potential is generally accurate and weak, allowing for the efficient use of a plane wave basis set to describe the resulting valence electrons pseudo-wavefunction. This approach has been further optimized, especially for first-row elements and *3d* transition metals, in the projector augmented-wave method (PAW).[109,110] This methodology, which is used for all calculations in the present work, makes use of localized atom-centred charges, so that better convergence for elements showing highly localized orbitals can be achieved.

Obtaining information on the charge density $\rho(\boldsymbol{r})$ requires the integration of the pseudowavefunction over all possible wave vectors. To simplify and speed up this calculation a grid-based approach is used, evaluating the energy at specific $\boldsymbol{k}$-points.

$$\rho(\boldsymbol{r}) = \int |\psi_{\boldsymbol{k}}(\boldsymbol{r})|^2 d^3\boldsymbol{k} \approx \sum_{\boldsymbol{k}} |\psi_{\boldsymbol{k}}(\boldsymbol{r})|^2 \tag{8}$$

In the resulting Kohn-Sham equations, an infinite number of wavevectors could be used to describe the pseudowavefunctions, but their coefficient decreases as the square modulus of the wavevector $|\boldsymbol{k}|^2$ is increased. To keep the calculation efficient, a maximum value for $|\boldsymbol{k}|^2$ is set, although generally the corresponding cut-off energy $E^{cut} = \frac{\hbar^2}{2m}|\boldsymbol{k}|^2$ is quoted. Since this value is primarily element-dependent, when plane wave basis sets built into commercial software are used a suggested cut-off energy is often quoted, as it is the case for the VASP code used in the present study. It is also possible, however, to ensure the accuracy of the calculations by executing a convergence study, verifying the change in energy of a chemically significant system with a varying energy cut-off.

## 2.3 Exploring the potential energy surface

The Born-Oppenheimer approximation results in the decoupling of electronic and ionic movements so that the electronic Schrödinger equation can be more readily

solved. As a result, the nuclei can be moved along a potential energy surface (PES) correlated to the electronic energy of each atomic configuration using the laws of classical mechanics. In this section we will discuss how the PES can be efficiently explored in order to obtain accurate structures and the solution to several chemical problems.

*Dispersion interactions*

The PES is a classical model of the forces that act on each atom within the investigated system. Once the electronic energy of a specific ionic configuration is obtained from the *ab initio* DFT cycle, the PES can be further improved in order to obtain a more accurate description of the system. One such approach concerns multipole-induced long-range correlative interactions, which are inherently hard to include in DFT due to the local nature of the theory. Dispersion interactions have been shown to be relevant in many cases in periodic-DFT, especially when surface reactivity is involved, so it was considered necessary to include dispersion correction in all calculations performed for this work. Of the various strategies that have been proposed for the inclusion of dispersion forces in DFT calculation, the one proposed by Stefan Grimme and coworkers in 2010[111] known as DFT-D3 has been chosen for this work.

The DFT-D3 method is a correction applied to the energy after the SCF cycle of the quantum mechanical calculation has been performed, thus not affecting the shape of the electron density but only that of the PES. The energy of each point on the PES is therefore given by the equation:

$$E_{DFT-D} = E_{KS-DF} - E_{dispersion} \quad (9)$$

The dispersion correction is calculated as a sum of contributions from all atom pairs and triples in the system within a given cutoff radius, using coefficients which depend on element and immediate chemical environment of each atom. This approach allows a consistent description of dispersion forces in a wide variety of systems while limiting the computational burden of the correction.

*Geometry optimization*

What has been described until now is the procedure which leads to the calculation of the energy of a single atomic configuration. The electronic energies of all possible ionic configurations give rise to the PES; this can be explored in order to find

chemically meaningful configurations such as the global minimum, local minima and saddle points, which correspond respectively to the most stable phase of a given atomic set, any other stable configuration of the same set and the transition states linking two of those. *Ab initio* software packages use a variety of algorithms to locate local minima of the PES around the input geometry, which generally make use of the forces acting on the atoms, i.e. by calculating the first derivative of the energy with respect to all degrees of freedom. Multiple line searches are then operated iteratively, bringing the system progressively closer to the minimum, and each successive direction can be chosen through various methods. The most common optimization algorithms are steepest descent, conjugate gradient, and Newton-Raphson: the first always selects the largest energy gradient for the line search of each minimization step, while the latter two use more nuanced equations for the choice of direction in order to obtain fast convergence. The minimum is identified through the first and second derivative of the energy with respect to the position of the atoms:

$$\frac{\partial E}{\partial x_i} = 0; \ \frac{\partial^2 E}{\partial x_i^2} > 0 \tag{10}$$

The search is always operated iteratively until a position sufficiently close to a minimum (as specified by a convergence limit) is located.

*Frequency calculations*

The second derivative of the energy of an atomic system with respect of the position of its atoms is the Hessian matrix. This matrix is of paramount importance in the calculation of vibrational frequencies and transition state energies, as it relates to the response of the system to the forces applied on each atom and to its position on the potential energy surface.

The Hessian matrix can be calculated using the finite differences method. In this approach, each atom is displaced in the three Cartesian directions and the forces are determined in the new position for each displacement, progressively filling the matrix. Once calculated, the Hessian matrix allows for the calculation of the eigenvectors and eigenvalues of the dynamical matrix, corresponding to the displacements and energies correlates to each vibrational mode. These vibrational modes are also correlated to the position of the system in the PES; specifically, imaginary vibrational modes are

correlated to the directions of the PES in which the second derivative of the energy is zero. As a result, their number, displacement and energy can be used to obtain information on whether the system is in a minimum of the PES (all vibrational modes are real), on a saddle point (all but one vibrational modes are real) or in another position, and in certain cases to help locate a transition state, as explained in the next section.

*Transition state search*

Other important information that can be found through the exploration of the PES is correlated with the energy required to transition from one minimum energy configuration of the investigated system to an adjacent one. According to transition state theory (TST), the rate of a reaction is correlated with the difference in Gibbs free energy between the reactants and the transition state, between which a quasi-equilibrium state is established:

$$k^{TST} = Ae^{-\frac{E^{TS}-E^{react}}{k_B T}} \tag{11}$$

where $E^{TS}$ is the energy of the transition state and $E^{react}$ that of the ground state of the reactants. The transition state itself is defined as the highest saddle point found on the minimum energy path of the PES connecting reactants and products. As a result, saddle points acquire a central role in answering several chemical questions and are the focus of many PES explorations. Nonetheless, locating saddle points poses several problems: saddle points are identified as points in the PES in which the first derivative of the energy is zero while its second derivative is positive in all but one direction. In mathematical terms, this is expressed as:

$$\frac{\partial E}{\partial x_i} = 0; \quad \frac{\partial^2 E}{\partial x_i^2} > 0 \Big|_{i \neq \tau}; \quad \frac{\partial^2 E}{\partial x_\tau^2} < 0 \tag{12}$$

Geometrically, this corresponds to saddle points being minima in all but one direction, along which they are a maximum. Several different methods have been reported for finding saddle points. In this work, the nudged elastic band (NEB), climbing image nudged elastic band (*c*NEB) and dimer methods have been used.

The elastic-band-based methods aim to identify the minimum energy path (MEP) between two images of the system. Along this path, the energy is stationary in all

directions but the one identified by the path itself; as a result, the transition state is simply the highest point along the MEP, i.e. the highest point along the reaction coordinate. In these methods, several images of the system are generated by (usually linear) interpolation between the PES minima corresponding to reactants and products of a single reaction step. Spring forces connecting each pair of subsequent images are generated, and the energy of all images is relaxed simultaneously taking into account the forces applied by these springs, which allow the images to converge towards the minimum energy path. The nudged elastic band (NEB) method slightly modifies this protocol in order to obtain a more accurate description of the MEP. At each iteration of the relaxation, the tangent to the reaction coordinate at each image is calculated; of the forces owing to the PES, only the contribution in the direction perpendicular to the tangent is considered; for the forces owing to the springs, instead, only the contribution in the direction parallel to that tangent is considered. Using this methodology the relaxation towards the MEP of the images is not hindered by the presence of the springs and the PES does not push all images towards the initial and final states of the reaction. Once all images are on the MEP, the saddle point can be located using the climbing image NEB (*c*NEB) method. This procedure eliminates the spring forces around one or more of the images of the system (generally the one with highest energy) once convergence to MEP is obtained, instead inverting the force parallel to the tangent to the MEP. This way a simple minimization of the energy of that image moves it to the closest saddle point on the MEP.

A completely different approach is used by the dimer method. This method makes use of the harmonic approximation of TST:

$$k^{hTS} = \frac{\Pi_i^{3N} \nu_i^{init}}{\Pi_i^{3N-1} \nu_i^{TS}} e^{-(E^{TS} - E^{react})/k_B T} \tag{13}$$

In this harmonic approximation, $N$ is the number of atoms and $\nu_i$ are the normal modes of vibration, 3N for a minimum and 3N-1 for a saddle point. The resulting imaginary mode of vibration, calculated in a system close to the geometry of the transition state, is considered as an estimate of the reaction coordinate and followed in order to find the saddle point.

## 2.4 Computational details

*Ab-initio software parameters*

All calculations reported in this thesis were performed within the framework of periodic density functional theory using the VASP code (Vienna Ab-initio Software Package) version 5.4.1.[112] Electrons were described using projected augmented wave (PAW) method[109] for core shells and plane waves for valence. The Perdew-Burke-Ernzerhof (PBE) functional[108] was used to approximate exchange and correlation interactions in the framework of generalized gradient approximation (GGA). Additionally, long range interactions were modelled using the Grimme D3 dispersion method.[111] All energies are converged within a cutoff of 520 eV and an electronic self consistent field (SCF) threshold of $10^{-5}$ eV. Convergence was determined using the tetrahedron method, implementing Blochl corrected smearing.[113] All parameters were benchmarked in order to optimise computational time and accuracy for calculations.

*Formic Acid Treated Polymeric Carbon Nitride*

The FAT-PCN polymers investigated in Chapter 3 of the present work were modelled as bulk oxygen-doped graphitic carbon nitride by modifying a high accuracy structure for g-$C_3N_4$, obtained through neutron diffraction, which was taken from the work of Fina *et al.*[54] through the Inorganic Crystal Structure Database. Each unit cell is organized in two planar layers accounting for a total of 4 linear polymeric chains, each composed of 2 heptazine units, 2 linker groups and 2 terminal groups. In the g-$C_3N_4$ (FAT-0) model, all these 16 groups contain nitrogen, in the form of -NH- for linker groups and -$NH_2$ for terminal groups. In the oxygen-doped (FAT-0.1 to FAT-2.0) models, 4 such groups are modified to introduce oxygen, replacing the previous linker and terminal groups with -O- and -OH respectively. In each FAT model different groups are modified, in order to highlight the effect of local oxygen arrangement on the electronic properties of the material. These structures are compared to previous models for similar polymeric materials from the work on ONLH (oxygen- and nitrogen-linked heptazine) from Wang *et al.*[35] All calculations were performed using a 5x5x5 K-points matrix in the reciprocal space with no spin polarization.

The formation energy for each unit cell has been calculated as the difference between the energy of the supercell and the energy of the compound elements divided by the number of atoms, via the formula:

$$\Delta_f E = \frac{E_{polymer} - \sum E_i n_i}{N} \quad (14)$$

in which $E_{polymer}$ is the energy of the polymer supercell; $E_i$ and $n_i$ represent the energy of an atom of each element present in the polymer in its elemental state and the number of atoms of that element in the supercell, respectively; N is the total number of atoms in the supercell, 144 for g-$C_3N_4$ and 140 for all FAT models. The elemental states considered are graphite for C and their respective diatomic molecules in vacuum for H, N and O. Their energies have been calculated within suitable unit cells using the same parameters as described above for the polymer supercells.

*Transition metal carbides*

The surfaces of the transition metal carbides (TMCs) studied in Chapter 4 and 5 of the present work were simulated by 2x2x3 supercell slab models cutting the bulk along the (001), (011) and (111) planes, as previously reported by Quesne *et al.*[85] Each slab has 6 atomic layers and 16 atoms per layer. The (001) and (011) surfaces are created so that they preserve bulk stoichiometry, resulting in an equal number of carbon and metal atoms being exposed to the vacuum. Conversely, the (111) plane is parallel to carbon and metal atomic layers, resulting in two possible surface terminations that respectively expose carbon and metal atoms to the surface. Such a protocol has been applied previously to TMCs and has been shown to describe accurately the electronic and structural properties of the (111) surfaces, as will be further discussed in Chapter 4.[85] To avoid interaction along the axis perpendicular to the surface, the lattice parameter was increased by 12 Å in such direction. A 5x5x1 K-points reciprocal lattice matrix was generated using the Monkhorst-Pack method. Spin polarization was allowed for the determination of the energy of all structures except for the $H_2$ reference molecule. The energy of the system was minimized by keeping the cell parameters fixed at their bulk-optimised value and allowing relaxation of all atoms minus those belonging to the 2 bottom layers of the model slab, which were kept fixed. The minimum energy structures were found using a built-in DIIS algorithm with a convergence force threshold of $10^{-2}$ eV/Å. The energies of molecular $H_2$, $CO_2$, CO,

and $O_2$ have been used as reference for adsorption energies on transition metal carbide slabs. These calculations have been performed using a single γ-point K-point mesh and the same cut off energy as all other calculations within a suitable unit cell, optimised as to minimise the interaction between neighbouring images.

In Chapter 4, interaction energies between the different surfaces and hydrogen were compared using adsorption energy ($E_{ads}$) as calculated by:

$$E_{ads} = \frac{1}{n} * \left[E_{slab+nH} - \left(E_{slab} + \frac{n}{2}E_{H_2}\right)\right] \quad (15)$$

where $E_{slab+nH}$ is the energy of the hydrogenated slab, $E_{slab}$ and $E_{H_2}$ are the energies of the pristine surface and isolated $H_2$ respectively, and $n$ is the number of hydrogen atoms involved in the adsorption. By normalizing by $n$, we consider $E_{ads}$ as the adsorption energy per atom instead of the total energy change in the system.

Further analysis of the coverage state of the slabs requires a measure of the trend of the adsorption energy per atom with coverage, which we define through:

$$\Delta E_{(a-b)} = E_{ads}\left(\theta = \frac{a}{m}\right) - E_{ads}\left(\theta = \frac{b}{m}\right) \quad (16)$$

where $a$ and $b$ are the number of hydrogen atoms adsorbed on the slab, $m$ is the total number of available adsorption sites on the slab and $\theta$ is the coverage in terms of monolayers (ML).

In Chapter 5, since different species are present in the model and no study of the coverage state of the surface is performed, the adsorption energy has been calculated for the whole model, from:

$$E_{adsorbed} = E_{slab+mol} - (E_{slab} + E_{mol}) \quad (17)$$

where $E_{mol}$ is the energy of the isolated molecule and the $adsorbed$ species can be $CO_2, CO, O, H, HCOO$ or $COOH$, or their combinations. Reaction and activation energies have also been calculated for certain steps of the catalytic reduction of $CO_2$ on the surface of transition metal carbides, using the following equations:

$$E_r = E_{product} - E_{reactant} \quad (18)$$

$$E_a = E^{TS} - E_{reactant} \quad (19)$$

Where $E_{product}$ is the energy of the final state of the reaction, $E_{reactant}$ is that of its initial state, and $E^{TS}$ is the energy of the transition state.

## 2.5 Data analysis

*Bader charge analysis*

Atomic charges were calculated for specific systems through a Bader charge analysis.[114] This approach is based on an analysis of the charge density around each nucleus: each atom is described by a Bader volume, containing a single charge density maximum and terminating with a charge density minimum in the direction normal to the separating surface. The Bader partitioning does not necessarily result in biunivocal correspondence between Bader volumes and atoms, but presents the advantage of being based on charge density, a quantity which is easily accessible in both computational and experimental chemistry, and in the former case it does not depend on the choice of basis set used. In this work, the implementation of Henkelman and co-workers[115,116] has been used, which is based on a grid-based analysis of the charge in the unit cell.

*Density of states calculations and the work function*

The density of states (DOS) in a material is the density per unit of volume and energy of solutions to the Schrödinger equation, i.e. the density of energy levels available to electrons. This quantity is of primary importance in semiconductors, as it gives information on carrier density and band gap, and is calculated in the VASP code as the integral of the occupation number with respect to the infinitesimal energy $d\epsilon$:

$$N(\epsilon_i) = \int_{-\infty}^{\epsilon_i} n(\epsilon) d\epsilon \tag{20}$$

In Chapter 4, an analysis of the work functions of several pristine and hydrogenated model carbide slabs is shown. The reported work functions ($\Phi$) were obtained from the following equation:

$$\Phi = E_{vacuum} - E_{Fermi} \tag{21}$$

where $E_{Fermi}$ is the maximum electronic energy in the system and $E_{vacuum}$ is the average of the local (i.e. electrostatic) potential of the volume of the unit cell above

the surface. The resulting Φ can be linked to the theoretical half-cell electrode potential for the slabs, for each coverage state, according to the methodology outlined by Trasatti[117]:

$$E_{vs.\ NHE} = \frac{\Phi_{slab}}{e} - 4.5\ V \tag{22}$$

where $\Phi_{slab}$ is the work function of the slab, $e$ is the electron charge and 4.5 V is an estimate of the absolute potential of the NHE as calculated from its work function, coherently with that found in the literature.[118,119]

*Ab initio thermodynamics*

The effect of hydrogen coverage has been further investigated by means of the *ab initio* thermodynamics formalism[120,121] with the objective of elucidating the level of hydrogenation as a function of the chemical potential of $H_2$ in the gas phase. The surface free energies (σ) of each slab model are defined as follows:

$$\sigma(T,p,\theta) = \gamma + \frac{E_\theta - E_{clean}}{A} - \frac{n}{A}\mu_H(T,p) \tag{23}$$

Where γ is the surface energy of the relaxed, pristine slab, $E_\theta$ is the energy of the slab with coverage state θ, $E_{clean}$ is the energy for the pristine slab, $n$ is the number of H atoms adsorbed on the surface and $\mu_H$ is their chemical potential in the gas phase. Values for the chemical potential as a function of temperature and pressure were calculated as shown by Santos-Carballal *et al.*[121] using standard statistical thermodynamics, via the formula:

$$\mu(T,p) = \frac{1}{2}\left(E_{el} + ZPE + \Delta G_{H_2}(T,p^0) + k_b T \cdot ln\frac{p}{p^0}\right) \tag{24}$$

where $E_{el}$ and $ZPE$ are respectively the electronic and zero-point energy of the hydrogen molecule as derived from DFT, and $\Delta G_{H_2}$ is the difference in Gibbs free energy between 0 K and T at constant pressure $p^0 = 1\ bar$ as calculated from the partition function of the molecule; the last term is the pressure dependency of the Gibbs free energy.

## 2.6 Computational Resources

Calculations were performed on CPU resources provided by Cardiff University (Raven), Supercomputing Wales (Hawk), Materials Chemistry Consortium (Archer), and Barcelona Supercomputing Centre (MareNostrum IV). The computational details of each computing cluster are summarised in Table 2.1.

| *Cluster name* | *CPU architecture* | *Cores/node* | *Core frequency* | *# of nodes* |
|---|---|---|---|---|
| *Raven* | Intel Sandy Bridge | 16 | 2.60 GHz | 128 |
| *Hawk* | Intel Skylake | 40 | 2.40 GHz | 201 |
| *Archer* | Intel Ivy Bridge | 24 | 2.70 GHz | 4544 |
| *MareNostrumIV* | Intel Skylake | 48 | 3.00 GHz | 3456 |

**Table 2.1** *Summary of the computational resources available on each of the supercomputing clusters used for this project.*

Given the ample difference between clusters, the amount of computational time used for a single calculation varied greatly. Standard optimization calculations have usually been performed using two nodes on Raven and Hawk, on which the size of the machine strongly limits the possibility of performing highly parallel calculations; conversely, the same type of calculation could be performed using four to eight nodes on Archer and MareNostrum IV, the higher capacity of which allows for faster calculations. Computational times therefore varied from less than 24 hours for calculations on MareNostrum IV to 6/7 days for the more intense calculations performed on Raven, such as those investigating the stacking arrangements of oxygen-doped carbon nitride. Standard single point calculations required significantly shorter computational times, usually well below 24 hours on all machines; even shorter computational times were needed for the investigation of partial charge density on oxygen-doped carbon nitride, since the calculations required for this purpose are only a few minutes long. More advanced calculations such as frequency and dimer method calculations have only been performed on Hawk, requiring two to four nodes and 24 to 72 hours for completion. Finally, NEB and *c*NEB calculations require a significantly higher computational effort, as they have been usually performed using one or two nodes per image and 5 to 12 images depending on the distance, in terms of reaction coordinate, between reactants and products. These calculations usually require 6 to 15 days of computational time to converge.

# Chapter 3:

# Photocatalysis on oxygen-doped carbon nitride

In this chapter we explored the structure and the electronic properties of oxygen-doped graphitic carbon nitride following the input from experimental collaborators from University College London (UCL). We will first report the experimental background on which this work is based, highlighting the performances of oxygen-doped carbon nitride upon hydrogen evolution from water and the optical and electronic properties we wish to match computationally. Secondly, we will compare our computational models for the material with previous models developed for similar photocatalysts and for pristine graphitic carbon nitride. Finally, we will analyse the optic and electronic properties of our model systems, verifying whether they match experimental evidence and proposing a rationale for the photocatalytic activity reported by our experimental collaborators.

The work presented in this chapter has previously been peer-reviewed and published as a joint experimental and computational paper in Wang *et al.* "Bandgap engineering of organic semiconductors for highly efficient photocatalytic water splitting", *Advanced Energy Materials,* 8 (24), 1801084, 2018.

## 3.1 Experimental evidence

As outlined in chapter 1, band gap tuning is a well established strategy to improve the solar-to-chemical efficiency of a material,[17,61,122] as it allows the researcher to balance the two contrasting requirements of solar spectrum harvesting, which is improved as the band gap is reduced, and chemical activity, which is more strongly driven by wide band gaps. Organic and polymeric materials often offer the flexibility to achieve such fine tuning, so wide ranging research has focused on them.[122] These materials, however, rarely show the required stability. A polymeric material that offers both robustness and photoactivity is graphitic carbon nitride, which was first shown to catalyse $H_2$ from water under visible light in 2008.[55] Band gap tuning has been applied to graphitic carbon nitride by an experimental group in University College London (UCL) through the addition of variable amounts of formic acid in the precursor, which

allowed for the substitution of some amino functional groups in the polymer with oxygen or hydroxyl groups.[123] This technique is designed to avoid the drawbacks of more traditional doping procedures previously implemented with g-$C_3N_4$ such as elemental doping and introduction of carbon quantum dots, which often led to reduced crystallinity and low apparent quantum yield due to charge recombination on defect centres.[51,53,56] The structure of the material synthetized by our experimental collaborators in UCL and its specific structure-performance relationship are the focus of this chapter.

Previous work from the same UCL group reported how modifying the synthesis of graphic carbon nitride by introducing a ketone group in its DCDA (dicyandiamide) precursor leads to a material in which some of the amino groups of the polymer's heptazine units are substituted with oxygen.[35] This new structure, which has been given the name of oxygen- and nitrogen-linked heptazine (ONLH), exhibits a band gap of 1.55 eV and improved charge separation over pristine carbon nitride; however, the procedure used does not allow for band gap tuning, as the ratio between nitrogen and oxygen is fixed in the polymer precursor. For this reason, a new polymerization procedure was developed:[123] the DCDA precursor to g-$C_3N_4$ was treated with formic acid to form aminohydroxytriazine, which is subsequently polymerized with unreacted DCDA to obtain a polymer in which the oxygen content can be regulated by the ratio between DCDA and formic acid (FA). The material as been named, after the procedure used, as formic acid treated polymeric carbon nitride (FAT-PCN, or FAT for simplicity). The different samples prepared were identified according to the FA/DCDA ratio: FAT-0 corresponds to pristine g-$C_3N_4$, while the labels FAT-0.1, FAT-0.2, FAT-0.5, FAT-0.8, FAT-1.0, FAT-1.5 and FAT-2.0 are used for the oxygen-containing samples.

The polymers were then characterized and tested for $H_2$ evolution from water under visible light irradiation. Characterization of these materials was performed in terms of elemental analysis, morphology and band position. The low FA samples (FAT-0 to FAT-0.5) presented differences <0.01% in the elemental composition, highlighting how minimal amounts of oxygen were embedded in the framework; from FAT-0 to FAT-0.5 a steady albeit slow increase in the surface area from 5.5 to 6.9 $m^2/g$ is observed, as well as a similar decrease in the band gap from 2.74 eV to 2.66 eV, as

calculated from Tauc's plot. These changes are correlated with an increase in the absorption coefficient of the band around 500nm in the visible spectrum and to a slight decrease of the conduction band minimum (CBM) of the samples. Collectively, these changes are attributed to a slight distortion of the framework, which results in an increased absorption coefficient for the n-π* excitation. Higher FA content samples, from FAT-0.8 to FAT-2.0, show more marked differences: oxygen content and surface area increase significantly in these samples, reaching respectively 2.71% and 40 $m^2/g$ in the latter; band gaps are significantly smaller than in the other samples, all within 0.15 eV of each other and reaching a minimum for FAT-1.0 at 1.92 eV before increasing again slightly in FAT-1.5 and FAT-2.0 up to 2.05 eV. Photocatalytic performances were tested by loading each sample with a 3w.t.% Pt co-catalyst and measuring the $H_2$ evolution over time in presence of 10% TEOA (triethanolamine) hole scavenger in solution and under visible light irradiation. The photocatalytic performances roughly follow the trend of the band gap, with high-FA samples showing considerably higher $H_2$ evolution than low-FA samples, and FAT-1.0 achieving the highest $H_2$ evolution rate at 0.8mmol/gh with 8.6% quantum yield at 400nm. In order to clarify the relationship between the performances reported above and the structural and electronic properties of the material, models of the electronic structure of the polymers were needed; their design and the results obtained analysing them are the focus of this chapter, while the experimental data used as reference for computational modelling is summarised in Table 3.1.

| *Sample name* | *O content / %* | *Surface area / $m^2g^{-1}$* | *Band gap / eV* | *HER activity / $\mu mol\, g^{-1}\, h^{-1}$* |
|---|---|---|---|---|
| *FAT 0* | 0.76 | 5.5 | 2.74 | 44 |
| *FAT 0.1* | 0.76 | 5.6 | 2.72 | 103 |
| *FAT 0.2* | 0.76 | 6.7 | 2.69 | 114 |
| *FAT 0.5* | 0.77 | 6.9 | 2.66 | 192 |
| *FAT 0.8* | 0.98 | 9.9 | 2.06 | 456 |
| *FAT 1.0* | 1.62 | 12.1 | 1.92 | 772 |
| *FAT 1.5* | 2.67 | 16.4 | 2.01 | 656 |
| *FAT 2.0* | 2.71 | 40.0 | 2.05 | 556 |

**Table 3.1** *Summary of the chemical and optical properties of the FAT samples, reproduced from ref(123).*

## 3.2 Modelling oxygen-doped graphitic carbon nitride

*Previous models*

Due to the absence of accurate experiments aimed at determining the periodic structure of DCDA-derived oxygen-doped carbon nitride, the starting point for this computational study has been the pristine graphitic Carbon Nitride (g-$C_3N_4$) structure. This material is synthesised from DCDA, which is condensed into heptazine planar units and therefore polymerised by linking these through their -NH- active sites. While the resulting polymer does not present a unique crystal structure, exhibiting a combination of 2D planes and linear chains as a result of the presence of three linking groups on each heptazine unit, Fina *et al.*[54] have demonstrated that the material is primarily composed of linear chains organised in planes stacked in an A-B-A fashion which optimises π overlap, as shown by structure [1] of Figure 3.1. Previous literature from Wang *et al.*[35] on ONLH showed how the structure proposed in ref(55) for g-$C_3N_4$ could be used as a starting point for the computational modelling of oxygen-doped carbon nitride. In the computational section of that paper, the most stable oxygen doping was found to be the substitution of -NH- groups of the pristine carbon nitride polymer with -O-. As a result of this substitution, the calculations predicted a significant change in the symmetry of the unit cell caused by a distortion of the framework, which is no longer planar and creates a twisted structure with A-B-A stacking. Dr. N. Martsinovic (University of Sheffiled), who undertook the computational work reported in ref(55), provided us with this ONLH structure – shown as structure [2-a] of Figure 3.1 – which has been analysed in this work both as-received and after further modifications within our theoretical framework, and compared to a variety of structures developed specifically for the present project. This procedure was considered necessary because the computational work reported in ref(35) had been performed using a different technique – atom-centred basis set and B3LYP functional with dispersion correction, run periodically using the CRYSTAL09 code – which is often regarded as "higher on the Jacob ladder" of chemical accuracy, potentially invalidating some of the partially contrasting results which will be presented here; nevertheless, the models designed specifically for this work – shown in section [3-a] to [3-i] of Figure 3.1 – are in similar and in certain cases better agreement with experimental data, effectively validating our procedure and allowing

a greater range of structures to be studied due to its lower computational cost. This has been exploited by deriving several additional models from the experimental g-$C_3N_4$ structure from ref(54), specifically built to investigate the structure-property relationship arising in FAT polymers from the short-range ordering of oxygen doping.

*Original structures*

Nine additional geometries have been built in order to investigate the FAT polymers, using the following procedure. A model of the g-$C_3N_4$ bulk structure was obtained from Fina *et al*.[54], containing four linear chains of two heptazine monomers each. The eight heptazine units, as shown in Figure 3.1 [1], are organized in two planes parallel to each other, about 3.2 Å apart and arranged with an A-B-A stacking that balances the interaction between the aromatic planes and the H-bonds between the chains. This structure contains eight -$NH_2$ 'terminal' functional groups bonding the chains together by hydrogen bonds and eight -NH- 'linker' functional groups connecting two consecutive heptazine units in the same polymeric chain. Nine new structures, shown in Figure 3.1 [3-a] to [3-i], have been designed for the present work. In each of the nine new structures four amino groups were modified to either -OH terminal groups or -O- linker groups. Specifically, five structures have been modified with the latter and four with the former, in order to represent a wide range of potential polymer conformations and study the differences in their electronic properties. These structures provide an oxygen content of 2.86%, close to that of FAT-2.0. This choice was made for a few reasons. Firstly, this provides a direct comparison between our own structures and the non-planar ones taken from earlier work. Secondly, this approach followed input from our colleagues carrying out experimental work, as they were interested in investigating such oxygen loadings; finally, it allowed us to investigate a wide variety of configurations, highlighting how the short-range order influences the photocatalytic performances of the material. Each structure analysed in this work is shown in Figure 3.1.

[1]

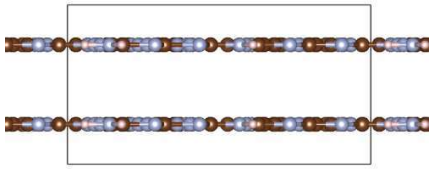

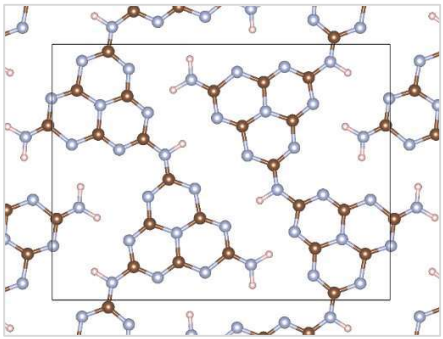

[2-a]

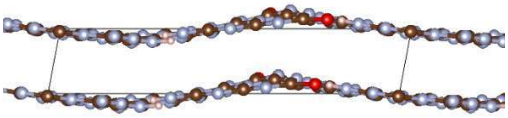

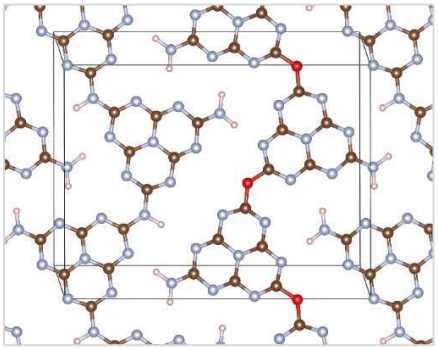

[2-b]

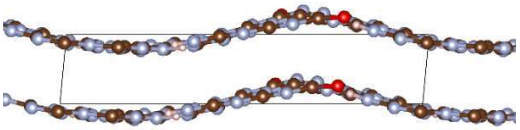

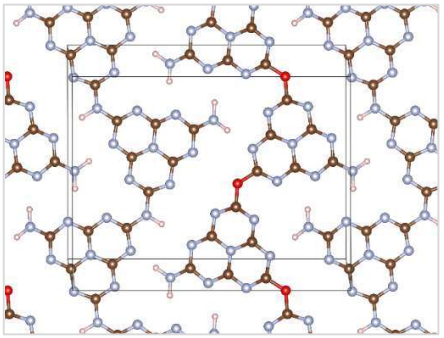

**Figure 3.1** part 1. *All structures investigated within this study are reported. The colour scheme is at follows: H = pink, C = brown, N = blue, O = red. The unit cell is outlined in grey. Structure [1] is the geometry for g-$C_3N_4$ reported in ref(54), structures [2-a] to [2-f], the ONLH models, are related to the previous study of oxygen-doped carbon nitride reported in ref(35). Structures [3-a] to [3-i], the FAT models, have been developed specifically for this study.*
*For structures [1], [2-a] and [2-b], reported in this page, a side view of the whole unit cell (left, along the a-axis) and a top view of a single atomic layer (right, along the c*-axis) are shown. Of interest here are: the geometry of the unit cell, which goes from orthorhombic in [1] to monoclinic in [2-a] and [2-b]; the structure of the polymer (left), which goes from planar in [1] to twisted in [2-a], and has even higher torsional angle in its fully optimized geometry [2-b]; the identical oxygen distribution in [2-a] and [2-b] (right), which gives rise to adjacent N-only and O-only chains.*

[2-c]

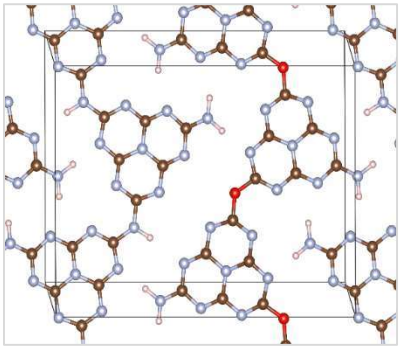

[2-d]

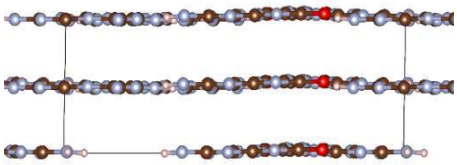

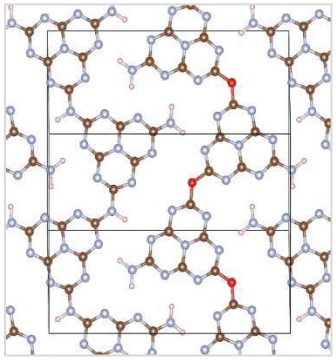

[2-e]

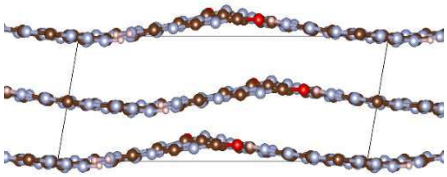

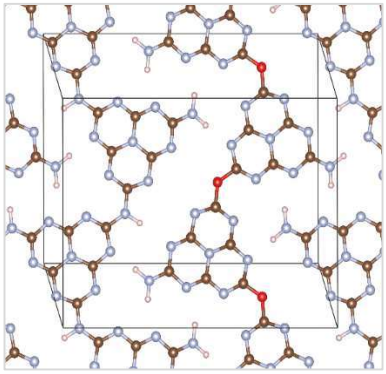

**Figure 3.1** part 2. *All structures investigated within this study are reported. The colour scheme is at follows: H = pink, C = brown, N = blue, O = red. The unit cell is outlined in grey. Structure [1] is the geometry for g-$C_3N_4$ reported in ref(54), structures [2-a] to [2-f], the ONLH models, are related to the previous study of oxygen-doped carbon nitride reported in ref(35). Structures [3-a] to [3-i], the FAT models, have been developed specifically for this study.*
*For structures [2-c], [2-d] and [2-e], reported in this page, a side view of the whole unit cell (left, along the a-axis) and a top view of a single atomic layer (right, along the c*-axis) are shown. Of interest here are: the geometry of the unit cell, which is monoclinic in all structures displayed here; the structure of the polymer (left), which goes from twisted in [2-c] to almost planar after full optimization in [2-d]; the identical oxygen distribution in all structures (right), which gives rise to adjacent N-only and O-only chains.*

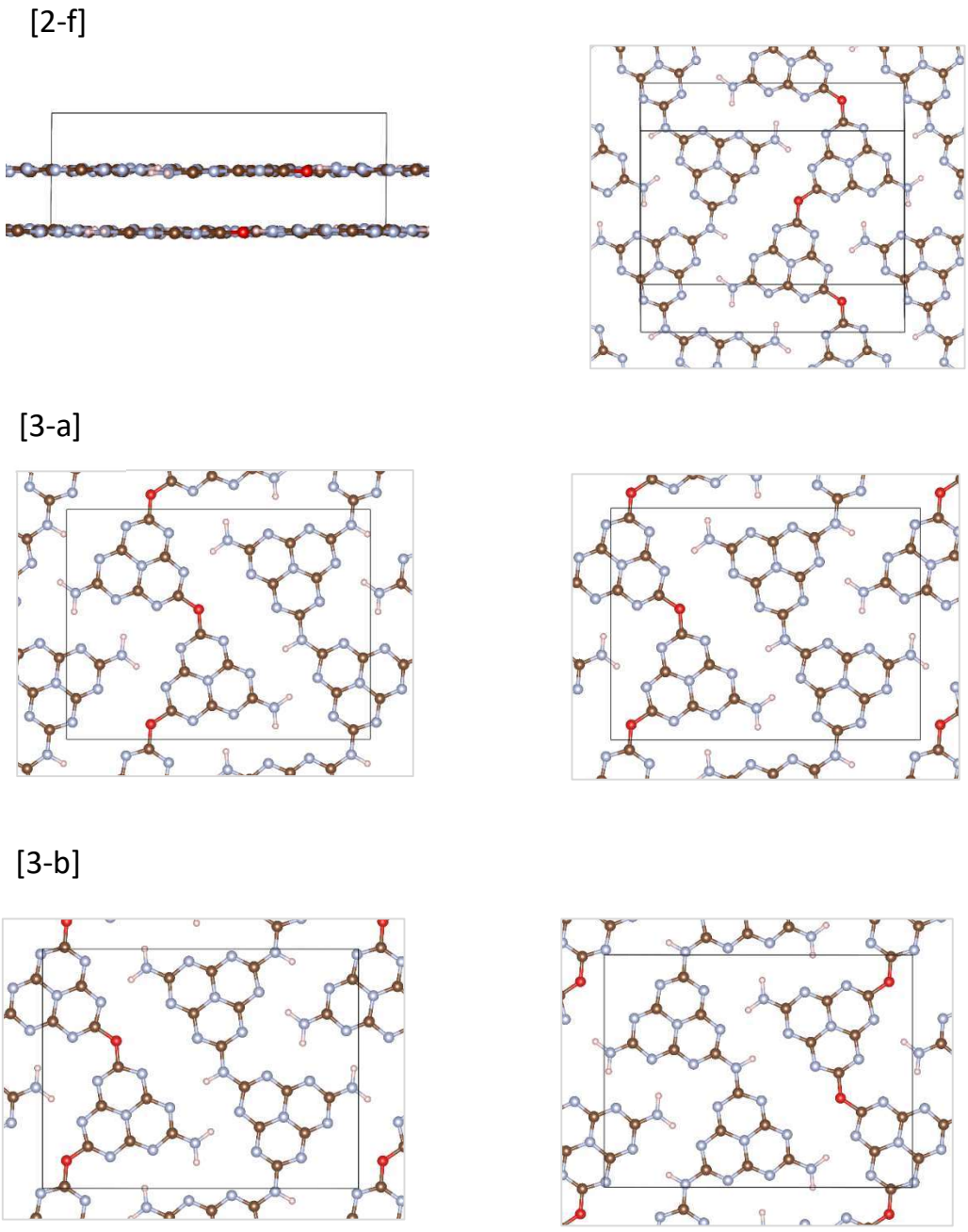


**Figure 3.1** part 3. *All structures investigated within this study are reported. The colour scheme is at follows: H = pink, C = brown, N = blue, O = red. The unit cell is outlined in grey. Structure [1] is the geometry for g-$C_3N_4$ reported in ref(54), structures [2-a] to [2-f], the ONLH models, are related to the previous study of oxygen-doped carbon nitride reported in ref(35). Structures [3-a] to [3-i], the FAT models, have been developed specifically for this study.*
*For structure [2-f], a side view of the whole unit cell (left, along the a-axis) and a top view of a single atomic layer (right, along the c*-axis) are shown. For structures [3-a] and [3-b], the top view (along the c*-axis) of the bottom (left) and top (right) layers is shown. The side view is discarded for FAT structures since their geometry is always planar. Of interest here are: the structure of the polymer in [2-f] (left), which goes from twisted in [2-e] (its non-optimised analogous, in the previous page) to almost planar; oxygen distribution in [3-a] and [3-b], which differ for the position of their top layer (right), but both give rise to adjacent N-only and O-only chains.*

[3-c]

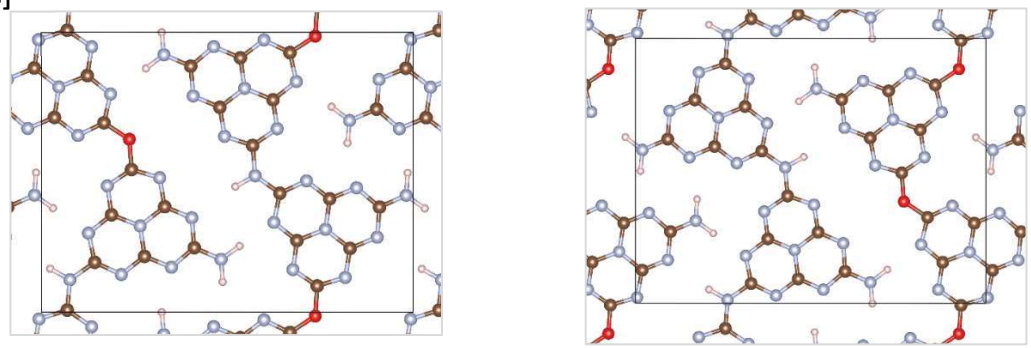

[3-d]

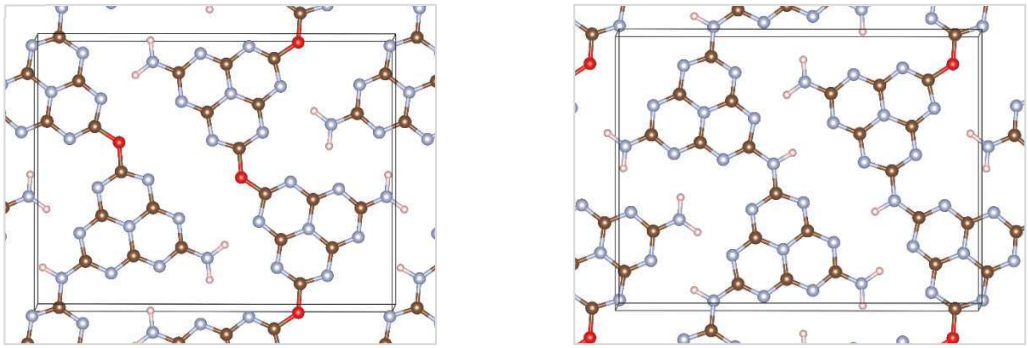

[3-e]

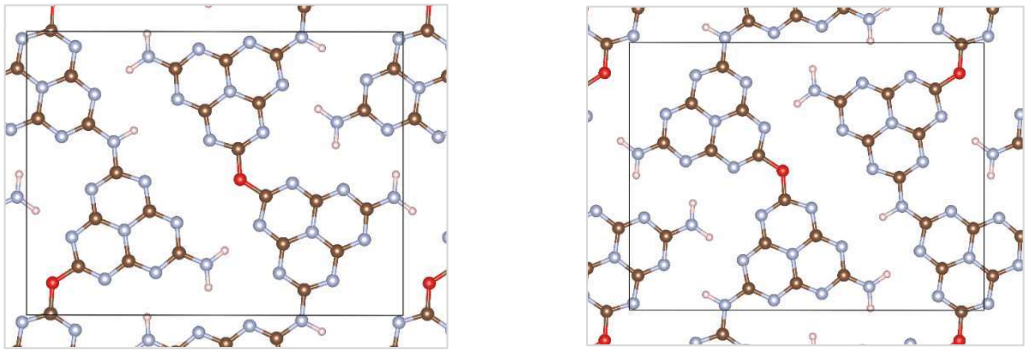

**Figure 3.1** part 4. *All structures investigated within this study are reported. The colour scheme is at follows: H = pink, C = brown, N = blue, O = red. The unit cell is outlined in grey. Structure [1] is the geometry for g-$C_3N_4$ reported in ref(54), structures [2-a] to [2-f], the ONLH models, are related to the previous study of oxygen-doped carbon nitride reported in ref(35). Structures [3-a] to [3-i], the FAT models, have been developed specifically for this study.*
*For structure [3-c] to [3-e], displayed in this page, the top view (along the c*-axis) of the bottom (left) and top (right) layers is shown. The side view is discarded for FAT structures since their geometry is always planar. Of interest here is the oxygen distribution in [3-c], [3-d] and [3-e]: in [3-c], the top layer (right) is divided in N-only and O-only chains as the models in previous pages, while the bottom layer (left) has one oxygen substituent per chain, resulting in 75% of O-doped chains; [3-d] also has 75% of O-doped chains, but does not show adjacent N-only and O-only chains since the bottom layer (left) has a higher oxygen content than the top layer (right); [3-e] has all chains doped with a single oxygen linker.*

[3-f]

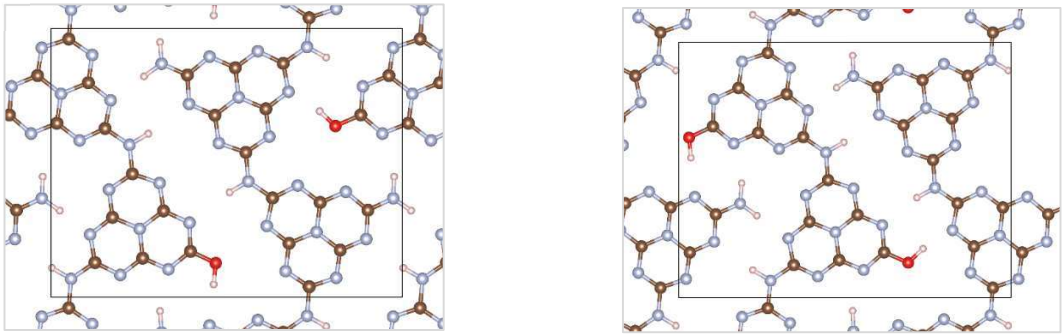

[3-g]

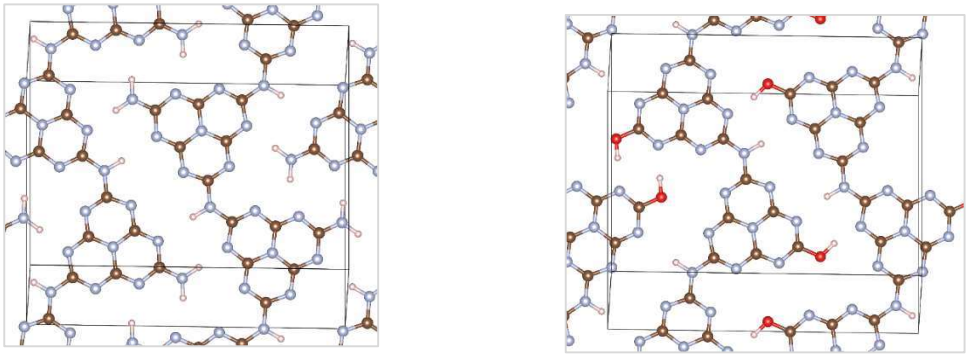

[3-h]

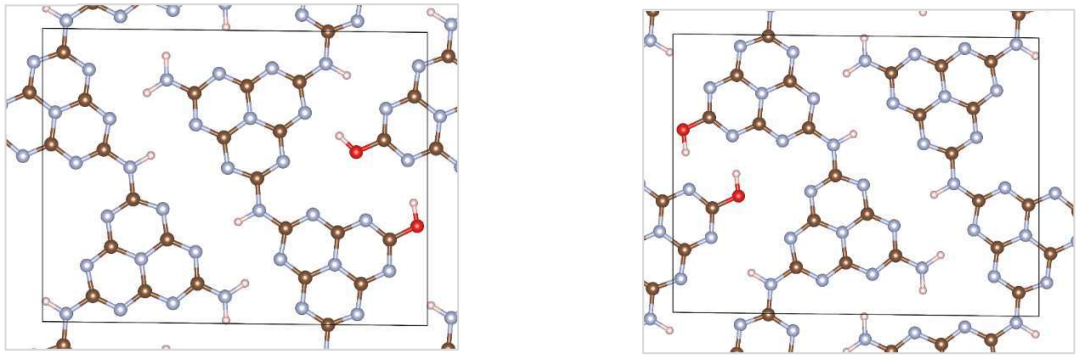

**Figure 3.1** part 5. *All structures investigated within this study are reported. The colour scheme is at follows: H = pink, C = brown, N = blue, O = red. The unit cell is outlined in grey. Structure [1] is the geometry for g-$C_3N_4$ reported in ref(54), structures [2-a] to [2-f], the ONLH models, are related to the previous study of oxygen-doped carbon nitride reported in ref(35). Structures [3-a] to [3-i], the FAT models, have been developed specifically for this study.*
*For structure [3-f] to [3-h], displayed in this page, the top view (along the c*-axis) of the bottom (left) and top (right) layers is shown. The side view is discarded for FAT structures since their geometry is always planar. Of interest here is the oxygen distribution, in the form of -OH terminal groups, in [3-f], [3-g] and [3-h]: in [3-f] oxygen doping is in 50% of chains in both layers, giving rise to adjacent O-only and N-only chains; in [3-g] oxygen doping is concentrated in the top layer (right) of the unit cell, while the bottom layer (left) appears similar to pristine carbon nitride; in [3-g] all chains in the unit cell have a single -$NH_2$ group substituted with an -OH group.*

[3-i]

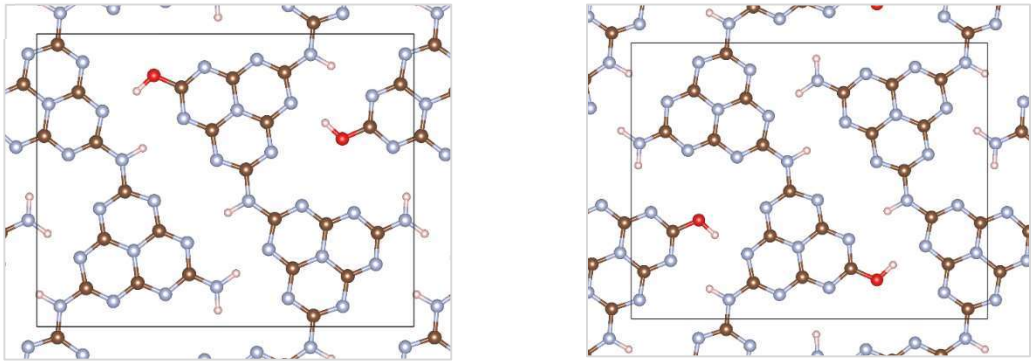

**Figure 3.1** part 6. *All structures investigated within this study are reported. The colour scheme is at follows: H = pink, C = brown, N = blue, O = red. The unit cell is outlined in grey. Structure [1] is the geometry for g-$C_3N_4$ reported in ref(54), structures [2-a] to [2-f], the ONLH models, are related to the previous study of oxygen-doped carbon nitride reported in ref(35). Structures [3-a] to [3-i], the FAT models, have been developed specifically for this study.*
*For structure [3-i], displayed in this page, the top view (along the c*-axis) of the bottom (left) and top (right) layers is shown. The side view is discarded for FAT structures since their geometry is always planar. Of interest here is the oxygen distribution, in the form of -OH terminal groups: in [3-i] all chains in the unit cell have a single -$NH_2$ group substituted with an -OH group.*

Structure [1] is the bulk model of g-$C_3N_4$ as taken from ref(54). This structure presents the material as composed of polymeric heptazine chains arranged in planar atomic planes kept together by hydrogen bonds between the -$NH_2$ terminal groups of each heptazine unit and the aromatic nitrogen atoms of their neighbours. The orthorhombic unit cell encloses four polymeric chains in two atomic layers, each chain made of two heptazine units.

The structures in section [2] are derived from previous computational work on ONLH. Structure [2-a] is the ONLH structure as taken directly from ref(35); this structure is a modification the g-$C_3N_4$ model above obtained by replacing -NH- linker groups with oxygen in half the polymeric chains of the unit cell considered. Structure [2-b] is the same structure after a full geometry optimization has been performed. Structures [2-c] is a 1x1x2 supercell of structure [2-a], created in order to check the effect of cell size on the geometric, energetic and electronic properties of the material; structure [2-d] is the resulting fully optimized geometry. Structures [2-e] and [2-f] are respectively the fixed and optimized geometries obtained from [2-c] by performing a 90° rotation around the c-axis of one layer with respect to the other. All structures display a non-planar geometry within a monoclinic unit cell, even though the torsional angle between the heptazine units which gives rise to the twisted geometry varies significantly, as

shown by the side view of Figure 3.1 [2-a] to [2-f] and by Table 3.2. Most notably, the oxygen content is identically distributed in all ONLH structures: on each atomic layer, one of the two polymeric chains displays only oxygen linker groups, while the other only has -NH linker groups.

| *Structure number* | *Oxygen type* | *O-containing chains* | *Formation energy / kJmol$^{-1}$* | *Average torsional angle* | *Interlayer distance / Å* | *Source* |
|---|---|---|---|---|---|---|
| *[1]- g-$C_3N_4$* | None | 0% | +13.05 | 0.00° | 3.25 | Ref (77) |
| *[2] - ONLH* | | | | | | |
| *[2-a]* | -O- | 50% | -7.56 | 13.75° | 3.57 | Ref (28) |
| *[2-b]* | -O- | 50% | -7.76 | 19.31° | 3.61 | Modified [2-a] geometry |
| *[2-c]* | -O- | 50% | non optimized geometry | | | |
| *[2-d]* | -O- | 50% | -8.34 | 3.62° | 4.44 | |
| *[2-e]* | -O- | 50% | non optimized geometry | | | |
| *[2-f]* | -O- | 50% | -8.58 | 2.36° | 3.37 | |
| *[3] - FAT* | | | | | | |
| *[3-a]* | -O- | 50% | -8.91 | 0.00° | 3.22 | Structural modification of [1] |
| *[3-b]* | -O- | 50% | -9.14 | 0.00° | 3.20 | |
| *[3-c]* | -O- | 75% | -9.09 | 0.00° | 3.21 | |
| *[3-d]* | -O- | 75% | -9.06 | 0.00° | 3.23 | |
| *[3-e]* | -O- | 100% | -9.12 | 0.00° | 3.21 | |
| *[3-f]* | -OH | 50% | -10.04 | 0.00° | 3.25 | |
| *[3-g]* | -OH | 50% | -10.50 | 0.00° | 3.56 | |
| *[3-h]* | -OH | 100% | -10.40 | 0.00° | 3.21 | |
| *[3-i]* | -OH | 100% | -10.18 | 0.00° | 3.25 | |

**Table 3.2** *Summary of the structural and geometric properties of all investigated models*

The structures in section [3] are the planar models derived for this project on FAT polymers and have all been only investigated after full optimization. All FAT model structures have the same planar geometry of g-$C_3N_4$ and mostly differ for their oxygen distribution: as highlighted in Table 3.2, FAT structures [3-a] to [3-e] have been modified with -O- linkers replacing -NH- linkers, while [3-f] to [3-i] have -OH terminal group in place of -$NH_2$ groups. The different oxygen arrangements result in a variable distribution of the oxygen content, which is localised on 50%, 75% or 100% of the polymeric chains within the unit cell, a characteristic that will later be linked with photocatalytic performances.

Structures [3-a] and [3-b] present an ordered oxygen arrangement: in both cases, each of the two layers present one chain with only O-linker groups and one chain with only N-linker groups; the main difference between the two structures is the relative position

of the two layers, as in [3-a] the O-linked chains are stacking on top of each other, while in [3-b] they do not. Structures [3-c] and [3-d] both present O-linkers in 75% of the polymeric chains, being composed of one purely O-linked chain, two partially O-linked chains and a single N-linked chain; the main difference between the two structures is in the oxygen distribution between the layers, as [3-d] displays O-linkers localised in one of the atomic layers (left in Figure 3.1 [3-d], displaying 3 O-linkers and 1 N-linker), while [3-c] does not. Structure [3-e] has one O-linker and one N-linker on each polymeric chain in the unit cell, resulting in a uniform distribution.

Structures [3-f] to [3-i] have been designed by exchanging -$NH_2$ groups at the non-polymerized end of each heptazine unit with -OH groups. Both structure [3-f] and structure [3-g] have oxygen on 50% of the polymeric chains, presenting two purely OH-terminated and two purely N-terminated chains. [3-f] has the OH-terminal groups equally distributed on each layer, while [3-g] has all OH-terminal groups on a single atomic layer. Structure [3-h] and structure [3-i] have -OH groups on 100% of polymeric chains, although in different relative positions: in structure [3-h] the proximity of the -OH groups of adjacent chains allows for a strong double hydrogen bond, while in [3-i] this is not possible.

*Oxygen-doped graphitic carbon nitride*

Formation energies, defined in Chapter 2 as the difference between the energy of each model system and that of its elemental constituents, have been used to compare the 16 structures, and reported in Table 3.2. According to our calculations, in all cases the formation of oxygen-doped carbon nitride is favoured over the polymerization of the non-doped material, as the formation energy strongly decreases when oxygen is in the polymer. Formation energies for the planar structures are more negative than those for twisted structures with comparable oxygen arrangements (for example, [3-a] has a formation energy 1.15 KJ/mol lower than [2-b], its optimized non-planar equivalent); furthermore, while the relaxation of [2-a] to [2-b] leads to an increase in average torsional angle between the heptazine units – corresponding to a less planar structure – the relaxation of the structures [2-c] and [2-e] to [2-d] and [2-f] respectively leads to structures with close-to-zero average torsional angles and energies still higher than all the structures in section [3]. Meaningful energy differences are also found amongst FAT structures. Models in which -OH terminal groups are present show formation

energies about 1 KJ/mol lower than models with -O- linker groups, due to the stronger hydrogen bonds the former functional groups can form between adjacent polymeric chains. The energy differences between different configurations of O-linker and OH-terminal structures, however, are sufficiently small that both oxygen types should be found, as confirmed experimentally.[35]

The data shown above suggest that a planar geometry is more favourable for oxygen doped carbon nitride compared to a twisted structure. This, however, is in disagreement with the previous computational work on ONLH reported in ref(35), in which the non-planar geometry is argued to be energetically favoured over the planar one. This discrepancy between the present work and previous investigations probably arises from the different technique used: while this work has been carried on with plane-wave basis sets and a GGA functional, ref(35) states the work had been carried on with atom-centred basis sets and using an hybrid functional to approximate the exchange and correlation energy. As mentioned above, the results presented here are not disproven by the existence of such partially contradicting data: this work will show how the planarity of the polymeric chain has little effect on the performances of the material, which can conversely be put more readily in relation with other geometric characteristics of the models. This conclusion is further strengthened by comparison of the intra-layer distance of all model systems with experimental literature: XRD experiments highlight a 3.30 Å distance for oxygen-doped samples, in better agreement with our planar geometries (ranging from 3.20 Å to 3.56 Å) than with the non-planar structure [2-a] which shows a distance of 3.57 Å as calculated in ref(35).

## 3.3 Electronic properties of FAT models

The FAT model structures shown in section [3] of Figure 3.1 have been used to investigate the effect of variable oxygen distribution within the unit cell on the electronic properties of the material. The consequences of oxygen distribution could then be related to the varying optic and photocatalytic performances displayed by experiments on the FAT samples. The results of this investigation are presented here.

*Band gap prediction*

As noted in the first section of this chapter, FAT samples with high oxygen loading show substantial differences from those synthetized using smaller amounts of formic acid. The Density of States (DOS) calculations on [3-*x*] models highlight how these structures are appropriate models for high oxygen loading FAT polymers, as expected from their oxygen content. All the computational structures [3-*x*] have band gaps between 1.77 and 2.33 eV; while this is a considerable range for structures that only differ in the short-range ordering, it matches experimental band gaps for high-performance FAT polymers, which are evaluated to be between 1.98 and 2.06 eV through Tauc's plots. The use of multiple oxygen configurations as models for the FAT polymers supports the investigation of the properties arising from changing the material's short-range ordering. Four of the O-linked structures match the experimental band gap of about 2.1 eV displayed by FAT-2.0, while the fifth, [3-e], shows a much higher value of 2.33 eV. Conversely, three of the four OH-terminated structures show band gaps larger than that, ranging between 2.24 and 2.30 eV, while configuration [3-f] presents the shortest band gap of all investigated configurations at 1.77 eV. No clear reason for this variability could be proved, as the only structural differences between the investigated geometries lie in the quality and quantity of their H-bonds, which cannot be readily put in relation with such a significant change in the band structure of the material. Nonetheless, a correlation could be drawn between the band gap and the distribution of oxygen among the polymeric chains in each structure: when the oxygen is distributed in only 50% of the polymeric chains, resulting in a unit cell organized in adjacent N-only and O-only chains, the band gap is generally below 2.1 eV. Opposite to this, all unordered structures show band gaps above 2.1 eV. The only exception to that is given by structure [3-g]: in its unit cell, the oxygen doping is concentrated on a single atomic plane, giving rise to a structure with no N-only chain adjacent to an O-only one on the same layer even if all oxygen is concentrated in only 50% of the polymeric chains, and this structure exhibits a band gap of 2.3 eV. We can therefore suggest that the electronic structure is somehow indeed affected by the presence of adjacent N-only and O-only chains on a single atomic plane.

| *Structure number* | *Oxygen type* | *O-containing chains* | *N – O chain sequence* | *Band gap / eV* | *Charge separation* |
|---|---|---|---|---|---|
| *[3-a]* | -O- linker | 50% | Yes | 2.13 | Yes |
| *[3-b]* | -O- linker | 50% | Yes | 2.11 | Yes |
| *[3-c]* | -O- linker | 75% | One layer only | 2.14 | Partial |
| *[3-d]* | -O- linker | 75% | No | 2.13 | Partial |
| *[3-e]* | -O- linker | 100% | No | 2.33 | No |
| *[3-f]* | -OH terminal | 50% | Yes | 1.77 | Yes |
| *[3-g]* | -OH terminal | 50% | Between layers | 2.30 | No |
| *[3-h]* | -OH terminal | 100% | No | 2.24 | No |
| *[3-i]* | -OH terminal | 100% | No | 2.27 | No |

**Table 3.3** *Summary of the structural, optical and electronic properties of FAT models.*

The band gap trend, however, is not consistent with experiments when the variation in oxygen content is considered: experimentally, the band gap is reduced as the oxygen content is increased from FAT-0 to FAT-1.0 and only slightly increases again from FAT-1.0 to FAT-2.0, which is in opposition to our calculations both in terms of band structure and in terms of comparison with pristine carbon nitride. For the former, the presence of oxygen in the valence band edge and conduction band edge is not prominent, suggesting that the presence of doping should not significantly change either. For the latter, the DOS calculations on g-$C_3N_4$ show a band gap of only 1.01 eV, not only significantly underestimating the experimental band gap of ~2.7 eV, but also reversing its trend over oxygen doping, as this seems to expand the band gap of the material rather than reducing it.

The inaccurate determination of the band structure is a well-known limitation of GGA functionals such as that implemented in this work, but as the use of more accurate techniques such as hybrid-DFT functionals and TD-DFT was considered to be too computationally expensive for unit cells of this size. Since experimental evidence clearly disproves the accuracy of band gaps calculated for carbon nitrides, no further investigation of the band structure was performed and the results shown in this section were only considered qualitatively.

### *Photocatalytic performances*

Despite the unreliable accuracy of band gap calculations performed using GGA techniques, the disposition of oxygen within the unit cell of each FAT model could be related to the photocatalytic properties of the material through the exploration of the partial charge density of valence and conduction band edges. According to the

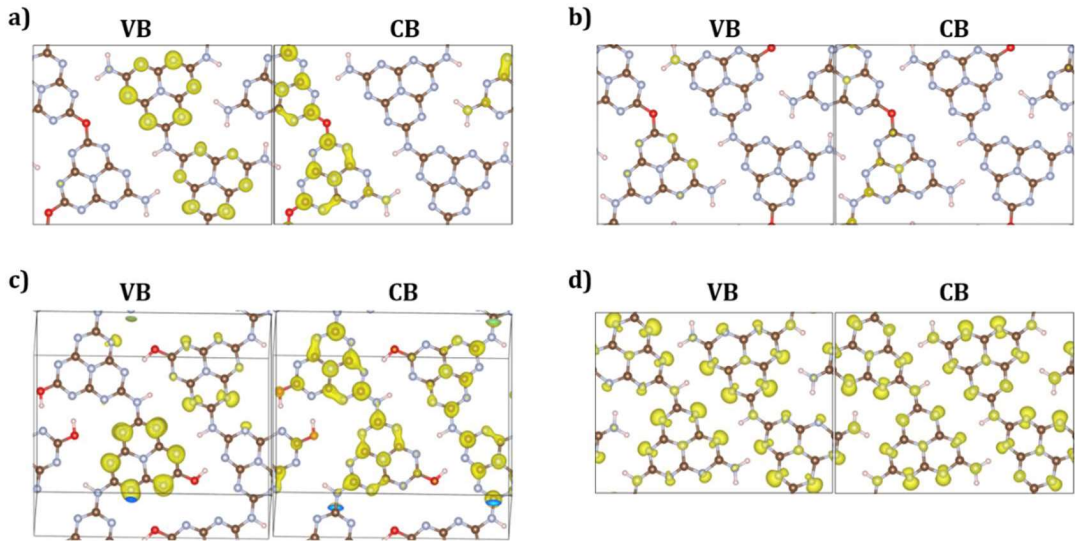


**Figure 3.2** *The valence band edge (VBE) and conduction band edge (CBE) of three FAT models and of pristine g-$C_3N_4$. The colour scheme is at follows: H = pink, C = brown, N = blue, O = red, the orbitals isosurface is depicted in yellow. The figure depicts the VBE and CBE of: (a) bottom layer of structure [3-a], exemplifying the correlation between a highly ordered structure with adjacent O-only and N-only chains and the full spatial separation of the two band edges. (b) Bottom layer of structure [3-c], showing partial overlap between VBE and CBE; the top layer, the structure of which is displayed in Figure 3.1 [3-c] (right), exhibits spatial separation of CBE and VBE. (c) Top layer of structure [3-g], which has all oxygen doping on this layer, displaying no spatial separation of VBE and CBE. (d) structure [1] – g-$C_3N_4$, in which all chains are equivalent by symmetry, preventing any difference between their electronic properties.*

experimental data provided in Table 3.1, the performances of FAT samples increase with oxygen content up to FAT-1.0 due to the gradual substitution of -NH- groups with oxygen in the polymer, before degrading slowly towards FAT-2.0. It was possible to correlate this activity trend to the interaction between of N-only chains and O-only chains in the FAT polymers: similarly to what is observed through the DOS calculations, which highlighted how adjacent N-only and O-only chains on the same atomic plane might reduce the band gap of the material compared to that of less ordered structures, the same characteristic is related to a peculiar spatial separation between VBE and CBE.

By analysing the charge density of the valence and conduction band edges of each configuration, some examples of which are reported in Figure 3.2, four possible situation arise: a) when each atomic plane shows one N-only and one O-only chain, these will host the VBE and CBE respectively, and no overlap is found not they are linked by chemical bonding; b) when 75% of the chains are O-containing but some of those are still adjacent to N-only chains, partial overlap between VBE and CBE is

found and the tendency to have the former on N-only and the latter in O-containing chains is maintained; c) if no N-only chain is adjacent to an O-containing chain, either because all chains are O-containing or because all oxygen is located in a single atomic layer, little to no spatial separation is observed, and the pattern with which VB and CB are localized can be irregular; d) if no oxygen is present – i.e. for pristine carbon nitride – the system is more symmetric and therefore VB and CB are not localized preferentially in any given section of the material.

The reason for such spatial separation might be ascribed to a change in the electrostatic potential of the O-containing chains due to the presence of polar covalent bonds, as suggested in previous studies,[124,125] but our modelling could not find solid evidence for this argument due to the complexity of the problem and the polymeric nature of the system. Nevertheless, this finding is in good agreement with the experiments, since it relates the peak in performance of FAT-1.0 to an optimization of the charge separation arising from the local ordering of the system: as oxygen content is increased from FAT-0 to FAT-1.0, adjacent N-only and O-only chains become more probable; the resulting short-range ordering of the material allows photoexcited electrons and holes to gather on O-only and N-only chains respectively, which act as traps and slow down charge recombination, improving the photocatalytic performances of the material. Conversely, if oxygen loading is further increased an excessive concentration of O-containing chains increases the overlap between VB and CB, as local ordering of the material becomes less likely, resulting in the reduction of photocatalytic performances observed on FAT-1.5 and FAT-2.0, which occurs even as the band gap is only marginally affected by the increase in oxygen loading.

*Conclusions*

It is reasonable to propose that the photocatalytic performances of FAT samples depend on the local distribution of oxygen as much as on its concentration within the g-$C_3N_4$ framework: while a reasonable amount of formic acid will benefit the performances of the polymer by reducing the band gap and, in some areas of the polymer, create a spatial separation between the VB and the CB that improves the $e^-$-$h^+$ lifetime, a concentration of O-linkers that is too high would lower the probability of having this separation, leading to the decreased performances highlighted in FAT-1.5 and FAT-2.0. Therefore, a peak in performance is to be expected, as a fine control

over the arrangement of oxygen within the framework is impossible and a more uniform distribution of oxygen among the chains does not significantly improve the charge separation with respect to pristine g-$C_3N_4$. Similar conclusions are found in ref(35) with a non-planar structure for the ONLH polymer, which is reported to have a similar structure-property relationship. This allows us to further expand our understanding of the performances of the material. Wang *et al.*[35,123] reported the increase in performance at low FA loading as due to a distortion of the framework, while the much more significant activity found for higher FA loadings had to be related to electronic properties. Our results, which highlight a similar charge separation properties in the planar and non-planar models, allows us to conclude that this is correct: the distortion of the polymer influences only marginally the localization of VB and CB, and instead it is the distribution of oxygen in the framework that enhances charge separation in the photocatalytic material, resulting in its remarkable ability to evolve molecular hydrogen from water using natural light. It is finally possible to note how the band gap, often regarded as a key descriptor of how promising a material can be for photochemistry and photoelectrochemistry, is indeed only one of the many factors that influence a process as complex as photocatalytic water splitting; when, as in this case, the band gap of the material can be tuned with relative ease, it becomes clear how the fine detail of the chemistry of the system has a great impact on the performances of the photocatalyst: while an excessive amount of oxygen has only a marginal effect on the band gap of the material we studied, it has a major impact on its capacity to increase $e^-$-$h^+$ pair lifetime and ultimately on its catalytic activity.

# Chapter 4:
# Hydrogen adsorption on transition metal carbides

## 4.1 Bulk and surface properties of TMCs

As discussed in Chapter 1, transition metal carbides are cheap and robust catalytic materials that have been used for hydrogen evolution and $CO_2$ reduction. The bulk and surface properties of TMCs have been extensively studied both computationally and experimentally, allowing us to choose four of the most promising early transition metal carbides for our investigation of the hydrogen evolution reaction on these materials and to use well-reported models with confidence in their accuracy in describing those systems. Previous reports[126–129] have studied the bulk properties and surface reactivity of several late transition metal carbides with various metal-to-carbon ratios. In these studies, both hydrogen adsorption and $CO_2$ reduction are reported on the (001) surface of these materials; $CO_2$ has been shown to be activated by the adsorption on $Mo_xC$ surfaces, highlighting a strong and barrierless hydrogen adsorption on these surfaces as well as a mechanism of $CO_2$ reduction strongly dependent on the stoichiometry of the investigated surface.[76,127,130] Quesne et al.[85] have instead reported a thorough computational study of all transition metal carbides with 1:1 metal to carbon ratio and rock-salt structure, highlighting the stability of their bulk structures and extending the investigation of the surface properties to the (001), (011) and (111) facets of each carbide. Calculation of the heat of formation of all carbides highlighted how TiC, VC, ZrC and NbC have the most stable bulk structure, a result consistent with experimental literature,[72] which has confirmed the stability of these four carbides with this specific structure and stoichiometry. The (001) facet has been shown to be the most stable low-index surface by an analysis of surface free energies, while the (011) surface is generally the one with the lowest work function and the *d*-band centre position is less negative on carbon-terminated (111) surfaces, all quantities that have previously been linked to surface reactivity and that we wish to correlate with adsorption energy in this chapter.

We therefore decided to investigate the four most stable carbides with rock-salt structure upon the surface reactivity of their four most stable facets, so that the results

could be compared both with previous computational investigations of the reactivity of other carbides and with the highlighted bulk and surface properties of the same materials. In this chapter, the hydrogenation of the (001), (011) and (111) surfaces of TiC, VC, ZrC and NbC has been investigated through an analysis of the adsorption energies of $H_2$ at increasing coverage states, with the aim of obtaining useful information on the activity of such catalysts over the HER.

The models used in this chapter are the same reported in ref(85), which use rock-salt structure for the bulk and replicate it to obtain a 2x2x3 supercell, which is then cut along the (001), (011) and (111) planes, the latter presenting two surface terminations. After a preliminary study of the kinetics of hydrogen adsorption on selected surfaces, the hydrogenation of all surfaces has been investigated thoroughly, analysing the geometry of the adsorption sites and correlating energetic trends with the electronic properties of the pristine surfaces. Finally, multiple coverage states of each surface have been studied, analysing the results in terms of *ab-initio* thermodynamics and proposing a distinctively superior performance over HER for the (001) surfaces of all investigated carbides.

The work presented in this chapter has previously been peer-reviewed and published in the paper "Hydrogen adsorption on transition metal carbides: a DFT study" by Silveri *et al.,* in *Phys. Chem. Chem. Phys.* 2019, 21, 5335-5343.

## 4.2 Hydrogen Adsorption

*Kinetic barriers to hydrogen adsorption*

The mechanism of hydrogenation was explored on the (001) and (011) surfaces of TiC. Using the DFT methodology, structures and settings discussed in Chapter 2, molecular hydrogen was placed 3.5 Å above its (001) surface and the structure was allowed to relax obtaining a long-range interaction energy of $E_{phys}$ = -0.013 eV, as shown in Figure 4.1. The distance between the surface and the molecule was then progressively reduced by fixing the Z-coordinate of one hydrogen, in order to obtain a first approximation of the activation path to surface hydrogenation. As the distance is reduced the energy increases slightly, reaching a maximum about 2.6 Å above the surface ($E_{phys}$ = +0.01 eV, central data point for (001) in Figure 4.1) with the hydrogen

molecule positioned with the H–H axis roughly perpendicular to the surface. A further contraction of the distance between molecule and surface leads to a sharp decrease in energy followed by heterolytic dissociation of the H-H bond, as one hydrogen atom is coordinated by a Ti surface atom while the other adsorbs on a surface C atom. A final full relaxation of the hydrogenated slab brings the system to its adsorbed minimum energy state, in which each hydrogen atom is coordinated to a surface carbon atom, completing its dissociative adsorption on the surface. The lack of a significant energy barrier to hydrogen adsorption is confirmed by the systematic investigation of the potential energy surface using a NEB method, through which no transition state could be isolated.

TiC (011) presents a similar case, also shown in Figure 4.1. A maximum in energy of $E_{phys}$ = 0.01 eV is found when $H_2$ is constrained 4.5 Å above the surface by fixing the

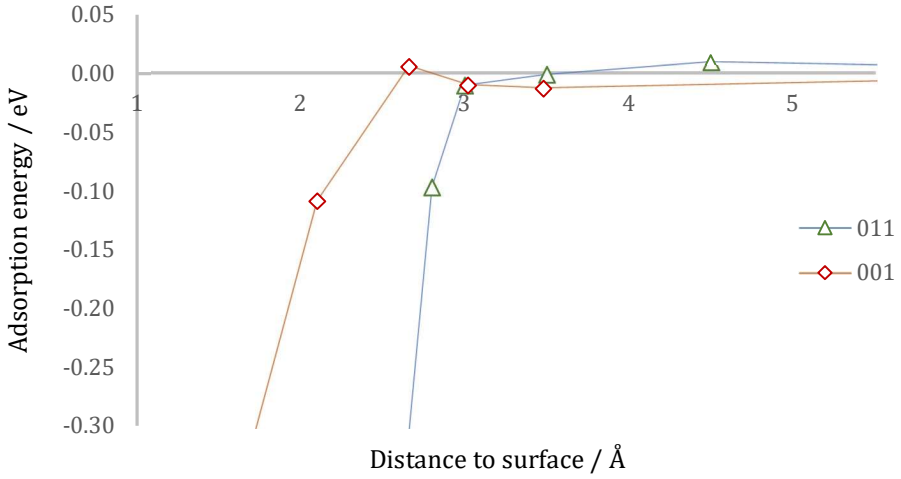


**Figure 4.1.** *Energetic profile of hydrogen adsorption on TiC(001) (orange) and TiC(011) (blue). In both cases the energetic barrier is very small, although differences between the two adsorptions can be found: TiC(001) highlights the presence of a shallow minimum which can be correlated with a physically adsorbed state, while this is completely absent in the profile of adsorption on TiC(011), which goes towards significantly negative energies at higher distances. In both cases the highest energy found is of the order $10^{-2}$ eV higher than the sum of energies of the reactants and no transition state could be isolated. The final points of both adsorptions have been removed for clarity: on the right, the non-interacting states correspond to an interaction energy equal to zero; on the left we find the adsorbed states of $H_2$ on each surface, for which energy and C-H distance can be found in Table 4.1.*

Z-coordinate of one of its two hydrogen atoms; as the distance is reduced further, the total energy of the system decreases slowly, until the molecule splits and adsorbs on the surface as it is placed less than 3 Å above the surface. Once again, NEB calculations were performed but no transition state could be isolated, leading to the

conclusion that the – rather limited – energy increase mentioned above is a consequence of the constraints forced on the systems rather than of the presence of an energy barrier to the dissociative adsorption of hydrogen on this surface. This result is consistent with literature data[64,88,131] and therefore a further, lengthy exploration of the PES resulting from the adsorption of $H_2$ over the (111) surfaces of TiC and over VC, ZrC and NbC was deemed unnecessary.

*Hydrogen adsorption on TiC surfaces*

Hydrogen adsorption has been first investigated on TiC in order to identify the energetic and geometric characteristics of all configurations and reduce the number of systems in study. For the first surface studied, TiC(001), three hydrogen adsorption sites have been identified: on top of a Ti atom, between two Ti atoms and on top of a C atom. The adsorption sites are named $M_{on\ top}$, $M_2$ and $C_{on\ top}$ respectively. The first two sites, which coordinate surface metal atoms, are both endothermic, displaying

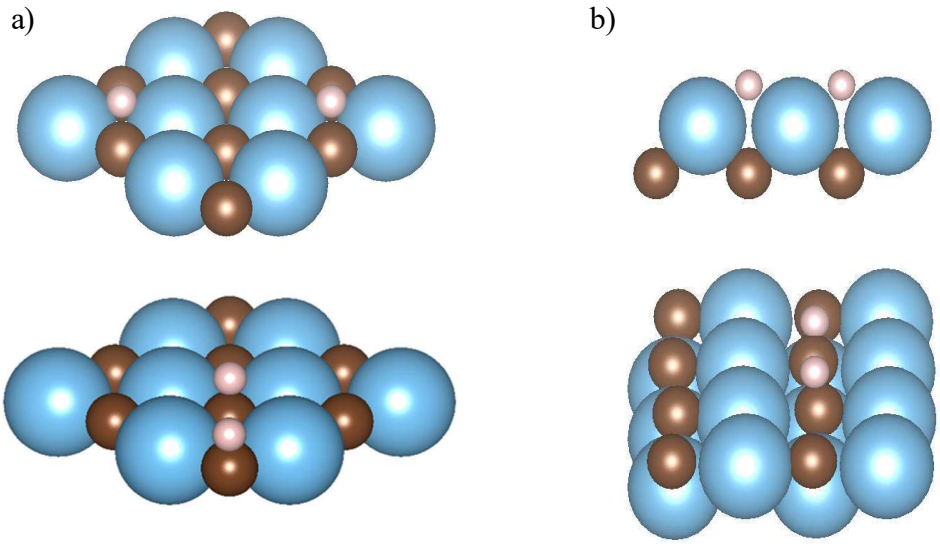


**Figure 4.2** *(a) Adsorption geometries for the TiC (001) surface: the $M_2$ site (top) and the $C_{on\ top}$ site (bottom). (b) Adsorption geometries for the TiC (011) surface: the $M_2$ site (top) and the $C_{on\ top}$ site (bottom). The colour scheme is as follows: Ti = blue, C = brown, H = pink*

$E_{ads}$ = +1.52 eV and $E_{ads}$ = +0.33 eV respectively. The $C_{on\ top}$ site, however, is exothermic, exhibiting an adsorption energy of $E_{ads}$ = -0.62 eV. In all three cases the surface reconstruction upon adsorption is minimal, if at all present. The two lowest-energy sites are shown in Figure 4.2 (a). The difference in adsorption energies between sites is mirrored in the Ti – H and C – H bond lengths: much longer in the former cases ($M_{on\ top}$ 1.79 Å, $M_2$ 1.66 Å) compared to the latter ($C_{on\ top}$ 1.13 Å). A

Bader charge analysis performed on the hydrogenated systems shows how the adsorbed hydrogens retain one electron each, even though the $M_2$ site has the hydrogen atoms lying in the plane of the surface (0.03 Å above the plane of Ti atoms) instead of in an upper atomic plane as in the *on top* sites. Similarly, a comparison of the surfaces' Densities of States (DOS) highlights that, although differences between the pristine and hydrogenated surfaces are present, these do no alter significantly the electronic structure of the slab. Figure 4.4 shows this comparison for the section of the DOS closer to the Fermi energy for the pristine and hydrogenated TiC(001) surface.

| *(001) surface* | *Preferred site* | *$E_{ads}$ / eV* | *C-H distance / Å* | *Average $e^-$ / a.u.* |
|---|---|---|---|---|
| *TiC* | $C_{on\ top}$ | -0.623 | 1.128 | 0.936 |
| *VC* | $C_{on\ top}$ | -0.165 | 1.139 | 0.971 |
| *ZrC* | $C_{on\ top}$ | -0.740 | 1.336 | 1.007 |
| *NbC* | $C_{on\ top}$ | +0.055 | 1.124 | 0.972 |

**Table 4.1** *The geometric and energetic effects of adsorption on all investigated (001) surfaces. For each carbide, only the most favourable adsorption site is shown. The column "Average $e^-$" reports the result of the Bader charge analysis on the adsorbed hydrogens on each surface, averaged between the two atoms.*

On TiC(011), similar $M_2$ and $C_{on\ top}$ adsorption sites are found, although no $M_{on\ top}$ site could be found. On this surface, both sites are exothermic, with significantly negative adsorption energies: $E_{ads}$ = -0.74 eV on $M_2$ and $E_{ads}$ = -1.30 eV on $C_{on\ top}$. The more negative adsorption energy compared to TiC(001) adsorption sites are mirrored in shorter bond distances for both $C_{on\ top}$ and $M_2$ sites. As for TiC(001), surface reconstruction upon adsorption is minimal on both sites, as are the electronic changes

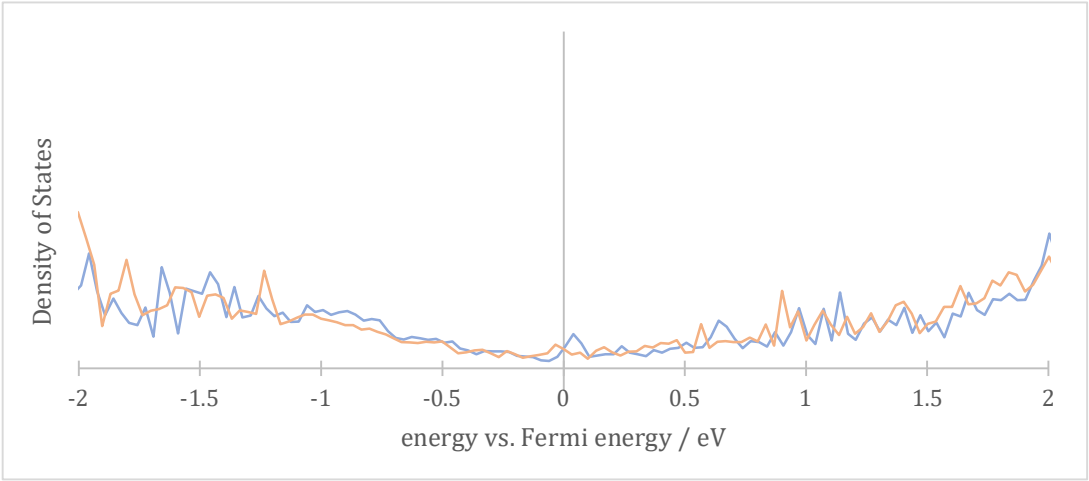


**Figure 4.3** *Comparison of the region of the Density of States (DOS) around the Fermi energy for the TiC(001) surface before (in blue) and and after (in orange) adsorption of an hydrogen molecule.*

investigated through DOS calculations and Bader charge analyses of the pristine and hydrogenated slabs.

The two surface terminations along the (111) plane are treated separately because the stoichiometries of their topmost atomic layer and their stabilities are different. Both the metal and carbon terminated slab models show a dipole perpendicular to the surface arising from the presence of alternate layers of carbon and metal atoms.[132] Despite this, previous studies have shown similar trends in the electronic properties of the surface on both reconstructed and unreconstructed surfaces[85]. Moreover, experimental reports only show unreconstructed metal-terminated surfaces for the (111) plane, when it can be shown to be clean and free of impurities under vacuum.[133–136] For these reasons, only the unreconstructed metal and carbon terminations of the (111) plane will be considered in this study, and will be referred to as (111)-M and (111)-C respectively.

| *(011) surface* | *Preferred site* | $E_{ads}$ / *eV* | *C-H distance / Å* | *Average e⁻ / a.u.* |
|---|---|---|---|---|
| *TiC* | $C_{on\ top}$ | -1.399 | 1.115 | 1.031 |
| *VC* | $C_{on\ top}$ | -1.070 | 1.112 | 0.930 |
| *ZrC* | $C_{on\ top}$ | -1.355 | 1.061 | 1.119 |
| *NbC* | $C_{on\ top}$ | -0.884 | 1.114 | 0.891 |

**Table 4.2** *The geometric and energetic effects of adsorption on all investigated (011) surfaces. For each carbide, only the most favourable adsorption site is shown. The column "Average e⁻" reports the result of the Bader charge analysis on the adsorbed hydrogens on each surface, averaged between the two atoms.*

On the metal terminated (111) surface, metal atoms are disposed in a hexagonal fashion as shown in Figure 4.3. A threefold site is available for the hydrogen atom, which adsorbs at the barycentre of a triangle formed by metal atoms, with no movement in the surface; this adsorption structure is labelled as $M_3$ site. There are, however, small differences among the $M_3$ sites: examining the ABA configuration of metal atoms in the TiC unit cell it can easily be seen how carbon atoms are in fact occupying half the octahedral sites left by the metallic framework. For this reason, a hydrogen positioned in a $M_3$ site can be situated either on top of a carbon atom of the second atomic layer or on top of a metal atom of the third atomic layer – i.e. one of the octahedral sites left free by carbon atoms. However, the energy difference is minimal, as on TiC(111)-M both configurations involve a highly exothermic

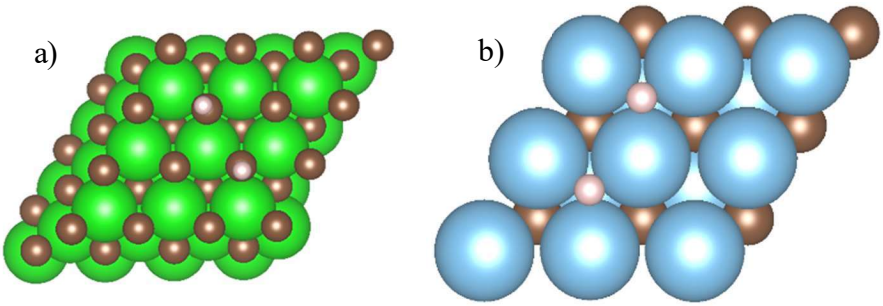


**Figure 4.3** *Adsorption geometries for (a) the ZrC(111)-C surface, with hydrogen on the $C_{on\ top}$ site; (b) the TiC(111)-M surface, with hydrogen on the $M_3$ site. The colour scheme is as follows: Ti = blue, C = brown, H = pink*

adsorption with $E_{ads}$ = -1.99 eV. The analysis of the Bader charges in this case shows how each hydrogen has gained a charge equivalent to 0.66 electrons, explanation for which could come from either geometric or electronic factors: the position of the hydrogen is very close to the surface, 0.94 Å above the plane of Ti atoms, which could result in the area in close vicinity of the hydrogen atoms being filled by the electrons of the surface; on the other hand, the electronic factor takes into account the electronegativity of the metal, which is lower than that of the hydrogen, exacerbating the electron-poor nature of the topmost metallic layer of the slab. Either way, the DOS calculations highlight once again a strong similarity between the electronic structure of the pristine surface and that of the hydrogenated slab.

A different picture resulted from the calculations on the TiC(111)-C surface. On this slab, the presence of hydrogen leads to a complete reconfiguration of the surface, with carbon atoms of the topmost layer reacting with each other and the adsorbing hydrogen molecule, ultimately demonstrating a severe instability of this termination in the presence of hydrogen. However, this instability is not observed on ZrC and NbC, so the preliminary investigation of the hydrogen adsorption was carried out on the former of these. On ZrC(111)-C, only one adsorption site was found, labelled $C_{on\ top}$ and showing $E_{ads}$ = -2.02 eV, reflecting the uniform adsorption pattern found on TiC(111)-M. The adsorption site is similar to the $C_{on\ top}$ sites found on (001) and (011) surfaces, with hydrogen sitting directly on top of a surface carbon atom with no significant surface reconstruction nor change in the DOS of the slab upon hydrogenation.

| *(111)-M surface* | *Preferred site* | $E_{ads}$ / *eV* | *C-H distance / Å* | *Average e⁻ / a.u.* |
|---|---|---|---|---|
| *TiC* | $M_3$ | -1.992 | 2.020 | 1.637 |
| *VC* | $M_3$ | -1.166 | 1.935 | 1.555 |
| *ZrC* | $M_3$ | -1.342 | 2.169 | 1.678 |
| *NbC* | $M_3$ | -1.244 | 2.074 | 1.592 |

| *(111)-C surface* | *Preferred site* | $E_{ads}$ / *eV* | *C-H distance / Å* | *Average e⁻ / a.u.* |
|---|---|---|---|---|
| *TiC* | - | - | - | - |
| *VC* | - | - | - | - |
| *ZrC* | $C_{on\ top}$ | -2.014 | 1.099 | 0.875 |
| *NbC* | $C_{on\ top}$ | -1.691 | 1.101 | 0.828 |

**Table 4.3** *The geometric and energetic effects of adsorption on all investigated (111)-M and (111)-C surfaces. For each carbide, only the most favourable adsorption site is shown. The column "Average e⁻" reports the result of the Bader charge analysis on the adsorbed hydrogens on each surface, averaged between the two atoms.*

*Identifying trends and descriptors for hydrogenation of TiC, VC, ZrC and NbC surfaces*

Throughout all four TiC surfaces investigated, a clear pattern arises: adsorption sites on top of a carbon atom always show significantly more negative adsorption energies than all other sites on the same surfaces when they are available; however, metal sites become more and more exothermic as the number of surface atoms that coordinate the adsorbing hydrogen is increased from one ($M_{on\ top}$ site on TiC(001), significantly endothermic) to three ($M_3$ site on TiC(111), more exothermic than $C_{on\ top}$ on TiC(011). As the investigation of hydrogen adsorption was extended to the surfaces of VC, ZrC and NbC, only the most favourable adsorption sites for each surface have been considered.

In all cases, the results in terms of bond distances and surface reconstruction are very similar for each carbide. However, the energetics of the reaction can vary significantly. On the 3 remaining (001) surfaces, only ZrC(001) presents a strongly exothermic adsorption ($E_{ads}$ = -0.73 eV) on the $C_{on\ top}$ site, while VC(001) and NbC(001) show adsorption energies that are close to zero, slightly exothermic for the former and slightly endothermic for the latter, a unique case throughout our study. Charge analyses and DOS calculation show similar results to those obtained on TiC(001), so it was possible to conclude that on all (001) surfaces the adsorption of hydrogen has only marginal effects on the electronic properties of the material. Similarly, (011) surfaces exhibit analogous behaviour on all carbides; the adsorption energy is again the most significant difference between carbides, as ZrC and NbC display the most and least negative adsorption energies respectively and no major surface

reconstruction is observed upon adsorption. The adsorption on (111)-M surfaces is, as expected, very exothermic and again results in no major surface reconstruction. However, on this facet TiC shows the most exothermic adsorption. As mentioned before, the (111)-C surface of TiC is unstable upon hydrogen adsorption. The same is true for VC(111)-C, but it is possible to adsorb hydrogen on the analogous surfaces of ZrC and NbC. The adsorption on NbC is geometrically similar to that on ZrC but less exothermic, as its adsorption energy is $E_{ads}$ = -1.69 eV.

With a few, minor exceptions, a clear trend in the exothermicity of hydrogen adsorption can be identified, both in terms of carbides and surfaces:

$$(111)\text{-C} > (111)\text{-M} \approx (011) >> (001)$$

$$\text{ZrC} > \text{TiC} >> \text{VC} > \text{NbC}$$

This trend can be correlated with certain properties of the pristine surfaces, as calculated by *Quesne et al.*[85], in order to identify descriptors capable of predicting the reactivity of the surface without the need of explicit calculation of adsorption energies. The surface energies (σ), work functions (Φ), and *d*-band centre positions reported in ref(85) can all be correlated to the hydrogen adsorption energies calculated in this study, giving rise to trends along the carbides and the surfaces similar to those highlighted above. The best correlation is found for the *d*-band centre position, a characteristic of each surface which can be taken as a good indicator of their reactivity. The trends over the surfaces for a single carbide and over the same face of each carbide show an inverse correlation with the $E_{ads}$ which, despite some discrepancies, can be considered a good descriptor of the activity of the carbide surface considered.

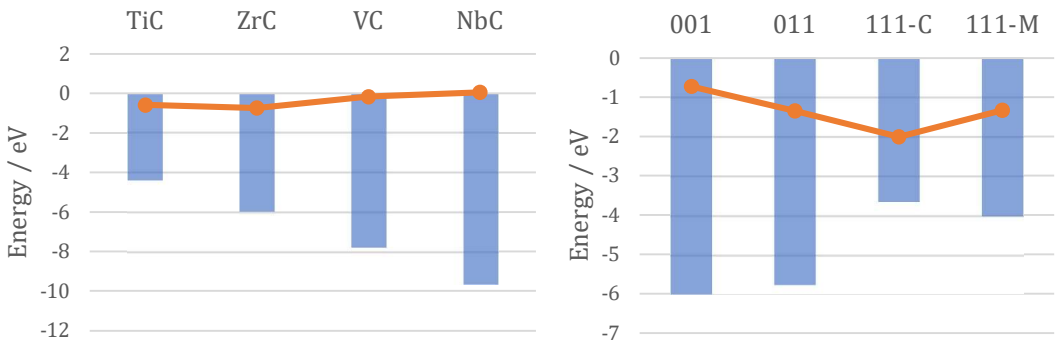


**Figure 4.5** *Correlation between $E_{ads}$ of a single hydrogen molecule on selected surfaces (orange dots) and the d-band centre positions of the same surfaces (blue columns). (left) shows the values for (001) surfaces over the four carbides, (right) shows the values for ZrC over its four surfaces.*

Figure 4.5 shows how, along the four surfaces of ZrC and through the four carbides on their (001) surfaces, a less negative *d*-band centre energy corresponds to a more exergonic hydrogen adsorption. The correlation, however, is not always linear: a close analysis of the data in Figure 4.5 shows how the change in *d*-band centre position does not necessarily correspond to a proportional change in $E_{ads}$ of $H_2$ adsorption, even though the qualitative correlation stands through all the investigated materials. It was then possible to conclude that the *d*-band centre position can be used as a useful qualitative descriptor of the activity a surface – which is correlated to the $E_{ads}$ of an hydrogen molecule through Sabatier's principle and its commonly used application to the hydrogen evolution reaction, the volcano plot – but the complex nature of the interaction between hydrogen and the material cannot, obviously, be completely described by a relationship as simple as the one highlighted here.

## 4.3 High hydrogen coverage

*Adsorption energies*

The volcano plot, as mentioned in Chapter 1, is a useful way of correlating the adsorption energy of an hydrogen atom to the activity of a material over the hydrogen evolution reaction (HER).[15,137] Nevertheless, the extensive use of this descriptor has also been met with certain criticism, in that it cannot encompass the complexity of the mechanism of the HER and it is sometimes overused.[66] In order to avoid such shortcomings, in the present work the coverage state of each surface was investigated, so that reactions conditions closer to those found in reactors could be modelled and more information on the interaction between transition metal carbides and hydrogen could be gained. The adsorption of 2, 4, 8 and 16 hydrogen atoms has been investigated on all surfaces, and the results have been analysed through an *ab initio* thermodynamics formalism, in order to deduce the coverage state of each surface at varying temperature and pressure.

Our approach considers chemisorption of H to define its coverage in terms of the monolayer (ML). In the previous section, the 16 lowest energy adsorption sites have been identified on each model slab: on the slab representing (001) and (011) surfaces these are equally divided between $C_{on\ top}$ and $M_2$, while on those representing the two terminations of the (111) surfaces either 16 $C_{on\ top}$ or 16 $M_3$ sites are present

alternatively. On the (001) surface termination, adsorption of 4 and 8 hydrogen atoms is investigated on the exposed $C_{on\ top}$ adsorption sites. On TiC(001), VC(001) and ZrC(001), on which the adsorption of the first hydrogen molecule is exothermic, the adsorption is favourable as the total energy of adsorption becomes more negative as the loading increases. However, each adsorption is less exothermic than the previous, resulting in a less negative adsorption energy per atom as more hydrogen atoms are adsorbed on the surface. This trend is linear on all three surfaces and the slope of the line becomes steeper as the adsorption becomes more exothermic for the effect of the material. On NbC(001), as mentioned before, the first adsorption is endothermic even on $C_{on\ top}$ sites, giving rise to a slightly different behaviour of the surface. The adsorption energy per atom highlights a generally more endothermic behaviour as the coverage is increased to fill the available $C_{on\ top}$ adsorption sites; however, there is a slight decrease when the second hydrogen molecule is adsorbed: $E_{ads}$ = 0.05 eV after the first hydrogen molecule adsorbed, $E_{ads}$ = 0.04 eV after the second.

| $nH_2$ | $\theta$ | *Site on (001)* | *TiC* | *VC* | *ZrC* | *NbC* |
|---|---|---|---|---|---|---|
| 1 | ¼ | $C_{on\ top}$ | -0.62 | -0.17 | -0.73 | +0.06 |
| 2 | ½ | $C_{on\ top}$ | -0.52 | -0.14 | -0.62 | +0.04 |
| 4 | 1 | $C_{on\ top}$ | -0.35 | -0.06 | -0.38 | +0.09 |
| 8 | 2 | $C_{on\ top} + M_{on\ top}$ | - | - | +0.09 | +0.31 |

| $nH_2$ | $\theta$ | *Site on (011)* | *TiC* | *VC* | *ZrC* | *NbC* |
|---|---|---|---|---|---|---|
| *1* | ⅛ | $C_{on\ top}$ | -1.40 | -1.07 | -1.36 | -0.88 |
| *2* | ¼ | $C_{on\ top}$ | -1.29 | -0.98 | -1.35 | -0.88 |
| *4* | ½ | $C_{on\ top}$ | -1.25 | -0.94 | -1.26 | -0.79 |
| *8* | 1 | $C_{on\ top} + M_2$ | -0.84 | -0.64 | -0.93 | -0.71 |

**Table 4.4** *The energetic effects of the hydrogen loading on the (001) surface (top) and (011) surface (bottom) of each investigated carbide, in eV. Θ is the fractional coverage of the slab referred to 1 ML and $nH_2$ is the corresponding number of hydrogen atoms adsorbed on our model slabs in each case.*

On all four carbides, subsequent adsorption of $H_2$ on the (001) surface is expected to be endothermic, as only $M_2$ and $M_{on\ top}$ sites are available. However, steric effects due to the small distance between hydrogens prevent the former sites from providing a stable adsorption on all surfaces. On the carbides of the 5$^{th}$ period, ZrC and NbC, hydrogen can adsorb on the more endothermic $M_{on\ top}$ sites, which results in a total energy higher than that of the non-hydrogenated surface, $E_{ads}$ = +0.09 eV on the

former and $E_{ads}$ = +0.31 eV on the latter. However, on the carbides of the 4th period those sites cannot provide a stable adsorption minimum, so no adsorption is possible once all $C_{on\ top}$ sites on the surface are filled, corresponding to 8 hydrogen atoms in our model slabs. As different loadings have been considered for the adsorbate, the question of coverage naturally arises. Since no favourable adsorption has been found on non-carbon sites, we allow the chemisorption of hydrogen on $C_{on\ top}$ adsorption sites to define the monolayer for all surfaces, which within our model slabs translates to θ=1 when 8 H atoms are adsorbed on each of the four (001) surfaces that have been investigated. This finding is consistent with what has been highlighted for similar carbides in previous work,[130] and will allow us to draw conclusions concerning their coverage state.

The trends upon hydrogen coverage increase are similar on the (011) surfaces. As the loading is increased from 2 to 8 hydrogen atoms, the $C_{on\ top}$ adsorption sites are filled. Similarly to the (001) surfaces of TiC, ZrC and VC, adsorption on (011) surfaces favours high coverage states, since the total adsorption energy becomes more negative as the loading increases, but the driving force for each adsorption decreases, because the adsorption energy *per atom* decreases. Unlike (001) surfaces, however, the modulus of $E_{ads}$ is strongly negative for all coverage states and its reduction upon hydrogen coverage increase is limited and non-linear. This could be linked to the morphology of the surface: the surface reconstruction upon cutting the (011) plane is more significant than that shown by (001) surfaces in that the position of surface carbons shift relative to their neighbouring metals and the underlying material, resulting in slight differences in the chemical surrounding of each carbon. This factor could of course be responsible for the higher variability found in the adsorption energy trends, but since the difference in adsorption energies as coverage increases are very small – the largest difference per atom being on VC(001) as the loading is increased from 2 to 4 hydrogens, $\Delta E_{(4-2)}$ = 0.1 eV – and since we will later show that the only coverage shown by these surfaces is full coverage regardless of temperature and pressure, these discrepancies have not been investigated further. Unlike the (001) surfaces, adsorption of 16 H atoms is exothermic, since the $M_2$ site is exothermic. The decrease in adsorption energy per atom is generally more significant than between $C_{on\ top}$ site, as it is to be expected given the less exothermic nature of the isolated $M_2$ site, but the total energy is significantly lower and therefore we define for each (011)

surface the monolayer as the hydrogenation state upon which all $C_{on\ top}$ and $M_2$ sites are filled. Within our model slabs this corresponds to a coverage of θ = 1 ML when 16 hydrogen atoms are adsorbed on the surface.

Higher hydrogen coverage states have also been studied on all (111)-C surfaces, highlighting an increased stability at higher coverage: the VC(111)-C surface is found to be stable when 4 hydrogen atoms are adsorbed on it and the TiC(111)-C surface is stable when all 16 $C_{on\ top}$ sites are filled. On all carbides for which multiple loadings on the (111)-C surface were studied some decrease in $E_{ads}$ with increasing coverage can be observed, although with different characteristics from that observed on lower-index surfaces. On both ZrC(111)-C and NbC(111)-C, the difference between the adsorption energy per atom upon adsorption of 2 and 4 hydrogen atoms is negligible. Upon further increased loading more significant energy differences are found on both these facets as well as on VC(111)-C, albeit still low compared to the absolute value of $E_{ads}$: on ZrC(111)-C, $\Delta E_{ads\ (16\text{-}2)}$ = 0.173 eV, which corresponds in an decrease in the modulus of $E_{ads}$ of only 0.6% per hydrogen. This characteristic, which is shared with NbC(011) and some of the (111)-M surfaces, is probably due to the distance of the adsorption sites on these surfaces, as it is more prominent on the carbides of the 5th period.

| $nH_2$ | θ | *Site on (111)-M* | *TiC* | *VC* | *ZrC* | *NbC* |
|---|---|---|---|---|---|---|
| *1* | ⅛ | $M_3$ | - | - | -2.01 | -1.69 |
| *2* | ¼ | $M_3$ | - | -1.68 | -2.01 | -1.69 |
| *4* | ½ | $M_3$ | - | -1.64 | -1.96 | -1.62 |
| *8* | 1 | $M_3$ | -1.93 | -1.55 | -1.83 | -1.45 |

| $nH_2$ | θ | *Site on (111)-C* | *TiC* | *VC* | *ZrC* | *NbC* |
|---|---|---|---|---|---|---|
| *1* | ⅛ | $C_{on\ top}$ | -1.96 | -1.17 | -1.33 | -1.24 |
| *2* | ¼ | $C_{on\ top}$ | -1.67 | -1.14 | -1.34 | -1.22 |
| *4* | ½ | $C_{on\ top}$ | -1.44 | -1.08 | -1.33 | -1.16 |
| *8* | 1 | $C_{on\ top}$ | -1.36 | -1.01 | -1.35 | -1.11 |

**Table 4.5** *The energetic effects of the hydrogen loading on the (111)-M surface (top) and (111)-C surface (bottom) of each investigated carbide, in eV. Θ is the fractional coverage of the slab referred to 1 ML and $nH_2$ is the corresponding number of hydrogen atoms adsorbed on our model slabs in each case.*

The (111)-M surfaces, as mentioned above, also present slowly decreasing $E_{ads}$ across most carbides. At all coverages, hydrogen adsorption happens on very exothermic $M_3$ adsorption sites, showing a linear trend on VC(111)-M and NbC(111)-M as the hydrogenation of the surface becomes slowly less exothermic with increasing hydrogen loadings. However, this decrease is not shown at all on ZrC(111)-M, on which $\Delta E_{ads\,(16\text{-}2)} = 0.015$ eV, and is instead much steeper but not linear on TiC(111)-M, on which $\Delta E_{ads\,(4\text{-}2)} \approx \Delta E_{ads\,(16\text{-}4)} = 0.31$ eV. While these discrepancies could not be fully explained, because no significant difference is found in the adsorption geometries and in the electronic structure of the slabs, some interesting trends across all carbides and surfaces can be highlighted.

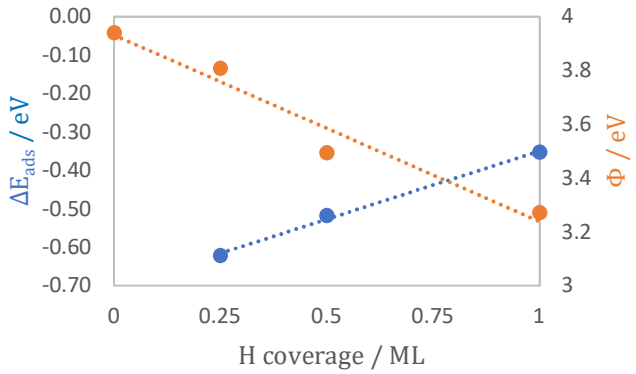


**Figure 4.6**. *The graph shows the correlation between hydrogen loading and $\Delta E_{ads}$ (blue) and between hydrogen loading and Φ (red) on the TiC (001) surface.*

Throughout the four carbides, the increase in coverage is correlated with a decrease in adsorption energy per atom, which is consistent with the results found for other carbides by previous work[130]. A possible explanation for this effect might come from the analysis of the work function Φ, which steadily increases with coverage as electrons are inserted in the conduction band, as Figure 4.6 shows for the TiC(001) surface. The trend of the adsorption energy and the work function with θ is found on all carbides and surfaces, albeit as Figure 4.6 shows it is often not linear, similarly to what has previously been highlighted for $E_{ads}$.

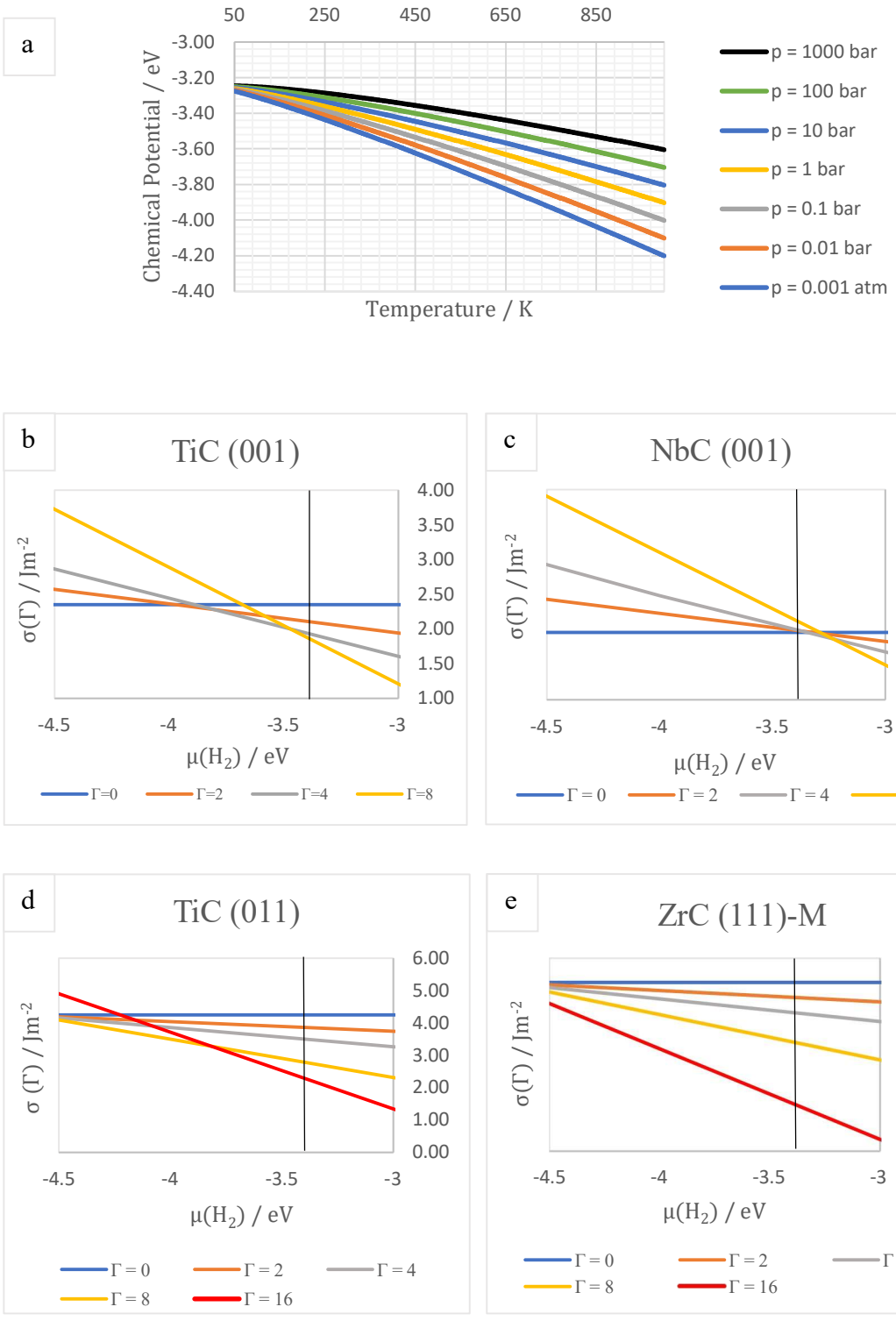


**Figure 4.7**. *(a) Chemical potential of a hydrogen molecule in gas phase as a function of temperature and pressure as calculated from first principles in the intervals $T \in$ (50 K, 1000K) and $p \in$ (0.001 bar, 1000 bar). (b-e) Surface free energies for different hydrogenation states of the surfaces of TiC(001), NbC(001), TiC(011) and ZrC (111)-M as a function of the chemical potential of a hydrogen molecule above the surface. $\Gamma$ indicates the number of hydrogen atoms adsorbed on the surface, so that $\Theta = 1$ corresponds to $\Gamma = 8$ for (001) surfaces and to $\Gamma = 16$ for (011) and (111) surfaces. The black vertical lines highlights $\mu = 3.39$ eV, the chemical potential of hydrogen at room temperature and pressure.*

*The coverage state as a function of chemical potential*

In order to elucidate the relationship between different coverage conditions on the same surface we computed the free energies of the hydrogenated surfaces as a function of the chemical potential of hydrogen, following the procedure outlined in Chapter 2. Figure 4.7 (a) reports the chemical potential (μ) in eV of a molecule of $H_2$ in the gas phase above our model slabs as a function of temperature and pressure. This allows us to predict the stability of each coverage state on all investigated surfaces as a function of the temperature and pressure of the $H_2$ gas phase. Even though this is an approximation of the thermodynamics of the system – not taking into account the free energy terms related to the surface – and unrelated to the reaction conditions of the HER – which takes place in aqueous solution, not at the interphase with an homogeneous hydrogen gas – it allows us to draw conclusions on the activity of each surface as an hydrogen evolution catalyst with a more nuanced theoretical background than the use of a simple volcano plot, without the additional computational effort required for DFT calculations of solid – liquid interphases.

Figure 4.7 (b) shows the free energies for the four stable coverages of the TiC(001) surface versus the chemical potential of the hydrogen. The graph highlights how, even though θ = 1 ML is the most exothermic coverage, lower coverages appear to be more favourable at low chemical potentials, which correspond to high temperatures and low pressures. Similar plots can be produced for VC(001) and ZrC(001), owing to the similar energetic trends for the three surfaces. In stark contrast, NbC(001) only exhibits hydrogenation of the surface at high pressures and low temperatures, quickly moving from the pristine surface to the fully hydrogenated as the chemical potential of hydrogen is reduced. This effect is obviously a consequence of the mildly endothermic nature of all adsorption sites present on this surface, which keep hydrogen from adhering to the surface at standard condition, but hasher conditions can reverse this tendency.

On all other surfaces the strongly exothermic nature of adsorption causes the highest coverage state to be the most favourable in most cases, as exemplified by the plots in Figure 4.7 (d) and (e) which report the coverage states of TiC(011) and ZrC(111)-M. Nonetheless, Figure 4.7 (d) shows a change in coverage state around $\mu_{H_2} = -3.9\ eV$, corresponding to conditions of very high temperature or very low pressure, below

which the higher slope of the θ = 1 line leads θ = ½ to become the most favoured coverage state. The difference in slope is caused by the adsorption of hydrogen on two different sites, as only $C_{on\ top}$ sites are filled up until θ = ½ while less exothermic $M_2$ sites are filled from there to θ = 1. Nevertheless, this effect is marginal, as it only happens at harsh conditions on TiC and even harsher for the three other carbides – $\Delta E_{ads\ (16\text{-}8)}$ = 0.41 eV for TiC(011) is the highest of all (011) surfaces, corresponding to the largest increase in slope between θ = ½ and θ = 1 and therefore the least negative potential at which the two lines meet – so that it is possible to consider the (011) surfaces to be effectively fully hydrogenated at most conditions. On the contrary, (111) surfaces only show a single type of adsorption site, consistently displaying high adsorption energy. As a consequence, the free energy plots for all (111)-C and (111)-M surfaces all show θ = 1 as the most favourable coverage state regardless of temperature and pressure, as shown in Figure 4.7 (e).

*Implications for hydrogen evolution catalysis*

It is possible to correlate the catalytic activity of a material towards the hydrogen evolution reaction (HER) with the free energy of adsorption of hydrogen on its surface: the former increases when the latter approaches zero, since $\Delta G_{ads} = 0$ corresponds to a balance between the adsorption and desorption of hydrogen,[67] the two primary steps of the reaction. It is therefore possible to predict the conditions at which the reaction will be most efficiently catalysed by identifying the intersections between the lines representing two subsequent coverage states. On TiC(001) this would imply having the best catalytic activity at temperatures slightly higher than 300 K, at which multiple coverage changes happen, while on NbC(001) low temperatures or high pressures are needed to catalyse the reaction efficiently. The graphs for VC(001) and ZrC(001) are similar to that of TiC(001), but due to the less exothermic $E_{ads}$ values, the equilibrium states between different coverage states for VC(001) are closer to 298 K and 1 atm. In general, it is possible to predict that (001) surfaces should offer a good catalytic activity towards the HER reaction on all investigated materials, as several coverage states are in equilibrium at conditions close to standard temperature and pressure, so that the reaction should not require high overpotentials to be carried out. On the contrary, all (011) and (111) surfaces are shown to be less suitable for HER: the interaction between molecular hydrogen and the material is too strong for the former to be efficiently released and therefore the reaction would have to be driven by a

significant overpotential. When comparing these results to those that are obtained through the use of a volcano plot, it is clear how there is a qualitative agreement between the two, as the variability in coverage states is possible due to the mildly exothermic or mildly endothermic nature of the adsorption of hydrogen on the (001) surfaces of these carbides, which are often correlated with the high catalytic activity of platinum and iridium.[15,67,137] The methodology presented here, however, adds a theoretical background to the use of the volcano plot, extending its use: surfaces such as TiC(011), which would be considered impractical for catalytic use due to their too high $E_{ads}$, are here considered viable for application at reaction conditions that differ from standard temperature and pressure. Furthermore, the activity of the (001) surfaces is now correlated to their coverage states, providing further insight in the reaction at conditions closer to those at which the HER is carried out without the need for complex and expensive DFT calculations at the solid – liquid interface.

*Summary and conclusions*

Our study of hydrogen adsorption on carbide surfaces shows that the $C_{on\ top}$ is the preferred adsorption site in all cases, which is always exothermic except for NbC(001). Metal sites are less favourable on all surfaces on which they are in competition with $C_{on\ top}$ sites, but show a stronger interaction as the number of coordinated metals increases, so that $M_3$ sites provide a strong hydrogen adsorption on (111) surfaces. On both carbon and metal sites, the energetic trends and adsorption properties are consistent across all four carbides studied. For all surfaces and coverages, reactivity on VC and NbC corresponds to less exothermic adsorption energies with respect to the same reactions over TiC and ZrC, showing a clear effect of the periodic group of the parent metal. The effect of the row in the periodic table is less marked, but in some cases the reduced lattice parameter for the carbides of the 4th row induces steric effects that hinder the adsorption. These trends could in some cases be related to the electronic characteristics of the surfaces. Across all carbides, (111)-C surfaces highlight the highest reactivity, but are unstable for the Group 4 carbides TiC and VC. (111)-M and (011) surfaces also provide very strong adsorptions, while the $E_{ads}$ reported for (001) surfaces are always close to 0 eV. The *d*-band centre positions have been proven to correlate with the activity of the material over the hydrogen adsorption for all surfaces and could therefore be used as descriptors. Similarly, a correlation could be found between the increase in coverage and a decrease in both $|\Delta E_{ads}|$ and $\Phi$: as more

hydrogens are added on a surface, more electrons are added to the conduction band of the solid, thereby obstructing further hydrogenation of the slab and simultaneously lowering the energy required to extract an electron from the surface. Nonetheless, the total adsorption energy becomes more negative as long as exothermic adsorption sites are used, as the decrease in exothermicity with coverage is small compared to the total value of adsorption energy. As a results, an *ab-initio thermodynamics* analysis of the data collected showed how the only coverage state displayed by (011) and (111) surfaces is that of $\theta = 1$, which might hinder their catalytic activity towards HER as the hydrogen is bound too strongly to desorb. On the contrary, the (001) surfaces of TiC, VC, ZrC, NbC show the most promise as hydrogen evolution reaction catalysts among those tested.

# Chapter 5:
# $CO_2$ reduction on transition metal carbides

*The choice of carbide*

The use of transition metal carbides as catalysts for $CO_2$ activation and reduction has been reported both experimentally and computationally, as highlighted in Chapter 1. However, little computational work has been performed to understand the mechanism of such reactions on early transition metal carbides. For other carbides, such as $Mo_xC$, it has been shown how the reaction pathway and the final product of the reduction depend on the stoichiometry of the material and its surface structure. For this reason, we investigated the dissociation and hydrogenation of $CO_2$ on several surfaces of early-TMCs, with the objective of identifying the most favourable pathways on each material and highlight the most active catalyst. However, the scope of the project did not allow for a simultaneous investigation of all the materials studied in the previous chapter for hydrogen evolution, so we turned to the literature as well as our own previous work in order to choose which carbides and surfaces should be investigated. *Quesne et al.*[102] highlighted a correlation between the $CO_2$ adsorption energy and its bond elongation once adsorbed, as well as calculating the charge transfer between molecule and surface upon adsorption on early-TMCs. Bond elongation and charge transfer data highlight an interesting activity for ZrC surfaces, which is shown to both bend and reduce the adsorbed molecule more than other carbides. Similarly promising results are also reported for TiC, which was also predicted to show easy adsorption and desorption of hydrogen over its (001) surface in the previous chapter of this work. Since both the C-O bond elongation and the charge transfer upon adsorption have previously been linked with the molecule activation,[81] and given the role hydrogen coverage plays in $CO_2$ reduction to hydrocarbons, TiC and ZrC where chosen for a thorough investigation of their catalytic activity over $CO_2$ dissociation and hydrogenation upon their low-index surfaces. Initially, the adsorption of $CO_2$ is investigated on all low-index surfaces of TiC and ZrC; secondly, the adsorption of CO, O, COOH and HCOO is also considered in order to obtain information on the reactions of dissociation and hydrogenation on those surfaces; lastly, the reaction paths

connecting $CO_2$ to the reduced species are studied, identifying the corresponding transition states and predicting the most favourable reaction path on each surface.

## 5.1 Adsorption of $CO_2$ on TiC and ZrC surfaces

We first investigated the adsorption of $CO_2$ on TiC and ZrC. For each material, the (001), (011) and (111) surfaces were investigated. Due to the instability of the carbon-terminated (111) surface, discussed in Chapter 4, only the metal termination of such plane has been considered. Several favourable adsorption sites were found on each surface, and their analysis constitutes the first part of this chapter.

*Adsorption energies and geometries*

$CO_2$ was placed on the (001) surface of TiC in several positions with distinct local geometries, identifying three adsorption sites. In all three cases, shown in Figure 5.1 and further described in the corresponding table, a covalent C-C bond is established with a surface carbon atom, bending the structure to form an O-Ĉ-O angle of $\theta \approx 120°$. The $C_{on\ top\ (M)}$ and $C_{on\ top\ (C)}$ adsorption sites both present the O-Ĉ-O molecular plane perpendicular to the surface, only differing by the coordination of the two oxygen atoms: in the former case, lower in energy, interaction with the surface is optimised by coordinating the two oxygen atoms with adjacent surface metal atoms; in the latter, the $CO_2$ molecule is rotated by 45° around the axis perpendicular to the surface and points towards the adjacent surface carbon atoms. The change in oxygen coordination is reflected in the adsorption energy $E_{ads}$, defined in Chapter 2, which changes from -0.85 eV to -0.50 eV. Similar coordination between oxygen and metal is found in the $M_2C$ site; in this case the $CO_2$ molecular plane has a ~60° inclination over the surface plane, leaning towards the coordinated surface metal atoms, and a slightly higher adsorption energy at -0.90 eV. Two of these adsorption sites are also found on ZrC, namely the $C_{on\ top\ (M)}$ and the $M_2C$, exhibiting very similar bond distances, bond angles and adsorption angles over the surface, as reported in Table 5.1. Similarly to what was highlighted in Chapter 4 for molecular hydrogen, adsorption $CO_2$ on ZrC is more exothermic than on TiC, with adsorption energies up to $E_{ads} = -1.68\ eV$ on the $C_{on\ top\ (M)}$ adsorption site.

| *(001)* | $E_{ads}$ / *eV* | $d_{C-C}$ / *Å* | $d_{C-O}$ / *Å* | $\theta_{O\text{-}\hat{C}\text{-}O}$ | *Inclination* | $\Delta q$ / *a. u.* |
|---|---|---|---|---|---|---|
| ***TiC*** | | | | | | |
| $C_{on\ top\ (C)}$ | -0.50 | 1.45 | 1.29 | 127° | 90° | +0.95 |
| $C_{on\ top\ (M)}$ | -0.85 | 1.48 | 1.29 | 128° | 90° | +0.89 |
| $M_2C$ | -0.90 | 1.49 | 1.30 | 122° | 62° | +0.85 |
| ***ZrC*** | | | | | | |
| $C_{on\ top\ (M)}$ | -1.68 | 1.47 | 1.30 | 124° | 90° | +0.98 |
| $M_2C$ | -1.48 | 1.47 | 1.31 | 121° | 70° | +1.04 |

**Table 5.1.** *Adsorption of $CO_2$ on TiC(001) and ZrC(001). The table highlights, from left to right, the adsorption energy, distance to the nearest surface carbon atom, C-O bond distance, O-Ĉ-O bond angle, inclination of the molecular plane with respect to the surface plane, and variation in charge with respect to gas phase $CO_2$ of the adsorbed molecule, for each adsorption site.*

On the two (011) surfaces, two adsorption sites have been identified, named $C_{on\ top}$ and $M_4C$. As with those described earlier, both these adsorption sites coordinate the central carbon atom of $CO_2$ to a surface carbon atom, bending the adsorbed molecule. The difference between $C_{on\ top}$ and $M_4C$ sites is in the coordination of the $CO_2$ oxygen atoms and in the angle between the molecular plane and the surface. In the former case, the adsorption site is analogous to that of the $C_{on\ top\ (O)}$ site found on (001) surfaces, as the $CO_2$ molecular plane is similarly found to be perpendicular to the surface and the C-O bonds are only slightly more elongated ($\Delta d_{C\text{-}O}$ = +0.02 Å on both carbides); in the latter site, the morphology of surface allows for the oxygen atoms to be coordinated by 2 metal atoms each, reducing the angle between the molecule and the surface to 45° and elongating the C-O bonds to 1.37 Å on both carbides, as well as producing a slightly more negative $E_{ads}$ on both carbides. On all (011) adsorption sites, the corrugated surface allows for shorter C-C bonds (0.1 – 0.3 Å shorter than the respective sites on (001) surfaces) and significantly more exothermic adsorption, ranging from -3.4 eV on TiC(011) – $C_{on\ top}$ to -4.2 eV on ZrC(011) – $M_4C$. Comparing

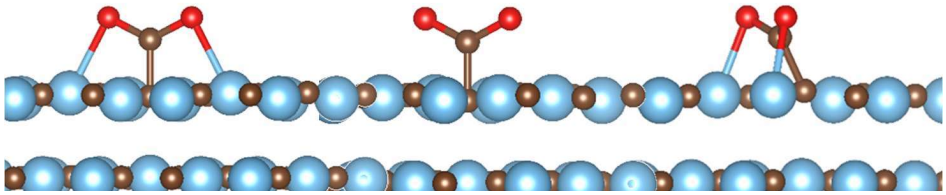

**Figure 5.1.** *$CO_2$ adsorption sites on TiC(001). From left to right: $C_{on\ top\ (O)}$, $C_{on\ top\ (C)}$ and $M_2C$. The first and last adsorption sites are also found on ZrC(001). The colour scheme is as follows: Ti = blue, C = brown, O = red.*

these results with those highlighted in ref(102) shows similar numbers for $E_{ads}$ and bond elongation, with the exception of ZrC(011), which present much larger adsorption energies than those reported in ref(102). That is due to the fact that a different adsorption site is investigated in that paper, similar to ZrC(011) – $C_{on\ top}$ but rotated by 90° around the C-C axis, reducing the interaction with the surface metal atoms and therefore in a less negative adsorption energy.

| *(011)* | $E_{ads}$ / *eV* | $d_{C-C}$ / *Å* | $d_{C-O}$ / *Å* | $\theta_{O\text{-}\hat{C}\text{-}O}$ | *Inclination* | *Δq / a. u.* |
|---|---|---|---|---|---|---|
| ***TiC*** | | | | | | |
| $C_{on\ top}$ | -3.42 | 1.40 | 1.31 | 127° | 90° | +1.00 |
| $M_4C$ | -3.45 | 1.38 | 1.37 | 126° | 45° | +1.27 |
| ***ZrC*** | | | | | | |
| $C_{on\ top}$ | -4.04 | 1.41 | 1.32 | 124° | 85° | +1.05 |
| $M_4C$ | -4.19 | 1.39 | 1.37 | 123° | 43° | +1.36 |

**Table 5.2.** *Adsorption of $CO_2$ on TiC(011) and ZrC(011). The table highlights, from left to right, the adsorption energy, distance to the nearest surface carbon atom, C-O bond distance, O-Ĉ-O bond angle, inclination of the molecular plane with respect to the surface plane, and variation in charge with respect to gas phase $CO_2$ of the adsorbed molecule, for each adsorption site.*

The (111) surfaces of both carbides have been investigated as a purely metal-terminated facet, for the reasons explained above. On these surfaces, $CO_2$ once again acquires a bent geometry upon adsorption, forming an acute angle between the plane of the surface and that of the molecule. In such a configuration each atom forming $CO_2$ can sit on top of a metal atom, bridging two metal atoms or at the barycentre of a triangle formed by three metal atoms, resulting in a wide array of adsorption sites with similar characteristics and energetics. It was possible to identify four such adsorption sites on TiC, which are shown in Figure 5.3, and three on ZrC. On both carbides, two of the identified adsorption sites show the $CO_2$ molecular plane parallel to that of the surface, each atom of the substrate coordinating 3 surface metal atoms, for a total of 5; the two sites only differ by the position of $CO_2$ with respect of the lower layers, as the central $CO_2$ carbon atom can sit on top of either a metal or a carbon atom, with the

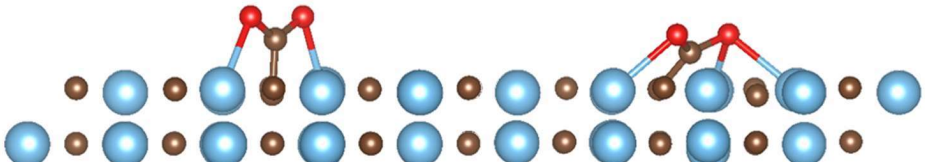

**Figure 5.2**. *$CO_2$ adsorption sites on TiC(011): $C_{on\ top}$ (left) and $M_4C$ (right). Analogous sites are found on ZrC(011). The colour scheme is as follows: Ti = blue, C = brown, O = red.*

latter case corresponding to an adsorption which is more exothermic by 0.2 eV. The latter adsorption site, named $M_5M$, is the most exothermic on both TiC(111) and ZrC(111), as highlighted in Table 5.3. On the two remaining sites, the two oxygen atoms of $CO_2$ are not chemically equivalent anymore, and the one more strongly coordinated by the surface shows a significantly more elongated C-O bond.

| *(111)* | $E_{ads}$ / *eV* | $d_{C-M}$ / *Å* | $d_{C-O}$ / *Å* | $\theta_{O\text{-}\hat{C}\text{-}O}$ | *Inclination* | *Δq / a. u.* |
|---|---|---|---|---|---|---|
| ***TiC*** | | | | | | |
| $M_5C$ | -2.90 | 1.46 | 1.40 | 114° | 0° | +1.76 |
| $M_{3\text{-}bent}$ | -2.55 | 1.54 | 1.45* | 118° | 20° | +1.62 |
| $M_5M$ | -3.11 | 1.39 | 1.36 | 117° | 5° | +1.77 |
| $M_4C$ | -2.93 | 1.50 | 1.46* | 113° | 10° | +1.77 |
| ***ZrC*** | | | | | | |
| $M_5C$ | -2.82 | 1.51 | 1.37 | 114° | 0° | +1.73 |
| $M_5M$ | -3.17 | 1.45 | 1.36 | 116° | 20° | +1.83 |
| $M_4C$ | -2.82 | 1.56 | 1.47* | 113° | 10° | +1.79 |

**Table 5.3.** *Adsorption of $CO_2$ on TiC(111) and ZrC(111). The table highlights, from left to right, the adsorption energy, distance along the Z-axis of the carbon atom from $CO_2$ to the plane of the surface, C-O bond distance, O-$\hat{C}$-O bond angle, inclination of the molecular plane with respect to the surface plane, and variation in charge with respect to gas phase $CO_2$ of the adsorbed molecule, for each adsorption site. In some cases, the two oxygen atoms of $CO_2$ are not equivalent once the molecule is adsorbed on (111) surfaces. When this happens, the value reported for $d_{C-O}$ is referred to the most elongated bond of the two, and the number is marked with *.*

### *Trends of $CO_2$ adsorption on early-TMCs surface*

All surfaces of TiC and ZrC show favourable chemical adsorption of $CO_2$, which is strongly bound to a surface carbon atom on (001) and (011) surfaces, and coordinated to the whole surface on the (111) surface. Because of this, (001) and (011) surface primarily coordinate the $CO_2$ central carbon atom, which is the closest to the surface, while the two (111) surfaces strongly bound the two oxygen atoms. Energetically, a

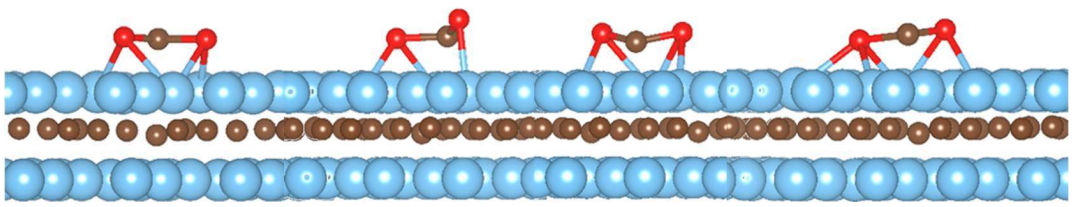

**Figure 5.3** *$CO_2$ adsorption geometries on TiC(111). From left to right: $M_5C$, $M_{3\text{-}bent}$, $M_5M$, and $M_4C$. On ZrC(111) analogous adsorption sites, with the exception of $M_{3\text{-}bent}$, are found. It is easily seen from these pictures how the oxygen atoms are chemically equivalent in $M_5C$ and $M_5M$, but are not in $M_{3\text{-}bent}$ and $M_4C$. The colour scheme is as follows: Ti = blue, C = brown, O = red.*

trend similar to that highlighted in the previous chapter for hydrogen adsorption could be identified:

$$|E_{ads}(011)| > |E_{ads}(111)| \gg |E_{ads}(001)|$$

$$|E_{ads}(ZrC)| > |E_{ads}(TiC)|$$

The particularly high adsorption energies for (011) facets can be related to the specific morphology of these surfaces: due to their corrugation, they can both form a strong C – C bond with $CO_2$ and coordinate its oxygen atoms to the surface metal atoms, while (001) and (111) surfaces can only efficiently do the former and the latter respectively. Moreover, in all investigated cases $CO_2$ is bent, its C – O bonds elongated and its central carbon atom partially reduced upon adsorption, as highlighted in Tables 5.1 to 5.3. These characteristics form trends similar to that followed by adsorption energies, but with a few exceptions, most notably the absence of a clear activation sequence between the two carbides. (001) surfaces show consistently the least $CO_2$ activation, bending the O-Ĉ-O bond to ~120° similarly to (011) surface but reducing the molecule less – the only charge differences $\Delta q < 1$ eV are found upon adsorption on (001) surfaces – and causing a shorter bond elongation, up to 0.12 Å. (011) surfaces are in line with (001) surfaces in terms of $\theta_{O\text{-}\hat{C}\text{-}O}$ but show longer $d_{C-O}$ and higher $\Delta q$. (111) surfaces, albeit not showing the highest adsorption energy, are the ones that alter the nature of $CO_2$ the most upon adsorption, increasing $d_{C\text{-}O}$ and reducing $\theta_{O\text{-}\hat{C}\text{-}O}$ the most while transferring a charge of almost 2 $e^-$ to the molecule.

These characteristics of bond elongation, geometry change and charge transfer have previously been linked to an activation of the molecule.[81,102] Our data therefore suggest that the (111) surfaces of TiC and ZrC should be the most reactive upon $CO_2$ reduction. To investigate this prediction we have studied the $CO_2$ reduction on TiC and ZrC surfaces in terms of its dissociation to CO, hydrogenation to COOH, and hydrogenation to HCOO.

## 5.2 $CO_2$ reduction on TiC and ZrC

*CO, COOH and HCOO on TiC and ZrC surfaces*

Carbon monoxide, formic acid and methanol are some of the most valuable and useful products of $CO_2$ reduction.[12] Posada-Pérez *et al.*[126] previously showed how surface

morphology and stoichiometry can drive the selectivity towards either product through a variety of reaction paths. On the initial step, $CO_2$ might dissociate yielding CO and O on the surface of the carbide; the former can be either directly desorbed or further reduced to methanol, while the latter is reduced to $H_2O$ and desorbed. Alternatively, $CO_2$ can be directly hydrogenated either on C or on O, yielding respectively a carboxyl or a formate on catalyst surface. The latter can be further hydrogenated to formic acid, or either intermediate might instead undergo dissociation of one C-O bond activated by the presence of H on either atom, and subsequent further reduction by $H_2$ to $CH_3OH$ and $H_2O$. The resulting overall reactions are therefore:

$$CO_2 + H_2 \rightarrow CO + H_2O$$

$$CO_2 + H_2 \rightarrow HCOOH$$

$$CO_2 + 3\ H_2 \rightarrow CH_3OH + H_2O$$

The first reaction is of course the reverse Water-gas shift reaction, and results in a product which is more economically valuable[12] but more oxidised. Formic acid and methanol, while less valuable, can be used to generate electricity in fuel cells[138,139] or as a building block for fuels and chemicals.[12] The first step of each of these reactions has been investigated in both the thermodynamic and kinetic aspects, modelling the formation of the three first-step intermediates on each surface:

$$CO_2 \rightarrow CO + O$$

$$CO_2 + ½\ H_2 \rightarrow COOH$$

$$CO_2 + ½\ H_2 \rightarrow HCOO$$

The adsorption of each of the involved chemical species on all TiC and ZrC surfaces has therefore been studied, identifying the minimum energy structures shown in Figure 5.4 and highlighting the adsorption energies reported by Table 5.4.

| | CO | O | COOH | HCOO |
|---|---|---|---|---|
| ***TiC*** | | | | |
| *(001)* | -1.82 ($C_{on\ top}$) | -2.54 ($M_2C$) | -1.25 ($M_2C$) | -2.08 ($C_{on\ top}$) |
| *(011)* | -3.22 ($C_{on\ top}$) | -4.40 (M-O-C) | -1.82 ($M_4C$) | -5.35 ($M_4C$) |
| *(111)* | -3.22 (M2) | -5.76 ($M_3$) | -1.20 ($M_{4\ -\ vertical}$) | -6.12 ($M_{5\ -\ up}$) |
| ***ZrC*** | | | | |
| *(001)* | -2.13 ($C_{on\ top}$) | -2.79 ($M_2C$) | -1.70 ($M_2C$) | -3.29 ($C_{on\ top}$) |
| *(011)* | -3.91 (C-$M_{bridge}$) | -4.56 ($M_{2\ -\ bridge}$) | -3.74 ($C_{on\ top}$) | N/A |
| *(111)* | -3.13 ($M_2$) | -5.85 ($M_3$) | -2.46 ($M_{4\ -\ vertical}$) | -6.17 ($M_{5\ -\ up}$) |

**Table 5.4.** *Adsorption energies for CO, O, COOH and HCOO on TiC and ZrC in eV. Only the most favourable adsorptions sites are considered in this table.*

Adsorption of CO is generally very exothermic (-1.82 eV to -3.91 eV) on all surfaces, compared to the gas phase molecule. $C_{on\ top}$ sites are dominant on both (001) surfaces, as shown by Figure 5.4 (a), in which the molecule stands almost perpendicular to the plane of the catalyst, only slightly leaning towards a metal atom; on these sites, the C-O bond shows significant elongation (1.20 Å), as the distance between the adsorbed molecule and the nearest surface carbon atom also resembles that of a strong covalent C-C bond at 1.32 Å. (011) surfaces present the most exothermic CO adsorption on both carbides, similarly to the previously highlighted case of $CO_2$; Figure 5.4 (b) show how the morphology of the surface drives the most favourable adsorption sites towards a state in which the CO molecule is covalently bound to a surface carbon atom and coordinated to a neighbouring metal atom, with significant bond elongation (1.27 Å on ZrC, where the oxygen is coordinated to two metal atoms). (111) surfaces offer multiple coordination patterns, resulting in low energy structures where both atoms of CO maximise coordination by lying almost parallel to the surface, as highlighted by Figure 5.4 (c). Isolated oxygen atoms are bound very strongly to all surfaces (-2.5 eV to -5.9 eV). On (001) surfaces adsorbed O is coordinated to one carbon and two metal atoms. On (011), oxygen interacts very strongly with carbon atoms, pulling them strongly out of the plane of the surface. On (111), O fits in the hexagonal sites coordinating three metal atoms, binding strongly to the surface.

The carbonyl group formed by hydrogenation of $CO_2$ on one of the oxygen atoms also presents different preferred geometries on the various surfaces. On both (001) surfaces, two planar structures could be identified: the first, $C_{on\ top}$, has its molecular plane perpendicular to the surface and presents a slightly bent geometry which maximises the distance between the -OH group and the surface; the second, $M_2C$, is instead bent towards the surface in order to maximise interaction between the latter

and the oxygen atoms. The two structures have very similar energies ($\Delta E < 0.05$ eV), with the latter being more favourable and therefore being shown in Figure 5.4 (a). On (011), similar structures are found; however, each is favoured on a different carbide, with $C_{on\ top}$ being stable on ZrC while $M_2C$ is favoured on TiC. On the (111) surface of both carbides, the COOH group is most stable when aligned perpendicularly to the surface, with C=O coordinated to the surface and -OH pointing upwards. Formate groups formed by hydrogenation of a $CO_2$ carbon atom are not stable on ZrC(011), giving spontaneous dissociation to an sp2 hybridized HCO on a $C_{on\ top}$ site with O coordinated to a metal, plus adsorbed oxygen. The same situation could be found on TiC(011), but in this case a surface formate intermediate could be isolated, shown in Figure 5.4 (b). On the four other surfaces HCOO presents stable configurations similar to those of COOH, with $C_{on\ top}$ and $M_{5-up}$ respectively being the most favoured on (001) and (111) surfaces respectively, on both carbides.

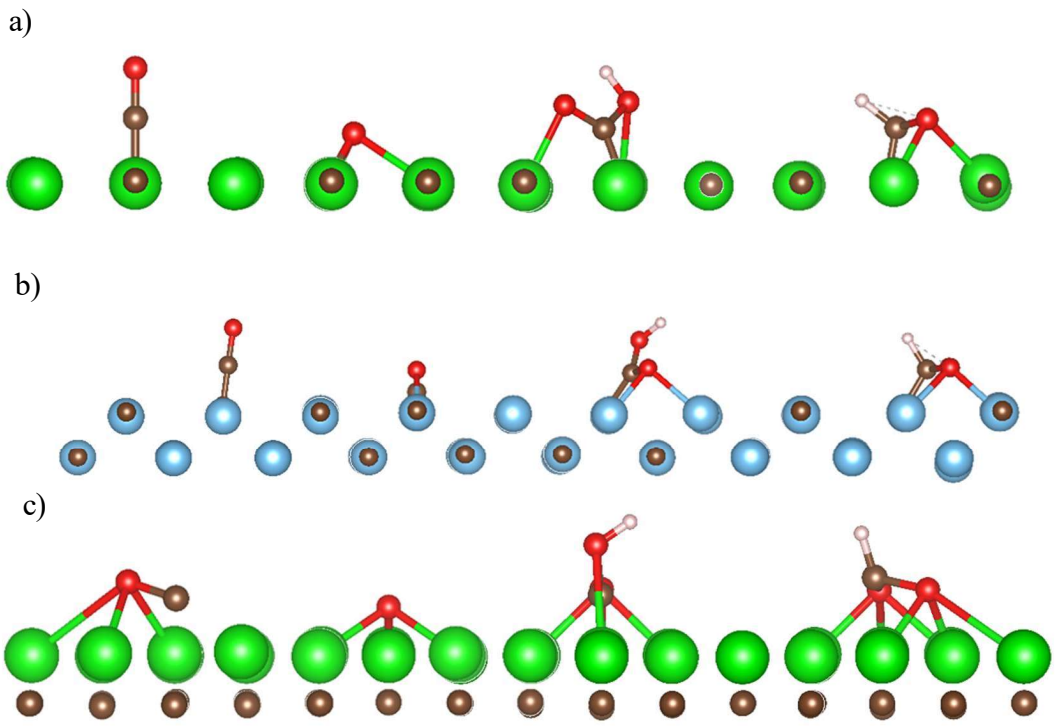


**Figure 5.4** *Most favourable adsorption geometries of, from left to right, CO, O, COOH and HCOO on a) ZrC(001), b) TiC(011), c) ZrC(111). Analogous geometries are found for all species on the carbide not shown in this picture, with the exception of HCOO on ZrC(011), which spontaneously dissociates upon adsorption. The adsorption geometries shown here are those with the minimum energy among those tested on each surface. The colour scheme is as follows: Ti = blue, Zr = green, C = brown, O = red, H = pink.*

*$CO_2$ dissociation and hydrogenation*

The energetics of the processes described above have been compared to those of the gas phase and adsorbed reactants according to the three investigated reaction paths. Nearly all reactions are strongly exothermic compared to the combined energy of the pristine surface and gas phase reactants. As shown in Table 5.5, however, the energy of the reaction step is only negative for the dissociation reactions, while it can be significantly positive for the two hydrogenation pathways.

| | **CO + O** | | **COOH** | | **HCOO** | |
|---|---|---|---|---|---|---|
| | vs. $CO_{2\,(g)}$ | vs. $CO_2^*$ | vs. $CO_2$, $H_{2\,(g)}$ | vs. $CO_2^*$, $H_2^*$ | vs. $CO_2$, $H_{2\,(g)}$ | vs. $CO_2^*$, $H_2^*$ |
| *TiC* | | | | | | |
| *(001)* | -1.13 | -0.23 | -1.25 | 0.59 | 0.19 | 2.03 |
| *(011)* | -7.05 | -3.6 | -3.38 | 1.43 | -3.38 | 1.43 |
| *(111)* | -5.70 | -2.60 | -2.76 | 1.43 | -3.84 | 0.35 |
| *ZrC* | | | | | | |
| *(001)* | -1.72 | -0.04 | -1.70 | 0.95 | -1.02 | 1.63 |
| *(011)* | -5.03 | -0.84 | -3.73 | 1.71 | -5.92* | -0.48* |
| *(111)* | -5.67 | -2.49 | -2.47 | 1.91 | -3.9 | 0.48 |

**Table 5.5** *Reaction energies (in eV) for the dissociation to CO + O, hydrogenation to COOH and hydrogenation to HCOO. For each reaction two energies are reported, differing for the reference used: in the column on the left of each section, the energy "vs. $CO_{2\,(g)}$" or "vs. $CO_2$, $H_{2\,(g)}$" is reported, which is the energy of the intermediate on the surface of the catalyst minus the energy of the gas phase reactants and pristine surface; in the column on the right of each section, the energy "vs. $CO_2^*$ or "vs. $CO_2^*$, $H_2^*$" is reported, which is the energy of the intermediated on the surface of the catalyst minus the energy of the reactants on the same surface, also referred to as single-step reaction energy. The energies reported for HCOO on ZrC(011) are marked with * because they are referred to the formation of HCO + O, since HCOO dissociation happens spontaneously on this surface.*

Table 5.5 summarises the reaction energies correlated with the formation of CO, COOH and HCOO, reported with respect to gas phase $CO_2$ (and ½ $H_2$ in the case of hydrogenation) as well as referred to the single reaction step from adsorbed $CO_2$. The dissociation reaction is the only one for which single-step energies are negative. This is obviously related to the high adsorption energies found for CO and O, which strongly bind to the surfaces of TiC and ZrC, allowing for an exothermic reaction energy. On the contrary, single-step reaction energies for formation of COOH and HCOO are generally endothermic, as a result of the relative instability of these intermediates. Nevertheless, the reaction energy from gas phase reactants are generally exothermic, with the only exception of the formation of HCOO on the TiC(001) surface, for which $E_{react}$ = +0.19 eV. As a result, it is possible that the adsorption of $CO_2$ and $H_2$ on the low-index surfaces of TiC and ZrC might provide the energy for

the formation of these intermediates on the catalysts, so their formation cannot be ruled out on the sole basis of single-step reaction energy. The endothermicity of $CO_2$ hydrogenation can also be linked with the results of hydrogen adsorption on TMCs presented in Chapter 4 of the present work: since hydrogenation on TiC and ZrC surfaces is always exothermic, energy is required for the formation of HCOO and COOH, as one strongly bound H atom has to be pulled from the surface. This is particularly true for (011) and (111) surfaces, because of their more exothermic adsorptions, which result in the high single-step reaction energies for COOH formation on these facets. HCOO formation, however, is less thermodynamically unfavourable on (111) surfaces, due to the very strong bond between this intermediate and the surface.

From the results of Table 5.5 it is also possible to preliminarily assess how the three competitive reactions are balanced on each surface. In absolute terms, the dissociation is always thermodynamically favoured, as it always shows $E_r < 0$ for the single-step process. However, if only the hydrogenation reactions are considered, a strong preference towards the formation of COOH is found on (001) surfaces, while on (111) surfaces the preference is towards the formation of HCOO, which on TiC(111) has the least positive single step reaction energy of all hydrogenated intermediates. On the two (011) surfaces, the formate is not stable, and can dissociate spontaneously to CHO + O. It was possible to identify a formate intermediate on TiC(011), which shows $E_r = 1.43$ eV, the same of $CO_2$ hydroxylation. On ZrC(011), instead, HCOO is so unstable on this surface that undergoes spontaneous dissociation and no intermediate could be found. Table 5.5 reports $E_r = -0.48$ eV for this reaction, but this is referred to the formation of CHO + O.

To evaluate the selectivity of each surface, the simple prediction of reaction energies is therefore not sufficient. Nudged elastic band calculations (NEB and *c*NEB, see Chapter 2.3 for more details) and the dimer method have been employed in order to sample the region of the potential energy surface connecting each intermediate to their adsorbed reactants, identifying the transition states corresponding to the reactions leading to CO, COOH, and HCOO on (001), (011) and (111) surfaces. From this investigation, two reactions have been excluded: the formation of formate on TiC(001) and ZrC(001) have been considered too high in energy to take place, the former

showing the only positive reaction energy from gas phase reactants, the latter being strongly unfavourable compared to COOH formation.

## 5.3 Exploring the potential energy surface

*Transition state calculations*

Figure 5.5 shows the initial state, transition state, and final state of the PES linking adsorbed $CO_2$ and H to COOH on TiC(001), $CO_2$ to CO and O on ZrC(011), and $CO_2$ and H to HCOO on TiC(111). Similar pictures could be drawn for all other reactions reported in Table 5.4, but also for the several other paths that have been investigated for each reaction. Each investigation is started by selecting suitable initial and final states: a model is created for each one so that the change between the two is minimal and limited to the reaction path in study. As an example, in the case of the hydrogenation path shown in Figure 5.5 (a) this is done by placing the $CO_2$ molecule of the initial state model on the same surface carbon atom as the COOH molecule of the final state model, and the reducing H atom of the initial state model on a neighbouring adsorption site. Several combinations of the relative positions of the reactants between each other and with the product are then created by selecting different adsorption sites for each species and changing the orientation of the O – H bond in the final state, in order to capture the different reaction paths which might generate the product of interest. For most of the transition states reported here, the MEP was found using neighbouring adsorption sites for $CO_2$ and H or CO and O, corresponding to the minimum distance between these species in their stable adsorbed state.

A nudged elastic band (NEB, see Chapter 2 for more details) calculation is then performed between each initial state - final state couple, in order to find the minimum energy path (MEP) connecting the two. Once converged, the MEPs related to different configurations of the same reaction are compared, selecting the best ones and performing on these either a *c*NEB or a dimer calculation in order to isolate their transition states. The results of these calculations can then be confirmed to be the transition state correlated with the hydrogenation or dissociation path under investigation by inspecting the vibrational frequencies of the adsorbate on the surface: because of the characteristics of the PES around these points (more extensively

discussed in Chapter 2) the transition state will show a single imaginary vibrational frequency, which will be the result of an imaginary mode of vibration corresponding to the formation or cleavage of the bond in interest – in our case, the O – H bond for $CO_2$ hydrogenation and the C – O bond for its dissociation. The results obtained through this protocol are summarised in Table 5.4.

| ***TiC*** | **Gas Phase** | **Transition state** | **Product** |
|---|---|---|---|
| *001 – CO* | +0.90 | +2.13 | -0.23 |
| *011 – CO* | +3.45 | +0.69 | -3.6 |
| *111 – CO* | +3.11 | +0.99 | -2.60 |
| *001 – COOH* | +1.84 | +1.58 | +0.59 |
| *011 – COOH* | +4.80 | +2.15 | +1.43 |
| *111 – COOH* | +4.19 | +2.15 | +1.43 |
| *001 – HCOO* | +1.84 | N/A | +2.03 |
| *011 – HCOO* | +4.80 | +1.39 | +1.43 |
| *111 – HCOO* | +4.19 | +1.44 | +0.35 |
| ***ZrC*** | | | |
| *001 – CO* | +1.68 | +1.86 | -0.04 |
| *011 – CO* | +4.19 | +0.49 | -0.84 |
| *111 – CO* | +3.18 | +1.29 | -2.49 |
| *001 – COOH* | +2.65 | +1.48 | +0.95 |
| *011 – COOH* | +5.44 | +1.97 | +1.71 |
| *111 – COOH* | +4.38 | +2.44 | +1.91 |
| *001 – HCOO* | +2.65 | N/A | +1.63 |
| *011 – HCOO* | +5.44 | > 3 eV | -0.48* |
| *111 – HCOO* | +4.38 | +1.58 | +0.48 |

**Table 5.4** *Activation and reaction energies of $CO_2$ reduction over TiC and ZrC. All energies are referred to the adsorbed $CO_2$ – for dissociation reactions – or $CO_2$ + H – for hydrogenation reactions – and are reported in eV. The first column refers to the energy of the gas phase reactants, so is equivalent to the opposite of the adsorption energy; the second row is the activation energy, hence the energy difference between the adsorbed reactant and the transition state; the third and final row reports the energy of the products referred to that of the reactants.*

### *Activation barriers*

While the reaction energies and activation barriers for hydrogenation are high, it must be kept in mind that these are related to the single-step reactions in which $CO_2$ and H are adsorbed; the energy of the gas phase reactants relative to their adsorbed state is then also reported in Table 5.4. Dissociation to CO on both (001) surfaces show mildly exothermic reaction energies coupled with very high barriers – over 2 eV for TiC(001). This highlights how, even if the (001) surface can chemisorb both reactants and products efficiently, $CO_2$ is not sufficiently activated on these surfaces to obtain a seamless reduction. It is possible to correlate this result with the bond elongation and

electron transfer data: $CO_2$ adsorbed on TiC(001) and ZrC(001) shows longer bond lengths, a bent geometry and a higher number of electrons than the gas phase molecule, all characteristics that have been correlated with $CO_2$ activation.[76] Nonetheless, this activation is proved to be insufficient, since on both carbides the transition state has a higher energy than the gas phase reactants, effectively ruling out the direct dissociation of $CO_2$ on these surfaces.

The dissociation reaction is instead favourable on (011) and (111) surfaces, as the more exposed metal atoms are able to more efficiently coordinate $CO_2$ while the C-O bond is elongated until full dissociation. Dissociation on ZrC(011) is, of all reactions, that with the lowest energetic barrier ($E_a = 0.49\ eV$ over the adsorbed reactants), while TiC(011) shows the most exothermic reaction energy ($E_r = -3.60\ eV$) but has a slightly higher activation barrier, $E_a = 0.69\ eV$. This can be correlated to the higher metal area exposed on ZrC, which allows for a better coordination of the dissociating oxygen, but results in its less efficient coordination once the reaction is complete. However, this trend is inverted for the transition states on (111) surfaces: the longer cell parameters of ZrC mean that the dissociating oxygen cannot be coordinated as efficiently, resulting in a higher barrier than that on TiC(111).

Conversely, the hydrogenation reaction to carboxyl is most favourable on the (001) surfaces of TiC and ZrC. In all cases the reaction is endothermic and the barrier is at least 1.5 eV over the adsorbed state of the reactants. However, this energy can be provided by the adsorption energies of $CO_2$ and $H_2$ on the surfaces of the catalysts, as both are significantly larger than the activation barriers. This reaction is least unfavorable thermodynamically on TiC(001), where it shows a $E_r = +0.59\ eV$, while kinetically ZrC shows a slightly lower barrier of $E_a = +1.48\ eV$. The hydrogenation on both (011) and (111) surfaces is instead significantly endothermic and shows barriers of 2 eV and higher, hindering the formation of COOH on these four surfaces. As mentioned in the previous section, the strong bond formed by hydrogen with these surfaces can be considered as a reason for the high hydrogenation barriers found on this surface.

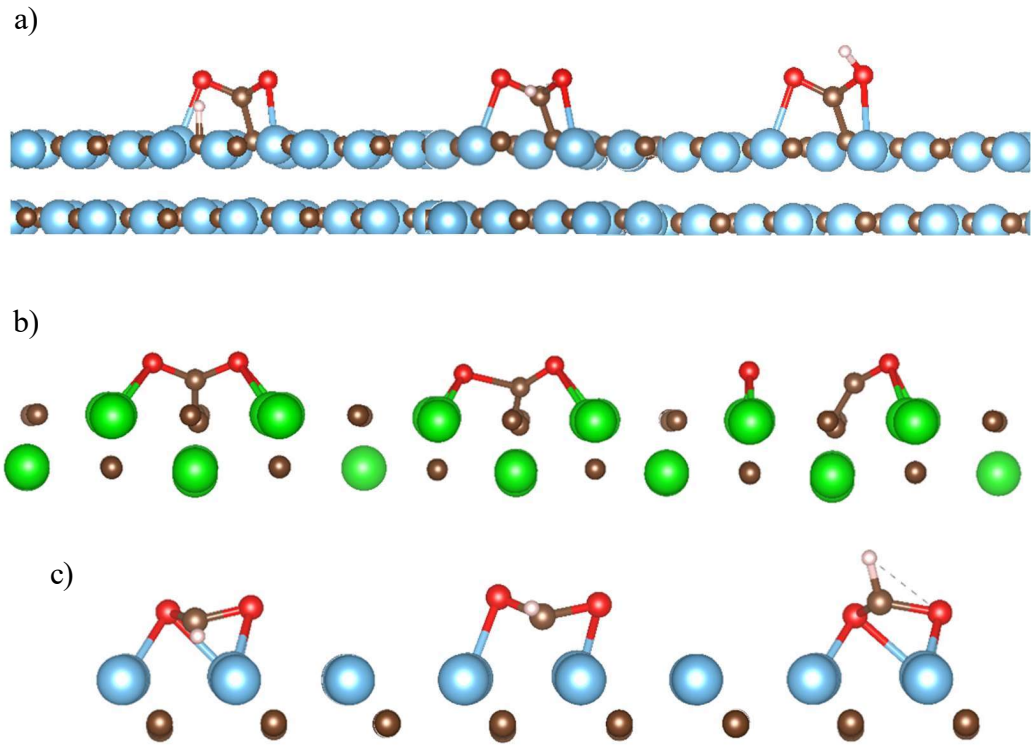


**Figure 5.5** *Proposed reduction mechanism of a) $CO_2$ hydrogenation to COOH on TiC(001), b) $CO_2$ dissociation to $CO + O$ on ZrC(011), c) $CO_2$ hydrogenation to HCOO on TiC(111). From left to right: initial state, in which the reactants are adsorbed on the surface of the catalyst; transition state, identified through the presence of one imaginary frequency related to the formation of the desired product; final state, in which the product is adsorbed on the surface of the reactant. The colour scheme is as follows: Ti = blue, Zr = green, C = brown, O = red, H = pink.*

Finally, the hydrogenation to formate presents an interesting case study, as the results vary greatly depending on the surface. On the (001) surfaces, as mentioned in the previous section, the reaction is so endothermic that no HCOO formation can take place, and no investigation of the potential energy surface has been performed. On the two (011) surfaces formate is not stable, and can dissociate spontaneously to CHO + O. It was possible to isolate an HCOO intermediate on TiC(011), for which a small barrier has been identified. This reaction is significantly more viable than hydrogenation to carboxyl despite its identical reaction energy, as $E_a(HCOO) = 1.47\ eV < E_a(COOH) = 2.44\ eV$. On ZrC(011), however, the barrier for the simultaneous hydrogenation and dissociation is found to be very close to the hydrogenated unstable intermediate HCOO in terms of geometry and electron transfer, resulting in a kinetic barrier $E_a > 3\ eV$, after which the intermediate spontaneously dissociates. The height of this barrier rules out the possibility of hydrogenation to

formate on the latter surface, as its significantly higher than $E_a = 1.97\ eV$ found for carboxyl production. Conversely, on both (111) surfaces, the reduction to formate is only mildly endothermic, with $E_r = 0.35$ eV on TiC. This is probably due to the conformation of the (111) surfaces of these materials, which allow for high interaction of the carbon and oxygen atoms of HCOO with the metal atoms of the material, while minimising interaction with hydrogen. Activation barriers on the two surfaces are similar – $E_a(TiC) = 1.44\ eV, E_a(ZrC) = 1.58\ eV$ – and in both cases much smaller than those found for COOH formation on the same surfaces and than the adsorption energies of $CO_2$ and $H_2$ on the surface, making this route potentially viable for (111) surfaces.

*Implications for $CO_2$ reduction catalysis*

The study of these reaction has provided us with a thorough understanding of the adsorption of carbon dioxide and its reduction to CO, COOH and HCOO on the low-index surfaces of TiC and ZrC catalysts. The catalytic properties of these materials have been first investigated in terms of the activation of $CO_2$ provided upon adsorption. Adsorption energies, charge transfer data, bond elongations and geometry changes have been analysed in order to identify descriptors for the catalytic behaviour of each surface. TiC(001) and ZrC(001) have been shown to activate $CO_2$ the least, even though a strong chemical bond with a surface carbon atom was created upon adsorption. (111) surfaces were shown to produce the highest C-O elongation as well as transferring the highest quantity of charge, but (011) surfaces can coordinate $CO_2$ better.

The first step of three different $CO_2$ reduction pathways was investigated for all six low-index surfaces, providing the groundwork for a further study of its recycling into CO, HCOOH or $CH_3OH$. In order to do this, the adsorption of CO, O, COOH and HCOO was studied, obtaining the thermodynamic data for the dissociation of $CO_2$ to carbon monoxide and its hydrogenation to either formate or carboxyl. The dissociation step was found to be exothermic on all surfaces, while the hydrogenation to either intermediate was found to be endothermic. Nonetheless, the high adsorption energy of $CO_2$ and $H_2$ upon the investigated surfaces could potentially provide the energy for these reactions, which have therefore been studied more thoroughly. The exception to this is the hydrogenation to HCOO on both (001) surfaces, which has a reaction energy

so high that no further investigation was deemed necessary to rule this reaction path out.

Finally, the potential energy surface connecting $CO_2$ with its reduced intermediates to carbon monoxide, formic acid and methanol was investigated. The (001) surface was found to be unable to catalyse dissociation reactions, as these have very high activation energies on both carbides. However, the hydrogenation to COOH, albeit endothermic, can take place on these surfaces. On the (011) surfaces the most favoured reaction path is that of dissociation, which highlights both the most exothermic and the most easily activated reactions of the 18 paths considered. HCOO is most easily formed on TiC(111) and ZrC(111), since their conformation helps stabilising both this intermediate and the transition state leading towards it, but (111) surfaces might also be able to catalyse dissociation reactions, albeit not as efficiently as (011) facets.

The present study has given us a thorough understanding of the first reduction step of $CO_2$ on the low-index surfaces of TiC and ZrC. This can give us indications both on our previous predictions of catalytic activity and on what can most effectively catalyse the full $CO_2$ reduction process. On the one hand, we must observe that, even though the (001) surfaces of these carbides did show some promising results in terms of $CO_2$ activation, they failed in coordinate $CO_2$ and H at the transition state level. This might lead us to reconsider the use of descriptors only considering adsorption as a viable tool for catalytic activity prediction. Moreover, computational studies of the activity of carbides have often been confined to this facet, while we have demonstrated how other surfaces might lead to better catalytic activity. On the other hand, this leads to the question of relationship between computational and experimental studies: while it is true that (011) surfaces are not often reported experimentally, works such as this might drive synthesis towards it when the material is designed as a RWGS catalyst. Finally, we are able to narrow down the number of pathways to be explored in a future computational work interested into the whole reduction process to high-value chemicals: the dissociation reaction and the hydrogenation to formate will be studied on the (011) and (111) surfaces of both carbides, the former leading to CO via the RWGS reaction and the latter leading to either formic acid or $CH_3OH$; the hydrogenation to carboxyl path will be studied on both (001) surfaces leading to $CH_3OH$ through further hydrogenation followed by dissociation of one C-O bond.

# Chapter 6: Summary and conclusions

A thorough computational study of two classes of materials for the catalytic conversion of water and carbon dioxide to synthetic and sustainable fuels and chemicals is presented here. The structure – property relationship of oxygen-doped graphitic carbon nitride has been studied in order to explain its activity in photocatalytic water splitting and help elucidate its structure, comparing it to previous models as well as to experimental graphitic carbon nitride geometries. The erratic nature of the oxygen position in the polymer has been proved to affect the localization of the valence band maximum and conduction band minimum, which can in certain case act as electron and hole traps. This effect provided a rationale for the superior performances in photocatalytic water splitting of the oxygen doped material compared to pristine carbon nitride and for their trend with respect to the oxygen content in the different polymeric samples. Electrochemical hydrogen evolution was investigated on early transition metal carbides, following both experimental and computational proof of their catalytic activity. Hydrogen adsorption on the surfaces of TiC, VC, ZrC and NbC has been studied in its energetic trends, resulting in a clear raking sequence of carbides and surfaces activity. This could be correlated with the bulk and surface properties of those materials and provided justification for the use of certain parameters as qualitative descriptors of catalytic activity, such as the *d*-band centre position. *Ab-initio* thermodynamics was used to correlated adsorption energies with surface coverage states at different temperatures and pressures and to predict hydrogen evolution activity for each material and surface. Two of the best-performing materials, TiC and ZrC, were subsequently investigated in their catalytic activity over $CO_2$ adsorption, dissociation and hydrogenation. Adsorption is found to be strongly exothermic on all surfaces, driving the reaction towards CO, HCOO or COOH depending on the thermodynamics and kinetics of the reaction steps on each of the carbide surfaces. Dissociation is found to be in all cases more favourable thermodynamically, but the high reaction barriers limit its rates on (001) surfaces, driving the reaction towards hydrogenated intermediates. The (011) surfaces were found to be the most catalytically active, especially towards dissociation, which shows both the lowest reaction energy and lowest activation barrier on this surface. The three reactions interlink in a network of steps that leads to the reduction of $CO_2$ to CO,

HCOOH, $CH_3OH$ and $CH_4$ using molecular hydrogen as a reduction agent. This will be the subject of further studies in order to elucidate the mechanism of reduction of $CO_2$, which will follow the most efficient reduction steps on each surface to either gas phase CO or gas phase $CH_3OH$: the dissociation reaction and the hydrogenation to formate will be studied on the (011) and (111) surfaces of both carbides, the former leading to CO and $H_2O$ in the reverse WGS reaction and the latter leading to $CH_3OH$ via the CHO intermediate which spontaneously forms on (011), while the hydrogenation to hydroxyl path will be studied on both (001) surfaces leading to $CH_3OH$ through further hydrogenation followed by dissociation of one C-O bond. The successful conclusion of this project will allow us to close the circle that society leaves open when using fossil carbon resources for its needs of fuels and chemicals by reverting practically unlimited resources such as $H_2O$ and $CO_2$ back to usable form through the use of renewable energy and the physical and chemical properties of artificial materials. This work, while limited to a few materials and not yet complete, improves our understanding of the catalytic and photocatalytic activity of the materials we investigated, and will hopefully be part of the collective, global effort in building more sustainable ways of doing chemistry and storing energy.

# Bibliography


1. McGrath, M. Climate change: July 'marginally' warmest month on record. *BBC News* (2019).
2. McGrath, M. Climate change: UK's 10 warmest years all occurred since 2002. *BBC News* (2019).
3. National Oceanic and Atmospheric Administration. July 2019 was hottest month on record for the planet. (2019).
4. Holden, E. & Gambino, L. Green New Deal: Ocasio-Cortez unveils bold plan to fight climate change. *The Guardian* (2019).
5. Watts, J. Greta Thunberg backs climate general strike to force leaders to act. *The Guardian* (2019).
6. Laville, S. & Watts, J. Across the globe, millions join biggest climate protest ever. *The Guardian* (2019).
7. Boffey, D. & Oltermann, P. EU elections: voters boost Greens and far right as centre left and right lose out. *The Guardian* (2019).
8. UN. Paris Agreement. *Resour. can be found online http//unfccc.int/files/meetings/paris_nov_2015/application/pdf/paris_agreement_english_.pdf*
9. Masson-Delmotte, V. *et al. IPCC, 2018: Summary for Policymakers. In: Global Warming of 1.5°C. IPCC Special Report* (2018). doi:10.1017/CBO9781107415324
10. Turner, J. A. Sustainable Hydrogen Production. *Science (80-. ).* **305**, 972–974 (2004).
11. Centi, G., Quadrelli, E. A. & Perathoner, S. Catalysis for CO2 conversion: A key technology for rapid introduction of renewable energy in the value chain of chemical industries. *Energy Environ. Sci.* **6**, 1711–1731 (2013).
12. Aresta, M., Dibenedetto, A. & Angelini, A. Catalysis for the valorization of exhaust carbon: From CO2 to chemicals, materials, and fuels. technological use of CO2. *Chem. Rev.* **114**, 1709–1742 (2014).
13. IEA. *Energy Technology Perspectives 2012: Pathways to a Clean Energy System (Paris: OECD/IEA, 2012)*. *International Energy Agency* (2012).
14. Barber, J. Photosynthetic energy conversion: Natural and artificial. *Chem. Soc. Rev.* **38**, 185–196 (2009).
15. Dionigi, F. *et al.* Electrochemical Hydrogen Evolution: Sabatier's Principle and the Volcano Plot. *J. Chem. Educ.* **89**, 1595–1599 (2012).

16. Milbrandt, A. & Mann, M. Potential for Hydrogen Production from Key Renewable Resources in the United States. *Tech. Report, NREL/TP-640-41134* 1–23 (2007).

17. Wang, Y. *et al.* Mimicking Natural Photosynthesis: Solar to Renewable H2 Fuel Synthesis by Z-Scheme Water Splitting Systems. *Chem. Rev.* **118**, 5201–5241 (2018).

18. Park, S., Shao, Y., Liu, J. & Wang, Y. Oxygen electrocatalysts for water electrolyzers and reversible fuel cells: Status and perspective. *Energy Environ. Sci.* **5**, 9331–9344 (2012).

19. Alvarez-Galvan, M. C. *et al.* Direct methane conversion routes to chemicals and fuels. *Catal. Today* **171**, 15–23 (2011).

20. Ruether, J., Ramezan, M. & Grol, E. *Life-Cycle Analysis of Greenhouse Gas Emissions for Hydrogen Fuel Production in the United States from LNG and Coal*. (2005).

21. Bowker, M. Sustainable hydrogen production by the application of ambient temperature photocatalysis. *Green Chem.* **13**, 2235 (2011).

22. Zhao, G., Rui, K., Dou, S. X. & Sun, W. Heterostructures for Electrochemical Hydrogen Evolution Reaction: A Review. *Adv. Funct. Mater.* **28**, 1–26 (2018).

23. Safizadeh, F., Ghali, E. & Houlachi, G. Electrocatalysis developments for hydrogen evolution reaction in alkaline solutions - A Review. *Int. J. Hydrogen Energy* **40**, 256–274 (2015).

24. Millet, P., Ngameni, R., Grigoriev, S. A. & Fateev, V. N. Scientific and engineering issues related to PEM technology: Water electrolysers, fuel cells and unitized regenerative systems. *Int. J. Hydrogen Energy* **36**, 4156–4163 (2011).

25. Navarro, R. M., Sánchez-Sánchez, M. C., Alvarez-Galvan, M. C., Valle, F. Del & Fierro, J. L. G. Hydrogen production from renewable sources: Biomass and photocatalytic opportunities. *Energy Environ. Sci.* **2**, 35–54 (2009).

26. Zhu, J. & Zäch, M. Nanostructured materials for photocatalytic hydrogen production. *Curr. Opin. Colloid Interface Sci.* **14**, 260–269 (2009).

27. Kudo, A. New materials for photocatalytic and photoelectrochemical water splitting. *AIP Conf. Proc.* **1568**, 7–10 (2013).

28. Levin, D. B. & Chahine, R. Challenges for renewable hydrogen production from biomass. *Int. J. Hydrogen Energy* **35**, 4962–4969 (2010).

29. Lewis, N. S. & Nocera, D. G. Powering the planet: Chemical challenges in solar energy utilization. *Proc. Natl. Acad. Sci.* **103**, 15729–15735 (2006).

30. Tachibana, Y., Vayssieres, L. & Durrant, J. R. Artificial photosynthesis for solar water-splitting. *Nat. Photonics* **6**, 511–518 (2012).

31. Goodeve, C. F. & Kitchener, J. A. THE MECHANISM OF PHOTOSENSITISATION BY SOLIDS. 902–908 (1938).

32. FUJISHIMA, A. & HONDA, K. Electrochemical Photolysis of Water at a Semiconductor Electrode. *Nature* **238**, 37–38 (1972).

33. Zhang, Y. *et al.* Photocatalytic hydrogen evolution via water splitting: A short review. *Catalysts* **8**, (2018).

34. He, S., Rong, Q., Niu, H. & Cai, Y. Platform for molecular-material dual regulation: A direct Z-scheme MOF/COF heterojunction with enhanced visible-light photocatalytic activity. *Appl. Catal. B Environ.* **247**, 49–56 (2019).

35. Wang, Y. *et al.* Linker-controlled polymeric photocatalyst for highly efficient hydrogen evolution from water. *Energy Environ. Sci.* **10**, 1643–1651 (2017).

36. National Renewable Energy Laboratory. Reference Solar Spectral Irradiance. Available at: https://www.nrel.gov/grid/solar-resource/spectra.html.

37. Maeda, K. *et al.* GaN:ZnO solid solution as a photocatalyst for visible-light-driven overall water splitting. *J. Am. Chem. Soc.* **127**, 8286–8287 (2005).

38. Ye, S., Wang, R., Wu, M. Z. & Yuan, Y. P. A review on g-C 3 N 4 for photocatalytic water splitting and CO 2 reduction. *Appl. Surf. Sci.* **358**, 15–27 (2015).

39. Martin, D. J., James, P., Reardon, T., Moniz, S. J. A. & Tang, J. Visible light-driven pure water splitting by a nature-inspired organic semiconductor based system Supporting information. **44**, 1–6 (2014).

40. Jorge, A. B. *et al.* H2 and O2 evolution from water half-splitting reactions by graphitic carbon nitride materials. *J. Phys. Chem. C* **117**, 7178–7185 (2013).

41. Higashi, M., Abe, R., Takata, T. & Domen, K. Photocatalytic overall water splitting under visible light using ATaO 2N (A = Ca, Sr, Ba) and WO 3 in a IO 3-/I - shuttle redox mediated system. *Chem. Mater.* **21**, 1543–1549 (2009).

42. Ma, S. S. K. *et al.* A redox-mediator-free solar-driven Z-scheme water-splitting system consisting of modified Ta3N5 as an oxygen-evolution photocatalyst. *Chem. - A Eur. J.* **19**, 7480–7486 (2013).

43. Wang, Q. *et al.* Particulate photocatalyst sheets based on carbon conductor layer for efficient Z-scheme pure-water splitting at ambient pressure. *J. Am. Chem. Soc.* **139**, 1675–1683 (2017).

44. Zhang, J. & Wang, X. Solar Water Splitting at λ=600 nm: A Step Closer to Sustainable Hydrogen Production. *Angew. Chemie - Int. Ed.* **54**, 7230–7232 (2015).

45. Larkin, P. J., Makowski, M. P. & Colthup, N. B. The form of the normal modes of s-triazine: Infrared and Raman spectral analysis and ab initio force field calculations. *Spectrochim. Acta - Part A Mol. Biomol. Spectrosc.* **55**, 1011–1020 (1999).

46. Martin, D. J., Umezawa, N., Chen, X., Ye, J. & Tang, J. Facet engineered Ag3PO4 for efficient water photooxidation. *Energy Environ. Sci.* **6**, 3380–3386 (2013).

47. Kudo, A., Omori, K. & Kato, H. A novel aqueous process for preparation of crystal form-controlled and highly crystalline BiVO4 powder from layered vanadates at room temperature and its photocatalytic and photophysical properties. *J. Am. Chem. Soc.* **121**, 11459–11467 (1999).

48. Jones, W. *et al.* A comparison of photocatalytic reforming reactions of methanol and triethanolamine with Pd supported on titania and graphitic carbon nitride. *Appl. Catal. B Environ.* **240**, 373–379 (2019).

49. Hitoki, G. *et al.* An oxynitride, TaON, as an efficient water oxidation photocatalyst under visible light irradiation (λ ≤ 500 nm). *Chem. Commun.* **2**, 1698–1699 (2002).

50. Qin, P. *et al.* High incident photon-to-current conversion efficiency of p-type dye-sensitized solar cells based on NiO and organic chromophores. *Adv. Mater.* **21**, 2993–2996 (2009).

51. Zhou, L. *et al.* Recent advances in non-metal modification of graphitic carbon nitride for photocatalysis: A historic review. *Catal. Sci. Technol.* **6**, 7002–7023 (2016).

52. Liebig, J. About some nitrogen compounds. *Ann. Pharm.* **10**, (1834).

53. Thomas, A. *et al.* Graphitic carbon nitride materials: Variation of structure and morphology and their use as metal-free catalysts. *J. Mater. Chem.* **18**, 4893–4908 (2008).

54. Fina, F. *et al.* Structural investigation of graphitic carbon nitride via XRD and Neutron Diffraction Structural investigation of graphitic carbon nitride via XRD and Neutron Diffraction. (2015). doi:10.1021/acs.chemmater.5b00411

55. Wang, X. *et al.* A metal-free polymeric photocatalyst for hydrogen production from water under visible light. *Nat. Mater.* **8**, 76–80 (2008).

56. Srinivasu, K., Modak, B. & Ghosh, S. K. Improving the photocatalytic activity of s-triazine based graphitic carbon nitride through metal decoration: an ab initio investigation. *Phys. Chem. Chem. Phys.* **18**, 26466–26474 (2016).

57. Martin, D. J. *et al.* Highly efficient photocatalytic H2 evolution from water using visible light and structure-controlled graphitic carbon nitride. *Angew. Chemie - Int. Ed.* **53**, 9240–9245 (2014).

58. Tyborski, T. *et al.* Crystal structure of polymeric carbon nitride and the determination of its process-temperature-induced modifications. *J. Phys. Condens. Matter* **25**, 395402 (2013).

59. Migani, A., Mowbray, D. J., Zhao, J., Petek, H. & Rubio, A. Quasiparticle level alignment for photocatalytic interfaces. *J. Chem. Theory Comput.* **10**, 2103–2113 (2014).

60. Bahers, T. Le, Rérat, M. & Sautet, P. Semiconductors used in photovoltaic and photocatalytic devices: Assessing fundamental properties from DFT. *J. Phys. Chem. C* **118**, 5997–6008 (2014).

61. Yang, S., Prendergast, D. & Neaton, J. B. Tuning semiconductor band edge energies for solar photocatalysis via surface ligand passivation. *Nano Lett.* **12**, 383–388 (2012).

62. Wang, M., Wang, Z., Gong, X. & Guo, Z. The intensification technologies to water electrolysis for hydrogen production - A review. *Renew. Sustain. Energy Rev.* **29**, 573–588 (2014).

63. Liu, Y., Kelly, T. G., Chen, J. G. & Mustain, W. E. Metal carbides as alternative electrocatalyst supports. *ACS Catal.* **3**, 1184–1194 (2013).

64. Chen, W.-F. F., Muckerman, J. T. & Fujita, E. Recent developments in transition metal carbides and nitrides as hydrogen evolution electrocatalysts. *Chem. Commun.* **49**, 8896–8909 (2013).

65. Laursen, A. B. *et al.* Electrochemical hydrogen evolution: Sabatiers principle and the volcano plot. *J. Chem. Educ.* **89**, 1595–1599 (2012).

66. Quaino, P., Juarez, F., Santos, E. & Schmickler, W. Volcano plots in hydrogen electrocatalysis – uses and abuses. 846–854 (2014). doi:10.3762/bjnano.5.96

67. Norskov, J. K. *et al.* Trends in the exchange current for hydrogen evolution. *J. Electrochem. Soc.* **152**, (2005).

68. Delannoy, L., Giraudon, J. M., Granger, P., Leclercq, L. & Leclercq, G. Group VI transition metal carbides as alternatives in the hydrodechlorination of chlorofluorocarbons. *Catal. Today* **59**, 231–240 (2000).

69. Carmo, M., Fritz, D. L., Mergel, J. & Stolten, D. A comprehensive review on PEM water electrolysis. *Int. J. Hydrogen Energy* **38**, 4901–4934 (2013).

70. Schweitzer, N. M. *et al.* High activity carbide supported catalysts for water gas shift. *J. Am. Chem. Soc.* **133**, 2378–2381 (2011).

71. Esposito, D. V *et al.* Low-Cost Hydrogen-Evolution Catalysts Based on Monolayer Platinum on Tungsten Monocarbide Substrates **. 9859–9862 (2010). doi:10.1002/anie.201004718

72. Xiao, Y., Hwang, J.-Y. & Sun, Y.-K. Transition metal carbide-based materials: synthesis and applications in electrochemical energy storage. *J. Mater. Chem. A* **4**, 10379–10393 (2016).

73. Levy, R. B. & Boudart, M. Platinum-Like Behavior of Tungsten Carbide in Surface Catalysis. *Science (80-. ).* **181**, 547–549 (1973).

74. Ono, L. K., Sudfeld, D. & Roldan Cuenya, B. In situ gas-phase catalytic properties of TiC-supported size-selected gold nanoparticles synthesized by diblock copolymer encapsulation. *Surf. Sci.* **600**, 5041–5050 (2006).

75. Kunkel, C., Viñes, F. & Illas, F. Transition metal carbides as novel materials for $CO_2$ capture, storage, and activation. *Energy Environ. Sci.* **9**, 141–144 (2016).

76. Posada-Pérez, S. *et al.* The bending machine: $CO_2$ activation and hydrogenation on δ-MoC(001) and β-$Mo_2C$(001) surfaces. *Phys. Chem. Chem. Phys.* **16**, 14912–14921 (2014).

77. Porosoff, M. D., Kattel, S., Li, W., Liu, P. & Chen, J. G. Identifying trends and descriptors for selective CO2 conversion to CO over transition metal carbides. *Chem. Commun.* **51**, 6988–6991 (2015).

78. Porosoff, M. D., Yang, X., Boscoboinik, J. A. & Chen, J. G. Molybdenum carbide as alternative catalysts to precious metals for highly selective reduction of CO2 to CO. *Angew. Chemie - Int. Ed.* **53**, 6705–6709 (2014).

79. Stottlemyer, A. L., Kelly, T. G., Meng, Q. & Chen, J. G. Reactions of oxygen-containing molecules on transition metal carbides: Surface science insight into potential applications in catalysis and electrocatalysis. *Surf. Sci. Rep.* **67**, 201–232 (2012).

80. Porosoff, M. D., Kattel, S., Li, W., Liu, P. & Chen, J. G. Identifying trends and descriptors for selective $CO_2$ conversion to CO over transition metal carbides. *Chem. Commun.* **51**, 6988–6991 (2015).

81. Posada-Pérez, S. *et al.* The bending machine: CO2 activation and hydrogenation on δ-MoC(001) and β-Mo2C(001) surfaces. *Phys. Chem. Chem. Phys.* **16**, 14912–14921 (2014).

82. Ted Oyama, S. Crystal structure and chemical reactivity of transition metal carbides and nitrides. *J. Solid State Chem.* **96**, 442–445 (1992).

83. Esposito, D. V., Hunt, S. T., Kimmel, Y. C. & Chen, J. G. A new class of electrocatalysts for hydrogen production from water electrolysis: Metal monolayers supported on low-cost transition metal carbides. *J. Am. Chem. Soc.* **134**, 3025–3033 (2012).

84. Ledoux, M. J., Huu, C. P., Guille, J. & Dunlop, H. Compared activities of platinum and high specific surface area Mo2C and WC catalysts for reforming reactions. I. Catalyst activation and stabilization: Reaction of n-hexane. *J. Catal.* **134**, 383–398 (1992).

85. Quesne, M. G., Roldan, A., de Leeuw, N. H. & Catlow, C. R. A. Bulk and surface properties of metal carbides: implications for catalysis.

86. Ferri, T., Gozzi, D. & Latini, A. Hydrogen evolution reaction (HER) at thin film and bulk TiC electrodes. *Int. J. Hydrogen Energy* **32**, 4692–4701 (2007).

87. Cohen, M. L., Louie, S. G., Grossman, J. C., Mizel, A. & Co, M. Cohen et al. - 1999 - Transition metals and their carbides and nitrides Trends in electronic and structural properties. **60**, 6343–6347 (1999).

88. Zhao, Y., Dillon, A. C., Kim, Y. H., Heben, M. J. & Zhang, S. B. Self-catalyzed

hydrogenation and dihydrogen adsorption on titanium carbide nanoparticles. *Chem. Phys. Lett.* **425**, 273–277 (2006).

89. Quesne, M. G., Roldan, A., De Leeuw, N. H. & Catlow, C. R. A. Bulk and surface properties of metal carbides: Implications for catalysis. *Phys. Chem. Chem. Phys.* **20**, 6905–6916 (2018).

90. Martens, J. A. *et al.* Catalysis for the valorization of exhaust carbon: from CO2 to chemicals, materials, and fuels. technological use of CO2. *Chem. Rev.* **6**, 1709–42 (2010).

91. Stratton, R. W., Wong, H. M. & Hileman, J. I. Quantifying variability in life cycle greenhouse gas inventories of alternative middle distillate transportation fuels. *Environ. Sci. Technol.* **45**, 4637–4644 (2011).

92. Gangeri, M. *et al.* Fe and Pt carbon nanotubes for the electrocatalytic conversion of carbon dioxide to oxygenates. *Catal. Today* **143**, 57–63 (2009).

93. Rodriguez, J. A. *et al.* CO2 hydrogenation on Au/TiC, Cu/TiC, and Ni/TiC catalysts: Production of CO, methanol, and methane. *J. Catal.* **307**, 162–169 (2013).

94. Wang, W., Wang, S., Ma, X. & Gong, J. Recent advances in catalytic hydrogenation of carbon dioxide. *Chem. Soc. Rev.* **40**, 3703–3727 (2011).

95. Ma, J. *et al.* A short review of catalysis for CO2 conversion. *Catal. Today* **148**, 221–231 (2009).

96. Wang, Z., Cao, X. M., Zhu, J. & Hu, P. Activity and coke formation of nickel and nickel carbide in dry reforming: A deactivation scheme from density functional theory. *J. Catal.* **311**, 469–480 (2014).

97. Wei, J. *et al.* Directly converting CO2 into a gasoline fuel. *Nat. Commun.* **8**, 15174 (2017).

98. Gao, P. *et al.* Direct conversion of CO2 into liquid fuels with high selectivity over a bifunctional catalyst. *Nat. Chem.* 1–6 (2017). doi:10.1038/nchem.2794

99. Oshikawa, K., Nagai, M. & Omi, S. Characterization of molybdenum carbides for methane reforming by TPR, XRD, and XPS. *J. Phys. Chem. B* **105**, 9124–9131 (2001).

100. Lim, R. J. *et al.* A review on the electrochemical reduction of CO2 in fuel cells, metal electrodes and molecular catalysts. *Catal. Today* **233**, 169–180 (2014).

101. Silveri, F., Quesne, M. G., Roldan, A., De Leeuw, N. H. & Catlow, C. R. A. Hydrogen adsorption on transition metal carbides: A DFT study. *Phys. Chem. Chem. Phys.* **21**, 5335–5343 (2019).

102. Quesne, M. G., Roldan, A., De Leeuw, N. H. & Catlow, C. R. A. Carbon dioxide and water co-adsorption on the low-index surfaces of TiC, VC, ZrC and NbC: A DFT study. *Phys. Chem. Chem. Phys.* **21**, 10750–10760 (2019).

103. Kim, J. H., Woo, H., Choi, J., Jung, H. W. & Kim, Y. T. CO2 Electroreduction on Au/TiC: Enhanced Activity Due to Metal-Support Interaction. *ACS Catal.* **7**, 2101–2106 (2017).

104. Posada-pe, S. *et al.* Highly Active Au/ δ -MoC and Cu/ δ -MoC Catalysts for the Conversion of CO 2 : The Metal/C Ratio as a Key Factor De fi ning Activity, Selectivity, and Stability. *North Am. Meet. North Am. Catal. Soc.* (2017). doi:10.1021/jacs.6b04529

105. Tao, J., Perdew, J. P., Staroverov, V. N. & Scuseria, G. E. Climbing the density functional ladder: Nonempirical meta–generalized gradient approximation designed for molecules and solids. *Phys. Rev. Lett.* **91**, 3–6 (2003).

106. Stampfl, C., Mannstadt, W., Asahi, R. & Freeman, A. J. Electronic structure and physical properties of early transition metal mononitrides: Density-functional theory LDA, GGA, and screened-exchange LDA FLAPW calculations. *Phys. Rev. B - Condens. Matter Mater. Phys.* **63**, 1–11 (2001).

107. Becke, A. Density functional calculations of molecular bond energies. **84**, (1998).

108. Perdew, J. P., Burke, K. & Ernzerhof, M. Generalized Gradient Approximation Made Simple. *Phys. Rev. Lett.* **77**, 3865–3868 (1996).

109. Blöchl, P. E. Projector augmented-wave method. *Phys. Rev. B* **50**, 17953–17979 (1994).

110. Kresse, G. & Joubert, D. From ultrasoft pseudopotentials to the projector augmented-wave method. *Phys. Rev. B* **59**, 1758–1175 (1999).

111. Grimme, S., Antony, J., Ehrlich, S. & Krieg, H. (2010)JCP_Grimme_A consistent and accurate ab initio parametrization of density functional dispersion correction „DFT-D… for the 94 elements H-Pu.pdf. *J. Chem. Phys.* **132**, (2010).

112. Kresse, G. & Furthmüller, J. Efficient iterative schemes for *ab initio* total-energy calculations using a plane-wave basis set. *Phys. Rev. B* **54**, 11169–11186 (1996).

113. Blöchl, P. E., Jepsen, O. & Andersen, O. K. Improved tetrahedron method for Brillouin-zone integrations. *Phys. Rev. B* **49**, 16223–16233 (1994).

114. Bader, R. F. W. Atoms in Molecules: A Quantum Theory. *Oxford Univ. Press*

115. Henkelman, G., Arnaldsson, A. & Jónsson, H. A fast and robust algorithm for Bader decomposition of charge density. *Comput. Mater. Sci.* **36**, 354–360 (2006).

116. Tang, W., Sanville, E. & Henkelman, G. A grid-based Bader analysis algorithm without lattice bias. *J. Phys. Condens. Matter* **21**, 084204 (2009).

117. Trasatti, S. Structure of the metal/electrolyte solution interface: new data for theory. *Electrochim. Acta* **36**, 1659–1667 (1991).

118. Skúlason, E. *et al.* Density functional theory calculations for the hydrogen evolution reaction in an electrochemical double layer on the Pt(111) electrode. *Phys. Chem. Chem. Phys.* **9**, 3241–3250 (2007).

119. Rossmeisl, J., Skúlason, E., Björketun, M. E., Tripkovic, V. & Nørskov, J. K. Modeling the electrified solid-liquid interface. *Chem. Phys. Lett.* **466**, 68–71 (2008).

120. Wang, X.-G. *et al.* Submitted to Phys. Rev. Letters The hematite ( α -Fe 2 O 3 ) (0001) surface: evidence for domains of distinct chemistry. 3–6 (2008).

121. Santos-Carballal, D., Roldan, A., Grau-Crespo, R. & de Leeuw, N. H. A DFT study of the structures, stabilities and redox behaviour of the major surfaces of magnetite Fe3O4. *Phys. Chem. Chem. Phys.* **16**, 21082–21097 (2014).

122. Gong, J., Liang, J. & Sumathy, K. Review on dye-sensitized solar cells (DSSCs): Fundamental concepts and novel materials. *Renew. Sustain. Energy Rev.* **16**, 5848–5860 (2012).

123. Wang, Y. *et al.* Bandgap Engineering of Organic Semiconductors for Highly Efficient Photocatalytic Water Splitting. *Adv. Energy Mater.* **8**, (2018).

124. Hu, W., Lin, L., Yang, C., Dai, J. & Yang, J. Edge-Modified Phosphorene Nanoflake Heterojunctions as Highly Efficient Solar Cells. *Nano Lett.* **16**, 1675–1682 (2016).

125. Hu, W., Lin, L., Zhang, R., Yang, C. & Yang, J. Highly Efficient Photocatalytic Water Splitting over Edge-Modified Phosphorene Nanoribbons. *J. Am. Chem. Soc.* **139**, 15429–15436 (2017).

126. Posada-Pérez, S. *et al.* Highly active Au/δ-MoC and Au/β-Mo2C catalysts for the low-temperature water gas shift reaction: Effects of the carbide metal/carbon ratio on the catalyst performance. *Catal. Sci. Technol.* **7**, 5332–5342 (2017).

127. Posada-Pérez, S. *et al.* The conversion of CO2 to methanol on orthorhombic β-Mo2C and Cu/β-Mo2C catalysts: Mechanism for admetal induced change in the selectivity and activity. *Catal. Sci. Technol.* **6**, 6766–6777 (2016).

128. Hwu, H. H. & Chen, J. G. Surface chemistry of transition metal carbides. *Chem. Rev.* **105**, 185–212 (2005).

129. Yang, W., Rehman, S., Chu, X., Hou, Y. & Gao, S. Transition Metal (Fe, Co and Ni)Carbide and Nitride Nanomaterials:S tructure, Chemical Synthesis and Applications. *ChemNanoMat* **13**, 76–398 (2015).

130. Posada-P??rez, S., Vi??es, F., Valero, R., Rodriguez, J. A. & Illas, F. Adsorption and dissociation of molecular hydrogen on orthorhombic ??-Mo2C and cubic ??-MoC (001) surfaces. *Surf. Sci.* **656**, 24–32 (2017).

131. Trasatti, S. Work function, electronegativity, and electrochemical behaviour of metals. III. Electrolytic hydrogen evolution in acid solutions. *J. Electroanal.*

*Chem.* **39**, 163–184 (1972).

132. Tasker, P. W. The stability of ionic crystal surfaces. *J. Phys. C Solid State Phys.* **12**, 4977–4984 (1979).

133. Aizawa, T., Hayami, W., Souda, R., Otani, S. & Ishizawa, Y. Hydrogen adsorption on transition-metal carbide (111) surfaces. *Surf. Sci.* **381**, 157–164 (1997).

134. Hayami, W., Souda, R., Aizawa, T., Otani, S. & Ishizawa, Y. Analysis of the NbC(111)-(\ensuremath{\surd}3 \ifmmode\times\else\texttimes\fi{} \ensuremath{\surd}3 )R30\ifmmode^\circ\else\textdegree\fi{}-Al surface structure by impact-collision ion-scattering spectroscopy. *Phys. Rev. B* **47**, 13752–13758 (1993).

135. Souda, R., Aizawa, T., Otani, S. & Ishizawa, Y. Effects of chemical bonding on the electronic transition in low energy He+ scattering. *Surf. Sci.* **232**, 219–227 (1990).

136. Hayami, W. et al. Analysis of the HfC(111) surface structure by impact collision ion scattering spectroscopy (ICISS). *Surf. Sci.* **276**, 299–307 (1992).

137. Ling, C., Shi, L., Ouyang, Y. & Wang, J. Searching for Highly Active Catalysts for Hydrogen Evolution Reaction Based on O-Terminated MXenes through a Simple Descriptor. *Chem. Mater.* **28**, 9026–9032 (2016).

138. Yu, X. & Pickup, P. G. Recent advances in direct formic acid fuel cells (DFAFC). *J. Power Sources* **182**, 124–132 (2008).

139. Wasmus, S. & Küver, A. Methanol oxidation and direct methanol fuel cells: A selective review. *J. Electroanal. Chem.* **461**, 14–31 (1999).